Summer 2003

Monte Carlo Analysis of Millimeter-Wave GaN Based Gunn Effect Oscillators

Sridhara Viswanadham
Old Dominion University

Monte Carlo Analysis of Millimeter-Wave GaN Based

Gunn Effect Oscillators

by

Sridhara Viswanadham
B.E in Electrical and Electronics Engineering (EEE), April 2000,
College of Engineering, Osmania University,
Hyderabad, Andhra Pradesh, India.

A Thesis Submitted to the Faculty of
Old Dominion University in Partial Fulfillment of the
Requirement for the Degree of

MASTER OF SCIENCE

ELECTRICAL ENGINEERING

OLD DOMINION UNIVERSITY
August 2003

Approved by:

Dr. Ravindra P. Joshi (Director)

Dr. Linda L. Vahala (Member)

Dr. Frederic McKenzie (Member)

ABSTRACT

Monte Carlo Analysis of Millimeter-Wave GaN Based Gunn Effect Oscillators

Sridhara Viswanadham
Old Dominion University, 2003
Director: Dr. Ravindra P. Joshi

Gunn diodes are one of the most common high frequency solid-state oscillators at the present time, and are considered as promising devices for millimeter and sub-millimeter wave applications. Monte Carlo studies of Gunn diodes based on bulk wurtzite GaN have been carried out in this thesis research. Two structures have been examined: (i) devices with conventional single notch structure and (ii) repetitive structures with serial segments to fashion a "multiple domain" device. Wurtzite GaN has been chosen because of the high drift velocity and because analytical expressions for the band structure have recently become available. Performance parameters of interest such as operating frequency, output power and conversion efficiency have been calculated. Variations due to changes in temperature, biasing voltage, and device length are also included. Due to their high frequency and power characteristics, GaN Gunn diodes are used as sources for the generation of millimeter wave signals. It is shown that there is a considerable improvement in output power and operating frequency over the reported results of InP and GaAs. It is also shown that multi-domain Gunn diodes can lead to significant improvements in output power over conventional, single-transit structure, and so such multiple GaN diodes merit serious experimental study.

This thesis work is dedicated to

all my family members,

my friends, and my Graduate Program Advisor

Dr. Ravindra P. Joshi.

TABLE OF CONTENTS

LIST OF FIGURES

LIST OF TABLES

CHAPTER I

INTRODUCTION

1.1 INTRODUCTION

Gunn diodes are one of the most common high frequency solid-state oscillators at the present time, and are considered as promising devices for millimeter and sub-millimeter wave applications [1].

There has been considerable interest in bulk GaN semiconductor material because of its large bandgap. This should facilitate higher applied voltages and allow for larger power, reduced electrical noise due for lower thermal generation, and withstand higher electric fields leading to higher carrier velocities and shorter transit times. It also exhibits other favorable electrical properties, such as high electron mobility and very high thermal conductivity, which bodes well for thermal management. Its bandgap of nearly 3.5eV makes it an important candidate for blue and ultraviolet electroluminescent devices. This large bandgap also results in a large breakdown field, which together with its high thermal conductivity, makes GaN especially suitable for high-power, high-temparture, and high-speed applications. In light of the above, GaN becomes an important semiconductor material, and merits study as it is a relatively emerging technology.

Monte Carlo Studies of transferred electron oscillators based on bulk wurtzite GaN are presented in this thesis report. Two structures have been examined here: (i) devices with the conventional single notch structure, and (ii) repetitive structures with

---

References according to the Journal of Applied Physics.

serial segments to form a "multiple domain" device. The primary aim is to evaluate the performance of Gunn diodes based on the GaN material technology, and to make comparisons with the well-known GaAs material system.

There are, of course, many other possible applications for such band-gap engineering. Starting from the initial discovery of the NDR (negative differential resistance), the phenomenon of semiconductor based microwave signal generation, amplification and processing has run the course of truly exciting research endeavors. Various theoretical aspects have been studied in order to understand the physical phenomenon, characterize the different device operating modes, probe fundamental device limitations, and to analyze performance parameters such as noise spectra and microwave power conversion efficiencies. Despite the abundant literature available on this topic, a re-evaluation of Gunn-effect electronics probably becomes necessary for reasons linked to its high power and high-speed capabilities. Also, our understanding of the subtleties of electron dynamics has improved significantly over the last decade. Better values for the material parameters, inter-valley separation thresholds [2], phonon-eigen energies[3], and electron-phonon coupling constants[4] have been obtained through experimentation. Also, better device simulation techniques, such as those based on the Monte Carlo method, have been developed. Therefore, it becomes germane and important to analyze GaN-based Gunn oscillators from the standpoint of improved accuracy, realistic predictions, and performance evaluations.

1.2   CONVENTIONAL GUNN DIODE OSCILLATORS

Currently, Gunn effect oscillators (or Transferred electron oscillators, as they are also known) are among the most promising candidates for semiconductor microwave applications. A conventional Gunn diode consists of three layers; a relatively low-doped transit region which is sandwiched between two very highly doped contact layers, forming an n+ - n - n+ structure. A bias is applied across the contact layers causing electrons to flow from the cathode to the anode. As the electrons are accelerated in the electric field, they gain energy and momentum. During this acceleration, they also partially lose some energy because of the inelastic scattering mechanisms (described later) with the atoms/phonons. The profile of the electric potential in the transit region under bias is non-linear, with its gradient, the electric field ever increasing as it approaches the anode. As the electric field becomes larger, the rate of gain of energy from the electric field exceeds the rate of loss from inelastic scattering, and the electron has, on average, a net gain of energy with time and distance traveled. If the transit region and the applied bias are sufficiently large, then at some point, the electrons gain enough energy to transfer from the central valley to an upper satellite valley. This is explained later in detail in Chapter II. The spatial region extending from the cathode up to this point of inter-valley transfer is called the dead zone. The rate of loss of energy in the dead zone due to phonon emission and other inelastic scatterings can be quite large. Since this is wasted energy and does not contribute to active power, the efficiency can suffer for devices containing long dead zones. In addition, since significant inter-valley transfer does not take place in this region, negative differential mobilities, which contribute to the

active power, are also absent. Hence, a primary objective is to reduce the dead zone through suitable device design.

1.3   MULTI-DOMAIN GUNN DIODE

A serial connection of several Gunn diode elements was first proposed in 1968 by Thim [5]. In essence, this amounts to a simple stacking of several wafers of conventional Gunn diodes in series with each other. The idea was further carried by Slater and Harrison[6], who demonstrated two and three domain Gunn diode operation, using simple horizontal diodes (i.e., with current flow parallel to the semiconductor surface). The results show that multi-domain Gunn diodes can lead to significant improvements in output power over conventional single-transit structure and so such multiple GaN diodes merit serious experimental and theoretical study. Such a study has also been carried out in this thesis research.

1.4   IMPROVING THE GUNN DIODE DESIGN

The above concept is relatively easy to understand in qualitative terms. The complexity begins when one starts thinking about the systems applications for this device to work as an oscillator. There are several performance specifications, which need to be optimized simultaneously. The two primary specifications for an oscillator are its operating frequency and the output power it delivers. The oscillating frequency is related to the transit time between the inter-valley transfer location and the anode. This is discussed in detail later. The limit to the power output is the amount of charge that the accumulation layer can collect without exceeding the breakdown field at the anode.

In order to maximize the output power and the efficiency for a particular length of the device, the accumulation layer should be formed very close to the cathode. In other words, the dead zone should be as small as possible. Thus, by choosing an appropriate transit region length and doping, it is possible to maximize the power for a desired frequency at a particular bias.

In view of the above discussion, it becomes apparent that the problem of attaining optimized device design is non-trivial. General guidelines and probable trends towards optimization can however be successfully obtained by simulating a variety of device structures (different doping profiles and material composition). The current goal is to take a step in this direction by focusing both on the conventional Gunn diode as well as the multi-domain Gunn diodes. A Monte Carlo numerical simulation scheme, discussed later in this thesis, has been employed for greater accuracy and precision.

Many simulations of Gunn effect oscillators in the past have relied on a variety of assumptions that are a somewhat simplifying. For example, early studies by Copeland [7] assumed that electrons could respond instantaneously to changes in the electric fields. In subsequent work [8,9], the electronic relaxation effects were explicitly included, but the analysis nonetheless used approximations to the actual carrier distribution functions. Lebwohl and Price using the Monte Carlo method [10] were the first to study Gunn effect devices without making any approximations for the electronic distribution functions. Unfortunately, their analysis did not include the correct bandgap ordering, since the sequence of the bandgaps $\Gamma_c^6 - L_c^6 - X_c^6$ was experimentally established at a later stage [11]. In a more recent work, many of the previous problems were addressed by Tully [12]. We will make the present study of both conventional Gunn diodes as well as the

multi-domain Gunn diodes without making assumptions, such as the distribution functions, or an instantaneous electronic response.

Before summarizing the scope of this thesis, a brief discussion outlining the advantages of multi-domain Gunn diodes is perhaps necessary. Neglecting heat limitation, it can be seen that the N-domain diode should be able to deliver N^2 times as much power at a given frequency as a conventional single-domain diode. The reason for the improvement is that an N-domain diode has N times the impedance of a single-domain diode at the same frequency. Therefore, its cross-sectional area can be increased by a factor of N without exceeding the maximum value of conductance the circuit can provide without excessive circuit loss. Hence, the volume of the diode and its power are increased by N^2. The above reasons indicate that multi-domain Gunn diodes merit serious experimental study.

1.5   SCOPE OF THESIS

The present work is dedicated to the study of Gunn devices for microwave oscillations using the Ensemble Monte Carlo (EMC) technique. In Chapter II, a brief review of the physical characteristics of microwave devices is presented. A brief comparison between various semiconductor microwave devices is also made. A description of the Negative Differential Resistance (NDR) property of GaN is also presented in Chapter II. The objective of this chapter is to show that time-varying, spatially-dependent, internal charge distributions within the device are necessary and can develop for microwave oscillations. In Chapter III, the principles of Monte Carlo method, applied to the study of semiconductors, are introduced and discussed. The general

features of EMC algorithm used for the consistent simulation of semiconductor devices are thoroughly presented. This chapter also explains the implementation of the algorithms for the solution of Poisson's equation. The EMC model implemented for the simulation of the Gunn diode is presented in Chapter IV. The complete details concerning the modeling of the Gunn diode and its interaction with the external circuit are discussed. This is followed by the discussion of the results. Finally, Chapter V summarizes the central results of this thesis, and lists scope for possible future work in this area.

CHAPTER II

LITERATURE REVIEW AND BACKGROUND

2.1   INTRODUCTION

A quick review of GaN Gunn diode literature is given in this chapter. The electrical and optical properties of GaN are discussed. A comparison between the properties of GaN and GaAs is also presented. A study of the fundamental properties of GaN indicates that this material should exhibit the "transferred electron effect". A wide band gap of 3.5 eV and other useful properties, such as, high electron mobility and very high thermal conductivity should make GaN a very suitable candidate in Gunn diodes for high power microwave applications. Characterization of the bulk GaN properties is discussed in section 2. This is followed by a brief description about other solid-state microwave devices in bulk semiconductors, such as, tunnel diodes that also exhibit the NDR (Negative Differential Resistance) property. Then, finally Gunn diode operation and related theory, is discussed.

2.2   AIM AND SCOPE OF THESIS RESEARCH

GaN is a relatively new material for semiconductor devices and not much research has been done in this area. There is, as yet, no confirmation of the transferred-electron effect in GaN based materials, although its bandstructure suggests it should occur.   The breakdown voltage for GaN is higher than the other commonly used semiconductors due to its large bandgap, and this material has a higher thermal conductivity. These aspects collectively suggest that GaN based electronic devices could

potentially be very useful for microwave power generation applications. Hence, it becomes worthwhile to evaluate the frequency and power capability of GaN Gunn devices, in order to estimate and assess their probable advantages. The present work is an effort towards this goal, and dedicated to the simulation study of the GaN Gunn devices for microwave oscillations using the ensemble Monte Carlo Technique.

2.3 OVERVIEW OF THE GaN MATERIAL SYSTEM

Over the past five years or so, the nitride material system has been the focus of intense research [13-21]. Advantages of these direct, large bandgap materials include higher breakdown voltages, the ability to sustain large electric fields (which helps for device downscaling), lower generation noise, radiation hardness and high-temperature operation.

GaN-based electronic amplifiers are projected to have significant improvement over silicon devices [21]. The nitrides have also shown promise as emitters and detectors [22-24], Bragg reflectors [25], light-emitting diodes (LEDs) [26], sensors for jet and automobile engines [27], and space-based operation in the solar blind region (~ 260 - 290 nm).

The high-field drift velocity of bulk GaN is larger than that of GaAs [28-29] due to the higher inter-valley separation and the larger optical phonon energy. GaN lends itself to hetero-structure fabrication, and the presence of a strong internal polarization can create very high sheet carrier densities. Experimental demonstrations of large radio-frequency (RF) power densities, as measured in Watts per millimeter of the gate periphery, have already been made [30-31]. The higher thermal conductivity of GaN

relative to GaAs and use of SiC substrates [34,35] should help alleviate the thermal management issue. These aspects collectively enhance the prospects of GaN for microwave power amplification, particularly at the X-band and higher frequencies [36-38].

2.3.1 ELECTRON TRANSPORT PROPERTIES OF BULK GaN

To date, only a few theoretical investigations of the electronic properties of the bulk GaN [39-41] have been made. Steady-state electron drift velocity calculations have been made based on the Ensemble Monte Carlo technique. These calculations for bulk GaN have either assumed a one- or two- valley analytical band structure for simplicity, or used full three-valley, non-parabolic conduction band models for higher accuracy [28].

It is now well known that GaN crystallizes in both the Zinc-blende and Wurtzite structures with slightly different material properties and substantially different band structures. Brennan et al. [42] reported on the bulk electronic transport properties in both zincblende and wurtzite phases. The calculation of the electronic band structures was based on the empirical pseudopotential method [43, 44]. Since the band energies are required over a dense k-space mesh throughout the Brillouin zone, which has been shown in Fig 2.1, computational efficiency becomes important. Consequently, in the Brennan analysis, the spin-orbit interaction was neglected and a local pseudopotential used. Approximately, an additional 100 plane wave states were included in Lowdin perturbation theory [45]. The effective mass was taken as the principle fitting parameter. For wurtzite material, the accepted experimental value for the energy gap is 3.4eV and
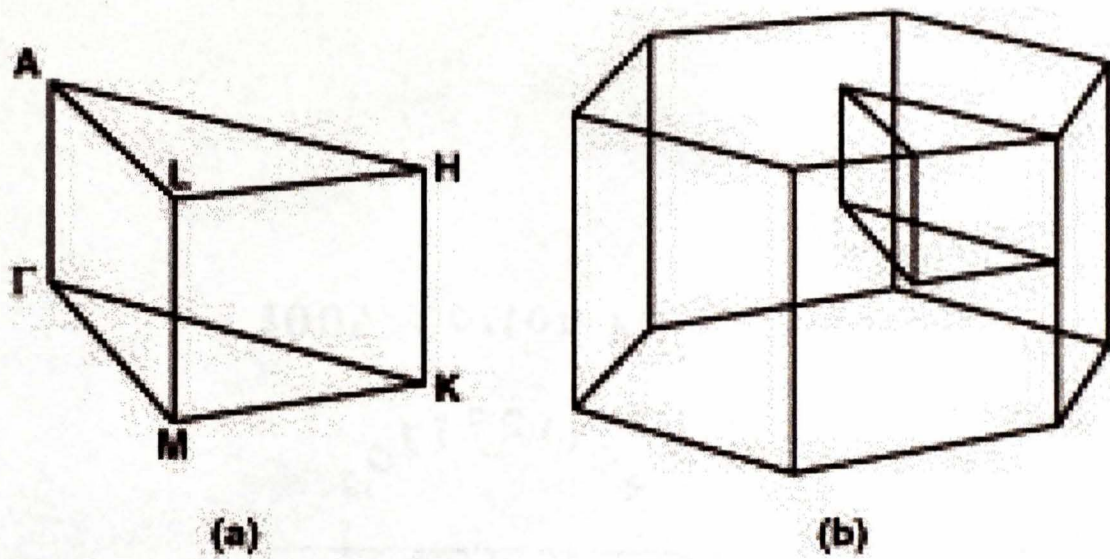
Fig. 2.1(a) Brillouin zone schematic including the various symmetry points within the irreducible wedge. (b) View of the full brillouin zone including the irreducible wedge.
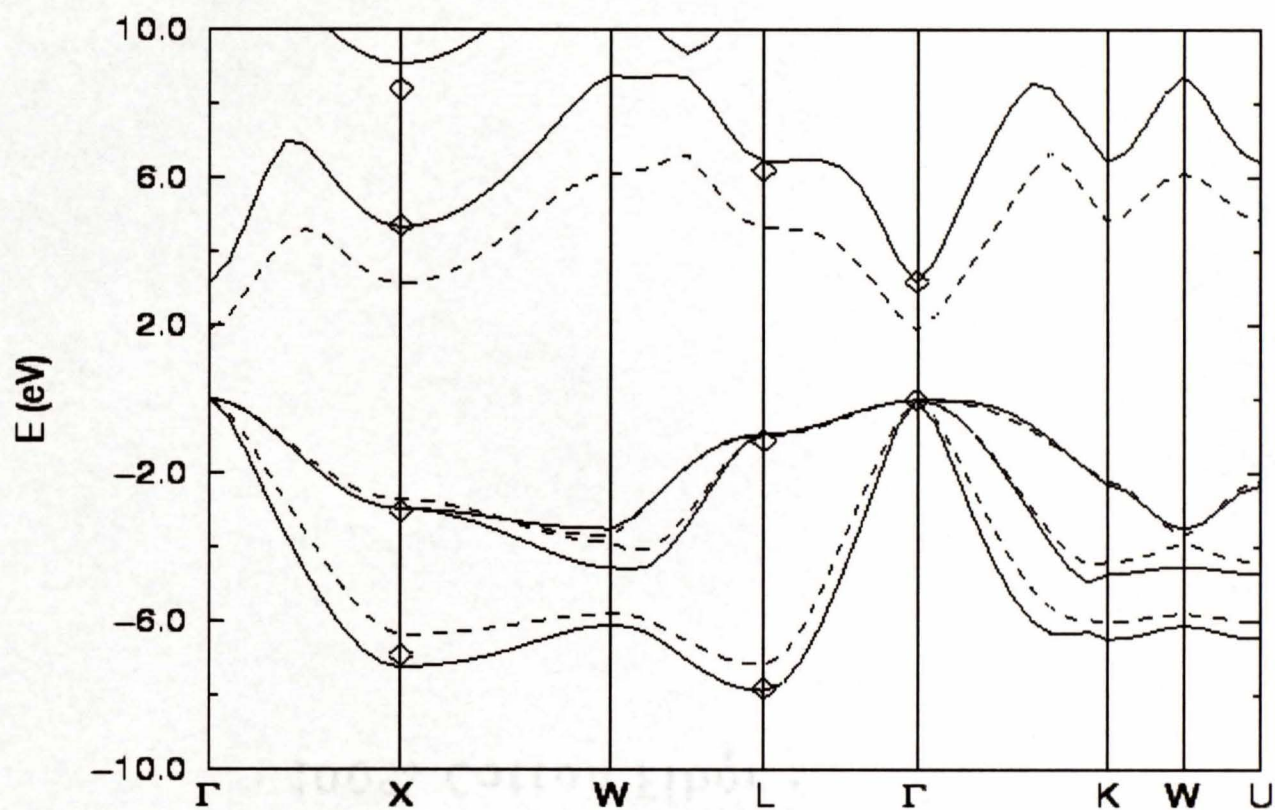
Fig 2.2 (a) Band-structures for zinc-blende GaN calculated with (i) first- principles method (dotted line) and (ii) semi-empirical pseudopotential method (solid line) [56].

GaN WZ
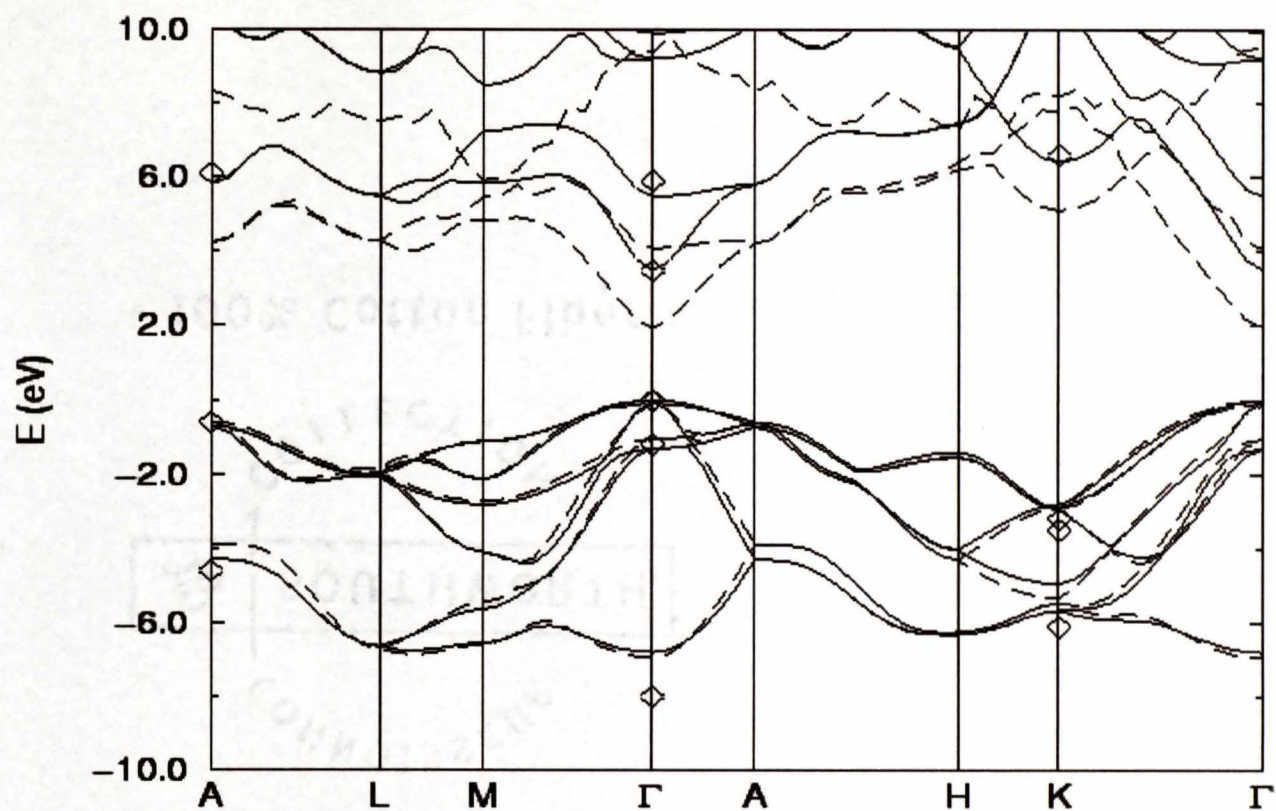
Fig 2.2(b) Band-structures for Wurtzite GaN calculated with (i) first- principles method (dotted line) and (ii) semi-empirical pseudopotential method (solid line) [56].

the electron effective mass is $0.19m_o$. For zincblende GaN, the experimental data yields an effective mass of $0.15 \, m_o$ [46].

The pseudopotential band structures along the main symmetry axes of the Brillouin zone are shown in Figs. 2.2(a) and 2.2(b) for zincblende and wurtzite GaN, respectively.

Although the two phases of GaN are very similar (both have direct fundamental gaps at the Γ point that differs by less than 10% in magnitude) their conduction bands appear to be sufficiently different to cause significant differences in their electron transport properties. For example, the nearest satellite valley in zinc-blende structure GaN (at the X point) is about 1.4eV above the conduction-band minimum, while the nearest satellite valley in wurtzite structure material (between the L and M points) is slightly more than 2 eV above the minimum. Furthermore, they noted the existence of a second conduction band at relatively low energy approximately 2.2 eV above the minimum at the Γ-point in wurtzite material. The second conduction band is considerably higher energy in zinc-blende GaN.

For wurtzite-phase GaN, the minimum is located at the Γ point. The satellite valleys are at the U point that is two thirds of the way between the L and M symmetry points. The next highest valley is located at the Γ_3 point. Thus, two Γ valleys and the six equivalent U valleys need to be considered for a reasonably accurate analysis. Some of the important material parameters of GaN at room temperature are listed in Table 2.1.

Differences in bandstructure between the two crystalline phases can be expected to play a role in affecting the electrical transport properties. For example, due to the slightly higher energy separation at the lowest Γ-point for the wurtzite phase, electrons

Table 2.1 Parameters used in the Monte Carlo calculations for wurtzite GaN.

PARAMETER	VALUE
Lattice constants in meter (a , c)	3.189 x 10^{-10} , 5.185 x 10^{-10}
Dielectric constants $k(0)$, $k(4)$	9.5 , 5.35
Density (gm cm^{-3})	6.095
Acoustic velocity (ms $^{-1}$)	4.33 x 10^{5}
Effective mass $m_{\parallel}$ (T_1 , U- and T_3-valley)	0.1846, 0.3858 , 3.6227
Effective mass m_{ζ} (T_1 , U- and T_3-valley)	0.2283, 3.03, 0.2856
Valley separation (eV)	0.0 , 2.2717 , 2.4
Nonparabolicity factors T_1 (eV^{-1})	0.37
Nonparabolicity factors U- valley (eV^{-1})	3.03 (m_{ζ}) and 0.385($m_{\parallel}$)
Nonparabolicity factors T_3 valley (eV^{-1})	0.22 (m_{ζ}) and 4.455($m_{\parallel}$)
Longitudinal optical phonon energy (eV)	0.092
Intervalley phonon energy (eV)	0.065
Acoustic deformation potential (eV)	8.0
Zero-order equivalent intervalley deformation potential (eV/cm)	0.5 x 10^{9}
Zero-order nonequivalent intervalley deformation potential (eV/cm)	1.0 x 10^{9}
First-order intervalley potential (eV)	5.0

are expected to require higher external electric fields in order to transfer to the satellite valleys. Consequently, the threshold voltage for the intervalley transfer effect that is at the heart of the NDR in Gunn diodes will be higher. Despite, such differences, however, many of the general features and trends for both GaN phases can be expected to remain very similar. For instance, the large bandgap (as compared to most other semiconductors of interest and commercial application at the present time) should lead to a high breakdown field and allow for the application of much higher device biasing. This, in itself, would help provide higher power-handling capability. Furthermore, this property should help in device miniaturization, which leads to increased electric fields, since this material can withstand higher fields.

2.3.2 COMPARISION BETWEEN THE GaN AND GaAs MATERIAL PROPERTIES

In this section, some of the important material properties of GaN are reviewed and comparisons made against the more commonly used GaAs material, to highlight the potential advantages as listed in Table 2.2. Some of the important advantages and superiority of GaN material over GaAs, are discussed below:

High Current Gain: Characterization of the heterojunction field-effect transistors fabricated to date has revealed a strong enhancement in carrier densities [46], which should lead to higher currents. This enhancement is thought to arise from strong piezo-electric fields in the GaN and AlGaN layers due to lattice mismatch strain between the two materials. Due to the high electron densities that are thus generated, higher current

Table 2.2   Comparasion of Material Parameters of GaN and GaAs.

Properties	GaN	GaAs
Threshold Electric Field	150 KV/cm	3.5 KV/cm
Separation between high and low energy mobility valleys (ΔE)	2.1 eV	0.3 eV
Peak Velocity	$3*10^7$ cm/sec	$1.5*10^7$ cm/sec
Saturation Velocity	$2*10^7$ cm/sec	$0.6*10^7$ cm/sec
Electron low-field mobility	280 cm^2/Vs	8000 cm^2/Vs
Peak Negative Differential Mobility	50 cm^2/Vs	2500 cm^2/Vs
N X L (N-L product); N -> electron concentration L -> thickness of the diode.	$8.2*10^{12}$cm^{-2}	$1*10^{10}$ cm^{-2}
N_{crit} (Critical Doping)	$4.3*10^{18}$ cm^{-3}	$3.4*10^{15}$ cm^{-3}

results. Consequently, the AC gain is expected to be large and strong amplification with a high current swing should result. From this standpoint, GaN Heterojunction Field Effect Transistors (HFETs) offer bright prospects for use in both small and large-signal amplification, particularly at the X-band and higher frequencies.

Wide band-gap: The lattice structure guarantees a band-gap in the 3.3-3.6 eV range depending on the GaN crystal type. This is much larger compared to the 1.41 eV bandgap of GaAs, which is the most commonly used direct bandgap semiconducor material. As a result of this large band-gap for nitrides, devices based on nitrides can have a large breakdown voltage, higher-power handling capability, lower noise and radiation hardness. The wide band-gap effectively prevents electrons in the valence band from making transitions to the conduction band. This cuts down on the background free-carier population, and leads to low noise and small dark currents in ultraviolet (UV) detectors.

Thermal Stability: This property is very important for high power applications. The higher thermal conductivity parameter helps in transporting heat away from internal hot spots and sources of heat generation. This makes thermal management and control easier in GaN-based electronic devices and guarantees that thermal runaway conditions can be avoided. This is a particularly important issue in the context of device miniaturization and density enhancements. With more electronic devices of a chip, the Joule heat produced internally as all of the devices operated can be quite substantial. Hence, thermal management and rapid heat dissipation remain important considerations. The thermal stability also helps enhance the power handling capability of the GaN devices.

High Frequency: GaN can be used with its alloys (such as AlGaN) to form heterostructure devices. Such devices have high carrier drift velocities due to the suppression of the impurity scattering. The overall result is an increased transconductance with carrier drift velocities in GaN almost a factor of two larger than those in GaAs. This allows for faster speeds and a better high-frequency response for GaN relative to GaAs at high operating voltages. Though GaAs too can be used to form heterojunction devices with AlGaAs alloys, the electron densities obtainable are substantially lower due to the absence of a strong piezoelectric effect. Hence, the GaAs system is not capable of providing as large currents at high frequencies as GaN. In GaN, however, the presence of a strong internal polarization arising from the spontaneous and piezoelectric effects work to create stronger band bending and contributes to very high sheet carrier densities, even in the absence of intentional doping.

Comparision of other important material properties: When a high electric field is applied to bulk semiconductors such as GaN or GaAs, electrons experience a negative differential mobility. Under these conditions, a non-uniformity of electron concentration grows at a rate inversely proportional to the differential dielectric relaxation time Γ_{DDR} which is equal to $\varepsilon/q\mu_{NDR}N$, where N is the electron concentration and μ_{NDR} is the peak negative differential mobility. It is expected that the domain growth lasts for at least 3 times differential dielectric relaxation time[47]. The critical values of the N-L product for GaN and GaAs is given in Table 2.2 where L is the thickness of the device. This product is calculated by using the following equation:

$$N * L > 3 * \varepsilon * v_{Peak} / q * \mu_{NDR} , \qquad\qquad (2.1)$$

Where ε is electric permittivity and q is the electron charge. And to avoid the formation of static domains at the anode, N should not exceed a critical doping[48] concentration given by the equation:

$$N_{Crit} = \varepsilon * (F_{Th})^2 / q , \qquad\qquad (2.2)$$

where F_{Th} is the threshold electric field, ε is electric permittivity and q is the electron charge.

Regarding electron transport properties, the Γ-valley effective mass of GaN is 0.2, which is almost three times more than that of GaAs. Therefore, the mobility in bulk GaN is expected to be inferior compared to GaAs, which is shown in experimental work too. However, the high-field drift velocity of bulk GaN is larger than that of GaAs [49]. This is due to the higher inter-valley separation and the larger energy of optical phonons. The former helps keep a higher fraction of electrons within the lower mass valley, while the latter reduces the net role of phonon scattering by increasing the emission threshold. The threshold field for intervalley transfer is much larger in GaN than in GaAs as listed in Table 2.2. The increased value of threshold field is caused by a larger separation between the high and low mobility valleys in GaN compared to GaAs in Table 2.2. Since most devices are operated under high electric field conditions, it is the drift velocity and not the low-field mobility that is an important parameter for consideration.

The capability of GaN to sustain a high peak velocity up to much higher temperatures than in GaAs may work in its favor in some high power applications [28].

2.4 MICROWAVE DEVICES

The need to use microwave technology for generation, amplification and signal processing applications has led to considerable research on semiconductor based electronic devices. Such solid-state elements have numerous advantages over vacuum-tube components for microwave applications that include speed, high density, compactness, and superior data handling capability. Research over the years has resulted in the development and fabrication of a large variety of solid-state devices in bulk semiconductors. Included among these are the: tunnel diodes, Varactor diodes, IMPATT (IMPact Avalanche Transit Time) and BARITT (BARrier Injected Transit Time) devices and Gunn-effect oscillators. The tunnel diode is associated with the quantum tunneling phenomena. The tunneling time across the device is very short, permitting its use well into the millimeter-wave region. However, this is a low power device since the current levels remain fairly low. Given its mature technology, the tunnel diode has been used in special low-power microwave applications, such as local oscillators and frequency-locking circuits. Tunnel diodes do exhibit a negative differential conductance (NDR) region in their electrical current-voltage characteristic. They are capable of operating up to frequencies in excess of 100 GHz, because of the inherently speed tunneling of electrons through the potential barrier of a p-n junction. However, since the tunnel effect, and hence the range of negative conductance, is restricted to voltages less than the band-gap of the semiconducting material, the attainable radio-frequency (RF) power levels

have traditionally been disappointingly low. In addition, both the power dissipating capability and the ruggedness of the tunnel device usually suffers if sizes are reduced to lower the parasitics. Gunn diodes are another class of high-frequency microwave devices, and are commonly referred to as Transferred Electron Diodes (TED). The TED was invented and realized by Gunn in 1963[50]. The TED is used extensively in such millimeter-wave applications as detection systems, remote controls, and microwave test instruments. The IMPATT (IMPact Avalanche Transit Time) diode was first discovered by Johnston et al. in 1965 [51]. IMPATT diodes can generate the highest continuous wave (CW) power at millimeter-wave frequencies of all semiconductor devices. They are used in radar systems and alarm systems. However, it must be pointed out that the devices and their electrical outputs briefly surveyed in this section, inherently allude to conventional semiconductor materials such as GaAs and InP. Many of their shortcomings are associated with the bandgap of the parent material. However, with the development of high bandgap materials such as GaN, this shortcoming is likely to be overcome and so device performance is likely to be much better.

In Varactors, the junction depletion capacitance is made to change through variations in the applied reverse bias to produce an NDR effect. There are, however, two additional difficulties associated with such a structure. First, since destructive avalanche multiplication can occur with very high reverse bias, a natural limit for the useful operating range of the diode is automatically set. Secondly, it is not an active oscillator and requires the presence of passive circuit elements. In another family of devices, represented by the IMPATT, TRAPATT (TRApped Plasma Avalanche Trigged Transit), and BARITT diodes, the desired NDR is achieved by controlling the phase shifts between

the device current and applied voltage by a two-step process. The first involves an avalanche breakdown inside a reverse biased p-n junction controlled by an applied RF field. This process introduces a 90 degree phase lag in the current waveform. The subsequent carrier drift along the device contributes to an additional phase delay. The total 180 degree phase shift then gives rise to the negative power dissipation mechanism. There are, however, two noteworthy difficulties with the transit time devices for circuit applications: (i) the noise is high, and sensitive to operating conditions due to large avalanche multiplication. Since avalanche multiplication is a random, stochastic process, the current tends to be very noisy and non-uniform in time. (ii) The large electronic reactances present are strongly dependent on oscillation amplitudes, and require unusual care in circuit design to avoid detuning or even burnout of the diode. In addition, thermal and shot noise associated with the p-n junction and the avalanche process, are responsible for the performance degradation.

Due to the above disadvantages, consideration was given to the possibility of producing bulk negative conductance in a homogeneous semiconductor (i.e., materials without p-n junctions) for the generation and amplification of RF signals. It seemed likely that by abandoning p-n junctions, with their restricted active volume and their associated capacitances, it might be possible to achieve higher RF powers and frequencies, reduce noise levels with the added advantage of simpler manufacture. Such a microwave oscillator based on a bulk semiconductor effect was made possible with the discovery of the Gunn effect [52].

The Gunn diode operation is based on the transferred electron effect, which arises from the bulk properties of semiconductors and does not depend, on either the junction or

contact properties. In addition, the effect is independent of total voltage or current, and is not affected by magnetic fields or different types of contacts [53]. Furthermore, it occurs in n-type materials only, since it results from transitions within the electronic band-structure, and not the hole/valance bands. The occurrence of such transitions requires internal electric fields above a certain critical threshold within the semiconductor. It has been found that for most materials (e.g. GaAs and InP), a threshold value of 3.3 KV/cm must be exceeded if oscillations are to take place. The mechanism responsible for the negative differential resistance in this device is a field-induced transfer of conduction band electrons from a low-energy, high mobility valley to high-energy, low-mobility satellite valleys is shown in Fig 2.3. The detailed description of this mechanism in pure semiconductors involves knowledge of the band structure, the strength of interaction between electrons and phonons, and the phonon spectrum.

The most detailed theoretical treatments of the Gunn effect have relied heavily on Monte Carlo computer simulations of the electron dynamics involved. The work presented here also involves the same Monte Carlo Computer simulation to simulate the transient electron dynamics and to obtain the velocity-field curves that are required to find the characteristics of the Gunn diode. A detailed discussion of this simulation is presented in the next chapter. For the present, the transferred electron effect is explained in detail along with the mechanism responsible for the negative conductivity.
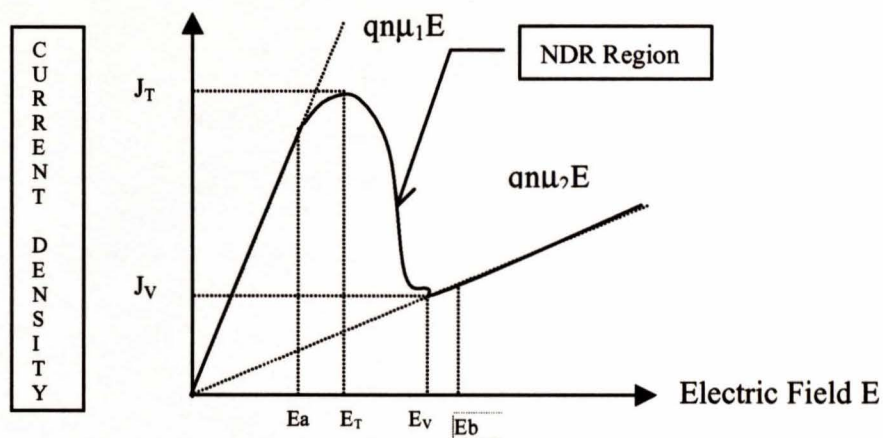
Fig 2.3   Current density versus Electric Field profile of a two-valley semiconductor.
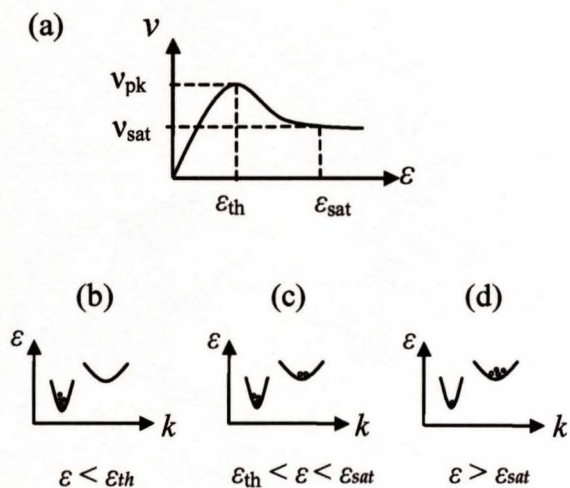
Fig 2.4 (a) Electron Velocity versus Electric Field profile of a two-valley semiconductor.

(b), (c), (d) Transfer of electrons from low-energy high mobility to high-energy low mobility satellite valleys as the Electric field is increased (th $\rightarrow$ threshold, sat $\rightarrow$ saturation, pk $\rightarrow$ peak, ε $\rightarrow$ electric field, v $\rightarrow$ velocity).

2.5   NEGATIVE DIFFERENTIAL RESISTANCE

In the previous section, the transferred electron diode was introduced and its operational principle briefly discussed in terms of the transferred electron effect i.e., the transfer of conduction electrons from a high-mobility lower energy valley to low-mobility higher energy satellite valleys. This can be better explained in terms of the following current-versus-electric-field characteristic of a two-valley semiconductor.

$$J = qn\mu_1 E \quad \text{for} \ \ 0 < E < E_a \tag{2.3}$$

$$J = qn\mu_2 E \quad \text{for} \ \ E > E_b \quad , \tag{2.4}$$

Where J is the current density, E is the applied electric field, q is the electron charge, n is the carrier concentration, μ_1 and μ_2 are the electron mobilities in the satellite valleys. If $\mu_1 E_a$ is larger than $\mu_2 E_b$, there is a region of negative differential resistance between E_a and E_b as shown in Fig 2.3. The other parameters are as follows: E_t is the threshold field corresponding to the onset of the NDR, J_t is the threshold current density, E_v is the valley field and the corresponding current density is $J_v.$ The NDR region is between E_t and $E_v.$

For the transferred-electron mechanism to give rise to the NDR, certain requirements must be met. (a)The lattice temperature must be low enough that in the absence of an electric field most of the electrons are in the lower valley (the conduction band minimum), that is the energy separation between the two valleys $\Delta E > kT$. (b) In the lower valley the electrons must have high mobility and small effective mass, whereas in the upper satellite valleys the electrons must have low mobility and large effective mass.

(c) The energy separation between the two valleys must be smaller than the semiconductor bandgap (i.e., $\Delta E < E_g$) so that avalanche breakdown does not begin before the transfer of electrons into the upper valleys. Some of the semiconductors satisfying these requirements are n-type Gallium Nitride, n-type Gallium Arsenide and n-type Indium Phosphide.

2.6 OPERATING MODES OF GUNN DEVICES

In this section, a brief review and discussion of the various modes of operation of Gunn diodes is presented. Space-charge growth for a device with negative differential mobility is elucidated. The goal of this is to demonstrate that spatially heterogeneous charge distributions are necessary for the occurrence of microwave oscillations in the bulk semiconductor devices. Various other modes of device operation are then discussed.

2.6.1 SPACE-CHARGE GROWTH MECHANSIM

A semiconductor exhibiting NDR is inherently unstable because a random fluctuation of carrier density at any point in the semiconductor can produce a momentary space charge that will grow exponentially with time. The one-dimensional continuity equation is given by :

$$\partial n/\partial t = (1/q)*(\partial J/\partial x) \quad , \tag{2.5}$$

where n is the carrier concentration, q is the electron charge, and J is the current density. If there is a small local fluctuation of the majority carriers from the uniform equilibrium

concentration n_o, the locally created space charge density becomes $n-n_o$. The Poisson's

equation and the current density equations for such a perturbative condition then, are :

$$\partial E/\partial x = -q(n-n_o)/\varepsilon_s \quad , \tag{2.6}$$

$$\text{and , } J = q\, n_o\mu E + qD(\partial n/\partial x) \quad , \tag{2.7}$$

where μ is the average mobility, ε_s is the dielectric permittivity, and D is the diffusion

constant. Differentiating eqn. 2.7 with respect to x and using Poisson's equation yields:

$$(1/q)\, \partial J/\partial x = -((\,n-n_o)\, qn_o\mu/\,\varepsilon_s) + D(\partial^2 n/\partial x^2) \quad . \tag{2.8}$$

Substituting this expression into eqn. 2.6 gives

$$\partial n/\partial t = -((\,n-n_o)\, qn_o\mu/\,\varepsilon_s) + D(\partial^2 n/\partial x^2). \tag{2.9}$$

The above equation can be solved by separation of variables. For the temporal response,

the solution for the above equation is :

$$n-n_o = (\,n-n_o)_{t=0}\, \exp(-t/\Gamma_R) \quad , \tag{2.10}$$

where Γ_R is the dielectric relaxation time given by :

$$\Gamma_R = \varepsilon_s/qn_o\mu \quad . \tag{2.11}$$

Γ_R represents the time constant for the decay of the space charge to neutrality if the mobility μ is positive. However, if the semiconductor exhibits NDR, any charge imbalance will grow with a time constant equal to $|\Gamma_R|$. If the above equation has to remain valid throughout the entire transit time of the space-charge layer, the maximum growth factor would be $\exp(L/v|\Gamma_R|)$, where L is the length of the active region and v is the average drift velocity of the space-charge layer. For large space-charge growth, this growth factor must be greater than unity, making $L/v|\Gamma_R| > 1$, or

$$n_o L > \varepsilon_s v/(q\mu) = 10^{12} \, cm^{-2} \text{ for GaAs and InP and } 5 \times 10^{12} \, cm^{-2} \text{ for GaN} . \qquad (2.12)$$

An important mode of operation for the TED is the transit-time domain mode. When there are positive and negative charges separated by a small distance, we have a dipole formation which is called a domain. From poisson's equation, we find that the electric field inside the dipole would be greater than the field on either side of it. The corresponding voltage variation across the device can be obtained by integrating the Poisson's equation once more. Because of the NDR, the current in the low-field region would be greater than that in the high-field region. The two field values tend toward the equilibrium level outside the NDR region, where the high and low currents are the same. The dipole has now reached a stable configuration. The dipole layer moves through the active region and disappears at the anode, at which time the field begins to rise uniformly across the device through the threshold (i.e., $E > E_t$), thus forming a new dipole, and the process repeats itself. The time required for the domain to travel from the cathode to

anode is L/v, where L is the active device length and v is the average velocity. The corresponding frequency, f, for the transit time domain mode is f = v/L.

2.6.2   MODES OF OPERATION

Since Gunn first observed oscillations in a GaAs rod [54] several operating modes have been studied. Out of them, Gunn and the LSA modes are concerned with the operation of the Gunn diode. The Gunn mode is in turn sub-divided into (i) Accumulation Layer Mode; (ii) the Transit-time or Fundamental Mode; (iii) the Quenched Mode; and (iv) the Delayed Mode [54].

Of these, the accumulation layer mode is characterized by an n_oL product value of less than 10^{12} cm^{-2}. The device doping levels and the transit lengths are inadequate for the space-charge growth to stabilize. A continually growing accumulation layer propagates towards the anode. This in turn causes a time-dependent variation in the internal electric field as shown. The net integral of this field curve, however, remains constant for a steady state DC bias voltage.

The Transit-time Dipole Layer mode of operation is made possible in a device if the n_oL product exceeds 10^{12} cm^{-2}. This mode is characterized by a stable dipole layer containing a high–field region, that neither grows nor shrinks with time. The high field domain is nucleated close to the cathode and travels the full length of the sample to the anode. The frequency of operation is then controlled by the transit time and hence is inversely dependent on the device length. This mode is already explained above clearly.

In the quenched Dipole Layer mode, the device operates at frequencies higher than those made possible from the transit time concept. In this mode, the device behavior

is controlled through an external resonant circuit, which effectively sets the voltage across the device. As the voltage begins to decrease in response to the circuit oscillations, the internal dipole width shrinks, until it is completely quenched. As a result, the overall result traversed by the dipole domain is less than the total device length.

Finally, in the Limited-Space-Charge Accumulation (LSA) Mode of operation, the electric field across the device rises from below the threshold value and falls back again so quickly that the space-charge distribution associated with high-field dipole-layers does not have sufficient time to form. Only a primary accumulation layer forms near the cathode; the rest of the device remains fairly homogeneous, provided that the doping fluctuations are sufficiently small to prevent the formation of dipole layers. Under these conditions, a large portion of the device exhibits a uniform field, and the power generation at the circuit-controlled frequency is affected by the negative differential mobility of individual electrons rather by the movement of space-charge bunches. The LSA mode is particularly suitable for microwave power generation because of its relatively high efficiency and operating frequency.

2.7 METHODS OF IMPROVING DEVICE PERFORMANCE

Thus far, a review has been made on the physical characteristics of Gunn devices and mainly assumed that the devices are made from GaN or GaAs. In this section, it is shown that the use of alternative heterojunction structures and different semiconductor material improves the high frequency device performance.

Usually, Gunn devices are associated with a dead zone. This is a characteristic distance that the electrons have to traverse before they can acquire sufficient energy from

the applied electric field and attain the threshold velocity. The dead zone serves no useful purpose and delays the generation of microwave power. The situation becomes more acute for high frequencies, which require shorter transit lengths. These size reductions worsen the situation since the relative percentage of the dead zone gets larger. In addition, the temperature variations also have an adverse effect on the dead-zone formation. Typically temperature fluctuations alter the phonon populations within the device and bring about changes in the intervalley phonon-assisted transfer. The net result of this temperature dependence of the intervalley dynamics is a degradation in the device performance and enhanced uncertainty in the successful growth and formation of the instability [55].

In order to overcome these drawbacks of device scaling at high frequencies, one needs to set up schemes for reducing and stabilizing the dead-zone. The simplest method for doing so involves the use of alternative semiconductor materials that have a smaller electronic mass and/or intervalley transfer threshold energy. This scheme however, is not always feasible since the semiconducting material may not simultaneously have a low electronic mass and intervalley separation. For example, InAs has a lower effective mass than GaAs but a much higher value of $E_{\Gamma\text{-}L}$. Furthermore, technological difficulties may prevent a successful device fabrication [56].

The above difficulty can, however, be overcome through the use of alternative heterostructures formed by joining dissimilar semiconductors. The basic concept is to use differences in the bandgaps of two semiconductors placed adjacently for creating energetic hot electron conditions. The cathode region is typically fabricated from a wide bandgap material and acts as the "hot electron injector". The middle drift region has a

lower bandgap and comprises the main transit region, as shown. The difference in the electronic band offsets caused by the dissimilar bandgaps is used to convert the potential energy at the cathode into large kinetic energy in the drift region. Electrons are therefore propelled into a high-energy state as they begin their transit.

The limitations to the microwave power obtainable from Gunn oscillators are a result of the heating of the device and the dielectric breakdown field of GaN. Any heating effects which can be removed will add to both the power and the efficiency. Ondria and Ross [56] have shown that by grading the doping profile in the transit region of a conventional Gunn diode, it is possible to improve the diode's performance. The attraction of varying the doping in the transit region in a logarithmic manner from high at the cathode to low at the anode, is that the electric field throughout the transit region is much more uniform when the device is operated. This reduces excessive heating of electrons by the field near the anode and leads to a higher efficiency. Hence, their mobility becomes less. As a result, their collective drift velocity decreases, and the ensemble attains a steady-state velocity. This final steady state velocity is determined by the material parameters and physically represents a dynamic equilibrium between the Γ_1 $\rightarrow$ L-M valley, and vice versa. The steady state velocities are lower at higher fields because a larger fraction of electrons occupy the higher mass valleys (i.e. the L-M, and Γ_3).

For low electric fields such as 10^7 V/m and 1.7 x 10^7 V/m, the drift velocity rises more slowly than at the higher fields. The steady state values are correspondingly high as most of the electrons will continue to be in the lower valley that has a higher mobility.

CHAPTER III

NUMERICAL SIMULATION SCHEME

3.1 INTRODUCTION

In using semiconductor devices, our principal goal is to determine the behavior of currents and voltages at the device terminals due to an applied stimulus which could be either an external bias or a thermal perturbation as a function of time. To fulfill this goal, we need to describe the behavior of the carriers in the device.

There are many simulation schemes but most of them are inaccurate and can be applied only under specific conditions. The simplest method is drift-diffusion scheme [57] but it ignores the distribution of carriers and takes into account average carrier densities.

The equation governing the motion of carriers in a drift-diffusion scheme is:

$$J = nqv_n + pqv_p - qDn\nabla n + qDp\nabla p , \qquad (3.1)$$

where J is the current density, n and p are the electron and hole densities, D_n and D_p are the electron and hole diffusion coefficients, v_n and v_p are the electron and hole drift velocities and q is the electron charge. The validity of Drift-diffusion scheme requires the following assumptions.

1. Anisotropic and parabolic single band

2. Inherent assumption of the relaxation time approximation

3. Homogeneous collision time

4. Absence of degeneracy

5. Absence of strong off- equilibrium effects

The limitations in the drift diffusion scheme are mostly addressed by a method called Boltzmann Transport approach. In this approach the dynamic distribution function f under non-linear conditions, is described by Boltzmann transport equation (BTE) [58]. The rate of change of distribution function is given by:

$$\partial f / \partial t = -(\mathbf{v} \cdot \partial f / \partial \mathbf{r}) - (e/\hbar) \mathbf{F} \cdot \partial f / \partial \mathbf{k} + (\partial f / \partial t)_{coll} , \qquad (3.2)$$

where F is the applied field, and $(\partial f / \partial t)_{coll}$ is the rate of change of F due to collisions and scattering. The first two terms of the equation represent the variation of distribution function with density gradient and the applied electric field respectively. The solution of this equation requires an integral of the collision term. This integral yields exact an solution only under few simple cases and these cases are not applicable to real systems. In cases, that are applicable to real systems, Boltzmann transport equation can give approximate solutions in terms of distribution functions. The most used techniques are Legendre polynomial expansion [59] and the displaced Maxwellian approximation [60]. Therefore, the Boltzmann transport approach requires, for its validity, simple distribution functions and simplified band structure and so fails in the situations where the distribution is complicated such as in devices having very short dimensional structure.

The two most important numerical techniques are the iterative method [61] and the Monte Carlo Technique[62]. A statistical method known as the Monte Carlo method was proposed to solve complicated mathematical problems such as the cases where BTE becomes unacceptable or for very short dimensional devices. This method is easy to implement and has many advantages, as given below:

1. Time and space dependent phenomena can be easily simulated.

2. Stochastic calculation is achieved at a minimum level of difficulty while incorporating memory effects.

3. The microscopic interpretation of the physical details is quite transparent.

4. Easily includes system memory effects and hence all non-Markovian behavior.

5. Arbitrary shapes and geometries as well as complicated boundary conditions can be easily analyzed.

6. The analysis can be extended to fluctuation phenomenon and hence noise properties can be calculated.

7. No arbitrary assumption regarding the distribution function be made.

8. Temperature gradients and fields (both electric and magnetic) can all be included.

Monte Carlo simulation was born well before its applications to the transport problems and has been applied to a number of scientific fields. This method was first applied to transport in semiconductors by Kurowasa [63] to study steady-state hole transport in Ge. Fawcett et. al. [64] extended this method for GaAs material where different scattering processes and a complex band structure needs to be incorporated. The physical interpretation of a numerical solution is the most important step in any simulation, and the Monte Carlo technique is particularly useful to achieve this goal, since it permits the observation of simulated physical situations unattainable in experiments, or even the investigation of a nonexistent material in order to emphasize special features of phenomena under study.

3.2   THE MONTE CARLO METHOD:

The Monte Carlo method, as applied to charge transport in semiconductors is the simulation of the motion of one or more electrons inside the crystal, subject to the action of external forces due to applied electric or magnetic fields and of given scattering mechanisms. The motion consists of a sequence of free flights continuously interrupted by instantaneous scattering events. This approach is semi-classical in a sense that the particles are treated as classical point like objects, but the scattering rates are determined using quantum mechanical theory. During the free flight, electrons obey classical laws of motion and drift in the existing electric field. The free flight time, the type of the scattering event and the final state of the electron after the occurrence of scattering are all taken as random quantities that are selected in accordance with some given probabilities. The probability distribution functions for these random quantities can be expressed in terms of transition rates due to various processes and the strength of the electric field. But the physical distributions may be quite complex and difficult to manipulate even with a computer. This problem can be solved by mapping the complex distributions on to a simple pseudo-random distribution [65]. The most easiest and the convenient pseudo-random distribution is nothing but the uniform distribution, which is available on most of the systems.

In general, if $p(q)$ and $p(r)$ are the respective probability densities, associated with q in the physical distribution and r is the pseudo-random distribution, then:

$$\int_0^q p(q') \, dq' = \int_0^r p(r') \, dr' \quad . \tag{3.3}$$

We know that in a uniform distribution p(r)=1, so we get

$$r = \int_0^q p(q') \, dq' \quad .$$

(3.4)

Hence, provided that this integral can be evaluated in a simple closed analytic form, inversion will yield a random value for the physical variable q in terms of the uniformly distributed random number r. As a consequence, any Monte Carlo method relies on the generation of a sequence of uniformly distributed random numbers corresponding to various random processes involved.

It is sufficient, in general to simulate the motion of one single electron when the purpose of analysis is the investigation of a steady-state, homogeneous phenomenon. So, we may assume that a sufficiently long path of this simple electron will give information on the behavior of all the carriers. But on the contrary when the purpose of analysis is not homogeneous, it is necessary to simulate the motion of an ensemble of charge carriers and evaluate over the time the ensemble average of the quantities that are of interest. This method is known as Ensemble Monte Carlo (EMC) method. The program flow is summarized in Figs. 3.1 and 3.2.

3.2.1 DEFINITION OF PHYSICAL SYSTEM

The starting point of the program is the definition of the physical system of interest, which includes the parameters of the material, values of the physical quantities and simulation conditions such as lattice temperature, electric field and the terminal bias.

The parameters that control the simulation such as the number of the electrons simulated, duration of each sub-history, total time, the desired precision of the results are also defined. The scattering rates are normalized and stored in a tabulated form.

3.2.2 INITIAL CONDITIONS

This step involves choosing the initial position, momentum, and the energy of the electrons. Uniformly distributed random numbers are used to select the initial position and direction of motion of the electrons. The electrons reside in the lowest valley initially and are assumed to be in a state of initial thermal equilibrium. For simulations involving photo-excitation, the initial state lies in the lowest direct valley with an energy equal to the excess energy of external excitation. The momentum at this initial state is generally distributed randomly. This is reasonable for unpolarized light. But for situations involving polarized radiation or in the case of electrical carrier injection from a contact, the distributions would be suitably modified.

3.2.3 FLIGHT DURATION:

After setting the initial conditions, the first step is to calculate the free flight time for each electron which depends on the scattering probability. The processes that scatters the electron at the end of each free flight is characterized by a transition rate $Sn(\mathbf{k},\mathbf{k'})$ i.e., from the momentum state $h\mathbf{k}$ to $h\mathbf{k'}$. Depending on the number of processes n changes its values say from n=0 to N if there are N different processes. The total scattering rate from the state $\mathbf{k}$ to $\mathbf{k'}$ because of nth process is given by

$$\lambda n(\mathbf{k}) = \int Sn \ (\mathbf{k},\mathbf{k'}) \ dk' \qquad . \qquad\qquad (3.5)$$

Therefore, the total scattering rate due to all processes is:

$$\lambda(\mathbf{k}) = \sum_{n=1}^{N} \lambda n(\mathbf{k}) \quad , \qquad (3.6)$$

where $\mathbf{k}$ is a function of time. Generally the total scattering rates are only functions of $|\mathbf{k}|$, so $\lambda(\mathbf{k})$ can be easily transformed to $\lambda(E)$. Thus, if $\lambda(\mathbf{k})dt$ is the probability that an electron in the state $\mathbf{k}$ suffers a collision during the interval dt, the probability that an electron which suffered a collision at time t=0 has not yet suffered another collision after a time 't' is given by the following expression:

$$\exp\left(-\int_{0}^{t} \lambda[\mathbf{k}(t')] \; dt'\right) \qquad . \qquad (3.7)$$

So, the probability that the electron will suffer its next collision during interval dt around dt is given by :

$$P(t)dt = \lambda[\mathbf{k}(t)] \exp\left(-\int_{0}^{t} \lambda[\mathbf{k}(t')] \; dt'\right) dt . \qquad (3.8)$$

The probability density $P(t)$ is therefore given by

$$P(t) = \lambda[\mathbf{k}(t)] \exp\left(-\int_{0}^{t} \lambda[\mathbf{k}(t')] \; dt'\right) . \qquad (3.9)$$

Using the above equations, a uniformly distributed random number r can be used to describe the process, which gives

$$r = 1 - \exp\left(-\int_{0}^{t} \lambda[\mathbf{k}(t')] \; dt'\right) . \qquad (3.10)$$

The above equation is very complex and cannot be solved for t analytically. But for each electron energy, numerical integration can be performed to produce r and t in tabular form. This obviously is time consuming.

A new technique for overcoming this difficulty has been proposed [65,66]. It involves the addition of a term that represents a virtual scattering process. This term is added to the real scattering process in order to make the total scattering rate constant. This virtual scattering process is taken such that it does not affect the state of the electron. This mechanism is usually referred to as "self-scattering" or "null collision". Thus the total scattering rate for each electron including virtual process is given by the following expression:

$$\lambda_T (k) = \lambda (k) + \lambda v (k) = \Gamma .$$

(3.11)

Equation (3.10) reduces to the following form:

$$r = 1 - \exp(-\Gamma t) \quad ,$$

(3.12)

$$i.e., \quad t = -1/\Gamma \ \ln (1-r).$$

(3.13)

Hence, the flight time can be easily determined from the uniformly distributed random number r. The scattering rate should be chosen in such a way that it should be equal to the maximum value of $\lambda(k)$ in the region of **k** space of interest. This should be done to avoid any negative values for the virtual scattering rate $\lambda v(k)$. The state **k** of the electron remains unchanged if the electron undergoes a self-scattering. The computer time that is wasted in computing the self-scattering events is more than compensated for by the simplification of the calculation of the free flight time.

3.2.4 FREE FLIGHT

The electrons drift freely under the influence of the electric field and during this free flight, the electron wave vector **k** changes continuously according to the Newton's

laws of motion. The flight comes to a halt after scattering occurs and the parameters of interest such as the position, momentum and energy of the electron are recorded at the end.

3.2.5 SELECTION OF SCATTERING MECHANISM

The selection of scattering mechanism for given applied electric field E, depends on the normalized probability. The normalized probability $P_j(E)$ for a given scattering mechanism j is given by the equation

$$P_j(E) = \lambda_j(E) / \Gamma \quad . \tag{3.14}$$

The selection of scattering mechanism is made by generating a random number r between 0 and 1. The selection of jth scattering mechanism depends on the following inequality :

$$\sum_{i=1}^{j-1} P_i(E) < r < \sum_{i=1}^{i=j} P_i(E) \quad , \tag{3.15}$$

$$\text{i.e., } \quad r > \sum_{i=1}^{N} P_i(E) \quad , \tag{3.16}$$

is the condition for self scattering. Here N is the total number of scattering mechanisms. Therefore, the inequality

$$r < \sum_{i=1}^{m} P_i(E) \quad , \tag{3.17}$$

is tested for all possible values of m ranging from 1 to N and then is selected if the inequality is satisfied.

3.2.6 CHOICE OF STATE AFTER SCATTERING

Once the scattering mechanism that caused the end of the flight is determined, the new state of the electron after scattering must be chosen, say **k'**. But if a self-scattering occurs then the new state is nothing but the previous state say **k**. A new flight time Δt is added to the time t and this goes on until a real scattering event is selected. When a real scattering event is selected, **k'** is chosen stochastically according to the differential cross-section of that particular mechanism. The final energy equals the initial energy if ionized impurity scattering or acoustic scattering is selected because of the elastic nature of the collision, but on the other hand if an inelastic process such as polar optical or inter-valley scattering is selected, the energy of the electron is changed. The change in momentum always occurs whether the scattering mechanism is momentum randomizing (inter-valley, acoustic scattering) or non-momentum randomizing (polar optical, ionized impurity scattering) process. Optical phonons add or extract a constant quanta of energy 'hω' through emission or absorption.

The determination of the new wave vector after the phonon scattering process needs generation of random numbers which can be used to determine the azimuthal angle θ and angle φ according to the angular dependence of the scattering mechanism selected. The angle φ after the scattering can take any value between 0 to 2π with equal probability, so that the angle can be chosen using a random number r in a way given by the following expression:

$$\phi = 2\pi r \quad . \tag{3.18}$$

The azimuthal angle, on the other hand, depends on the nature of the scattering process. If the scattering process is momentum randomizing process, then θ is given by :

$$\theta = \cos^{-1}[(2r-1)] \quad . \tag{3.19}$$

For other scattering mechanisms that have a directional dependence, θ can be selected by generating a random number and mapping the distribution to a uniform distribution [67].

After each and every scattering event, the momentum and the energy of the electron are updated while the position of the electron remains unchanged as the scattering is considered to be instantaneous. The process repeats as the electron begins its next flight and the scattering mechanism repeats till we reach the end of the simulation. The data collected after each and every free flight is used in ensemble method to determine the average values of the quantities of interest.

3.3   SCATTERING MECHANISM IN GaN

The motion of electrons is free in a perfect crystal, but if there is any external electric field, the electron uniformly accelerates. This linearly increases its drift velocity with time in the direction of the field. Such a linear increase in drift velocity with time is not observed in any real crystal. The average electron drift velocity reaches a limiting value, which at low fields is proportional to the magnitude of the field. This limit is set by the interaction of the electron with imperfections in the crystal through the scattering process.

It implies that scattering theory is important for electron transport in solids. The interaction of carriers in a solid with imperfections of the crystal lattice such as

impurities, lattice vibrations, and lattice defects, contribute to the scattering. Here we discuss about the general scattering theory and also give some brief description of the various scattering processes.

3.4   GENERAL SCATTERING THEORY

Some of the most important scattering sources that determine the transition of the electron are phonons, ionized impurities, interactions with other electrons and interface roughness scattering. The transitions of interest for electron transport in semiconductors are primarily classified as intervalley and intravalley. A scattering is considered to be an intervalley scattering event when the final state of the electron lies in a valley different from that of the initial valley and it is considered as intravalley scattering when the final state of the electron is in the same valley as the initial state.

The scatterings which fall under the intravalley scattering catergory are:

- Polar Optical Phonon

- Non-Polar Optical Phonon

- Deformation potential acoustic phonon

- Piezo-electric acoustic phonon

- Ionized impurity

- Neutral impurity

The various scattering mechanisms could be classified in a very broad manner and is depicted in the figure 3.3.

```
            ┌─────────┐
            │  Start  │
            └─────────┘
                 │
                 ▼
         ┌───────────────┐
         │  Initial Data │
         └───────────────┘
                 │
                 ▼
    ┌──────────────────────────┐
    │ Tabulation of Scattering │
    │          Rates           │
    └──────────────────────────┘
                 │
                 ▼
         ┌───────────────┐
    ┌───▶│  Free Flight  │
    │    └───────────────┘
    │            │
    │            ▼
    │    ┌───────────────┐
    │    │  Choice of    │
    │    │  Scattering   │
    │    └───────────────┘
    │            │
    │            ▼
    │    ┌───────────────┐
    │    │  Choice of new│
    │    │ electron State│
    │    └───────────────┘
    │            │
    │            ▼
    │    ┌───────────────┐
    │    │ Calculation of│
    │    │ parameters of │
    │    │   interest    │
    │    └───────────────┘
    │            │
    │            ▼
    │         ◇ Steady
  No│          State
    └─────────◇ Velocity
                 │ Yes
                 ▼
    ┌───────────────┐     ┌────────┐
    │ Calculation of│────▶│  Stop  │
    │   Averages    │     └────────┘
    └───────────────┘
```
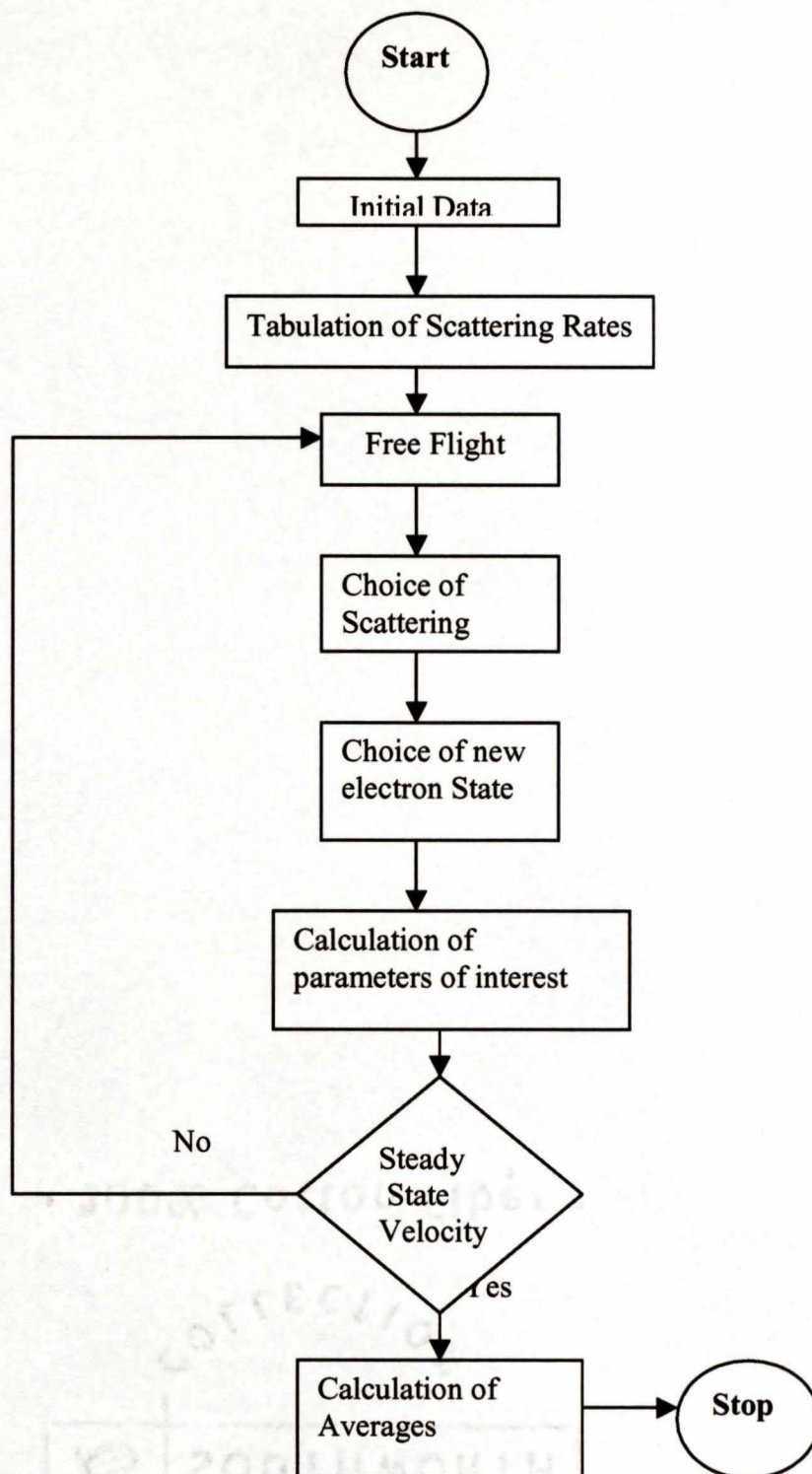
Fig 3.1 Flow chart of the ensemble Monte Carlo program.
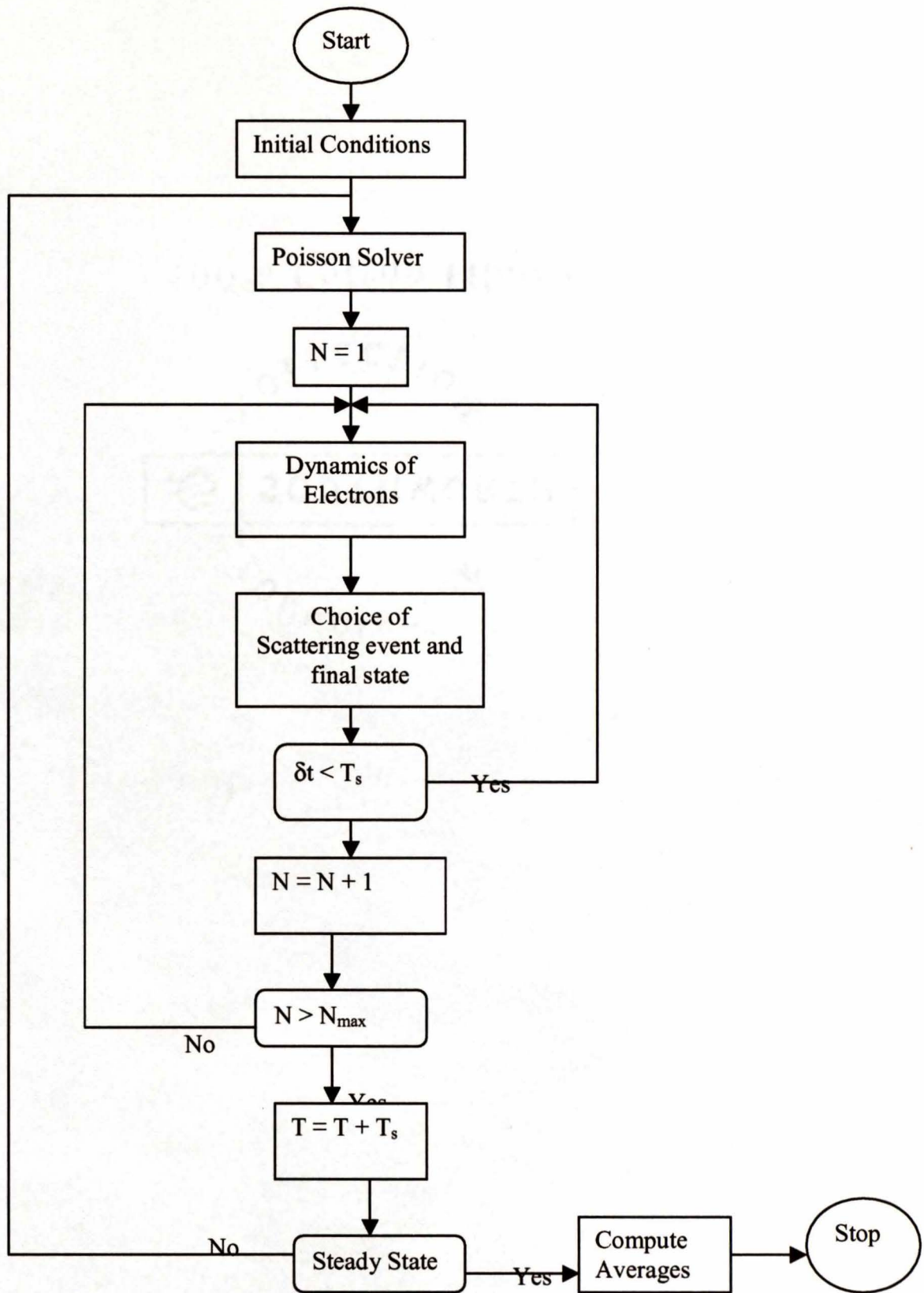
Fig 3.2 Flow – Chart of a device ensemble Monte Carlo program.
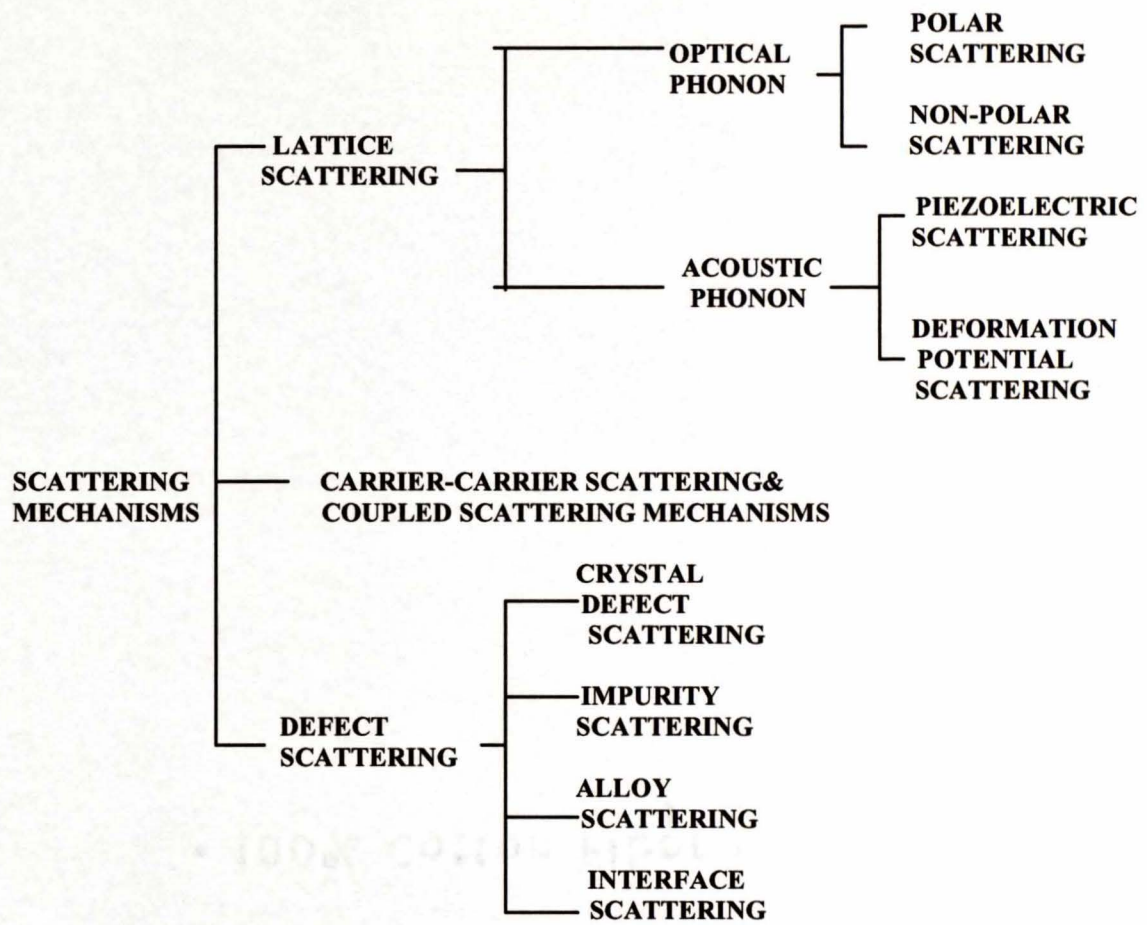
Fig. 3.3 Different scattering mechanisms.

3.4.1 ACOUSTIC PHONON SCATTERING

The energy change in acoustic phonon scattering is negligible and it is treated as an elastic process. But, a small-energy dissipation is needed to establish a smooth distribution function in the case of non-linear transport problems. The squared matrix element V(q) is given by [67]

$$V(q) = \frac{E_a^2 hq}{2\rho s} \left(N_q + 0.5 \pm 0.5 \right) \quad , \tag{3.20}$$

with the plus (minus) sign referring to phonon emission (absorption) process, E_a is the acoustic deformation potential, ρ is the crystal density, s is the speed of sound and N_q the Bose – Einstein distribution given by :

$$N_q = (\exp[h\omega/kt]-1)^{-1} \quad , \tag{3.21}$$

where $h\omega$ is the phonon energy. The acoustic phonon scattering rate can then be determined.

3.4.2 POLAR OPTICAL PHONON SCATTERING

The two oppositely charged unit cells oscillate out of phase in optical phonon mode of vibration. The displacement during the oscillation sets up a polarization field that scatters the electron. The squared matrix element for this scattering process is given by [67]

$$V(q) = \frac{4\Pi e^2}{4\Pi \varepsilon q^2} \frac{h\omega}{2} (\varepsilon_\infty^{-1} - \varepsilon_0^{-1})(N_q + 1/2 \pm 1/2) \quad , \tag{3.22}$$

where ε_∞ and ε_0 are the high frequency and static dielectric constants respectively. N_q is again the Bose–Einstein distribution for phonons.

3.4.3 NON-POLAR OPTICAL PHONON SCATTERING

The non-polar optical phonons generate a short range of potential that causes a shift in the electronic band states. One set of atoms moves as a body against the second set of atoms in the long wavelength optical mode of vibration which creates a strain in the lattice. This type of scattering of electrons by the strain is known as deformation potential scattering.

$$V(q) = \frac{D_o^2 h^2}{2\rho h \omega} (N_q + 1/2 \pm 1/2) \quad , \tag{3.23}$$

where D_o is the deformation optical potential.

3.4.4 INTERVALLEY PHONON SCATTERING

If there are multiple valleys in the conduction band, intervalley phonon scattering comes into play. In a multi –valley model electrons undergo transitions between states in two different equivalent or non-equivalent valleys after scattering with large momentum phonons. Considering two conduction band valleys involved in the transition, the phonon wavevector is approximately constant and is given by the distance in the Brillouin zone between the minima of the initial and the final valleys. The energy involved in such a transition is also approximately constant and intervalley scattering can be formally treated in the same way as the intravalley optical phonon scattering with the deformation potential interaction.

On the other hand, there is a large amount of momentum transfer in such a transition. The wavevector causing such transitions is nearly the same as the distance between the minima of the initial and final valley in the Brillouin zone.

$$V(q) = \frac{D_{ij}^2 h^2}{2\rho h\omega_{ij}} (N_q + 1/2 \pm 1/2) \quad , \qquad (3.24)$$

where D_{ij} is the deformation potential for scattering from i^{th} valley to the jth valley induced by a phonon energy of $h\omega$.

If the scattering between the central and satellite valley occurs, the electrons must acquire at least an energy Δ before the transition becomes possible. But on the other hand if the transition is from sattelite valley to the central valley, it is necessary to add Δ to the electron energy.

3.4.5 IONIZED IMPURITY SCATTERING:

The ionized impurity scattering is elastic in nature and it cannot control the transport by itself in the presence of external electric field. It should be accompanied by some dissipative scattering mechanism to obtain proper energy distribution. The scattering source is a direct result of coulombic interactions of the carriers and the ionized atoms. The squared matrix element in this scattering process is given by [68,69] :

$$V(q) = \frac{NZ^2e^4}{(4\Pi\varepsilon)^2(q^2+\beta^2)^2} \quad , \qquad (3.25)$$

where Z is the number of unit charges in the impurity, and β is a constant screening parameter.

3.5   POISSON'S EQUATION

The need to solve Poisson's equation arises because one requires the full knowledge of both the internal electric field and the device potential at every time instant. The spatial distribution of the mobile charges is not homogeneous within the device. This implies that the distribution of electric fields is not uniform. The changes in the carrier positions in turn, continuously modify the electric field distribution within the device. Therefore, a method should be adopted to update the electric field at intervals through a new solution of Poisson's Equation. Charge flows must be monitored in addition to calculating carrier dynamics in responsible to local fields at any time.

3.6   BOUNDARY CONDITIONS

The simulation of both transient and steady state phenomenon is of interest for the analysis and modeling of semiconductor devices. The device is such that the electrons are constrained inside the device space that represents an open system through which particles flow. This flow of charge is clearly controlled by and dependent on the boundary of the device and so appropriate boundary conditions must be chosen. The contacts of the device are Ohmic in nature with an abundant supply of free carriers. So if a particle crosses one of these boundaries, one should replace another particle through the other side to maintain current continuity. This is known as a periodic boundary condition.

Such periodic boundary conditions were implemented in the present Monte Carlo program.

3.7 IMPLEMENTATION OF THE ENSEMBLE MONTE CARLO TECHNIQUE

An initial distribution of position and momentum of the electrons inside the device is set up at the beginning, which defines the initial conditions. The electric field distribution at the beginning of the simulation is obtained by solving Poison's equation. This dictates the dynamics of all the electrons in the ensemble that are simulated in parallel for a chosen time step dt. During this time interval, scatter and drift occurs continuously, and possible interactions with the boundaries are monitored. The new charge distribution at the end of each and every time step is set up through the knowledge of free carrier positions. The internal electric field should also be updated at the end of each and every time step by solving Poisson's equation. This should be done until we reach the end of simulation. Care should be taken such that the time step chosen should be less than the dielectric relaxation time.

Poisson's equation is solved by the method of finite differences, as it is relatively easy to implement. Generally, Poisson's equation is to be solved in three dimensions, but due to the transverse symmetry inherent in the chosen device structure allows the reduction to a one-dimensional problem. The Poisson's Equation in one–dimension is :

$$\frac{\partial^2 V}{\partial x^2} = \frac{\rho}{\varepsilon} , \qquad (3.26)$$

where V is the potential, ρ the charge density, and ε is the dielectric constant.

This can be computed using the method of finite differences as mentioned earlier. In reality, to solve Poisson's equation, one needs to find the charge density at various nodes generated across the device and since the ionized donors are immobile, they present a uniform background of positive charge in the doped regions of the device. On the other hand, the electrons are initially distributed in accordance with the doping density, but subsequently the changes in position with time are due to Ensemble Monte Carlo dynamics. The electric field values obtained from Poisson's Equation are used for updating charge movement during the subsequent time steps. By repeatedly applying the above method, the electric field, the potential profile throughout the device as well as the electronic distribution can be obtained. Figure 3.4 below gives the electric field distribution in GaN obtained from our Monte Carlo simulations, as an example of the dynamic nature of the electric field profiles. Further details of the Monte Carlo simulation results are discussed in the following section.

3.7.1   THE VELOCITY – FIELD CURVE FOR WURTZITE GaN

So far the discussion has centered on Monte Carlo procedure and numerical implementation of Poisson's Equation and also the role of non-uniformities in setting up internal fields. In this section, the above theory will be tested and it's implementation analyzed by carrying out Monte Carlo simulations of electron transport in bulk GaN. The central goal of this exercise is to demonstrate the validity and accuracy of the present GaN simulation code.
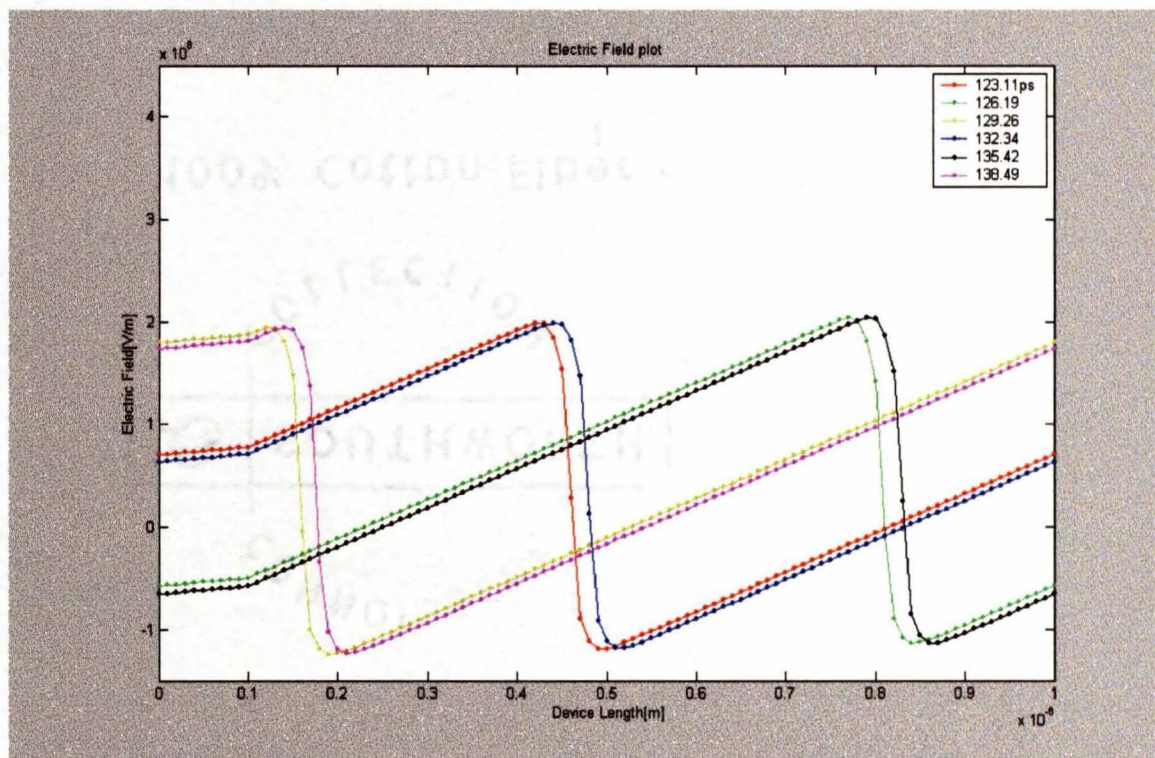
Fig. 3.4   Electric-field distribution along the device length.

The results for the field-dependent velocity response of electrons in GaN are presented first. The ambient temperature was chosen to be 300 K (i.e. room temperature). The plots of the transient velocity for different fields of 10^7 V/m, 1.7 x 10^7 V/m, 2.3 x 10^7 V/m and 3 x 10^7 V/m are shown in Fig. 3.5. The corresponding curves for the conduction valley populations are given in Figures 3.6. We can see that for higher fields there is a very fast rise in transient velocity. This is expected since the electrons are initially in the lowest valley ($\ni_1$) where the mobility is the highest. Under the influence of the electric field, these electrons gain energy and accelerate causing the velocity to increase quickly. Once they attain energies higher than the energy threshold, they undergo inter-valley scattering into the higher valleys, where their effective mass is larger. Hence, their mobility becomes less. As a result, their collective drift velocity decreases, and the ensemble attains a steady-state velocity. This final steady state velocity is determined by the material parameters and physically represents a dynamic equilibrium between the Γ_1 → L-M valley, and vice versa. The steady state velocities are lower at higher fields because a larger fraction of electrons occupy the higher mass valleys (i.e. the L-M, and Γ_3).

For low electric fields such as 10^7 V/m and 1.7 x 10^7 V/m, the drift velocity rises more slowly than at the higher fields. The steady state values are correspondingly high as most of the electrons will continue to be in the lower valley that has a higher mobility. To compare our results with the literature, we present in Fig. 3.7, the steady state Velocity – Electric Field curve obtained from the transient velocities of Fig. 3.5. The curve of Fig. 3.7 was obtained by focusing on the transient velocity plots, and plotting the steady state velocity corresponding to each transient velocity plot for that electric field.
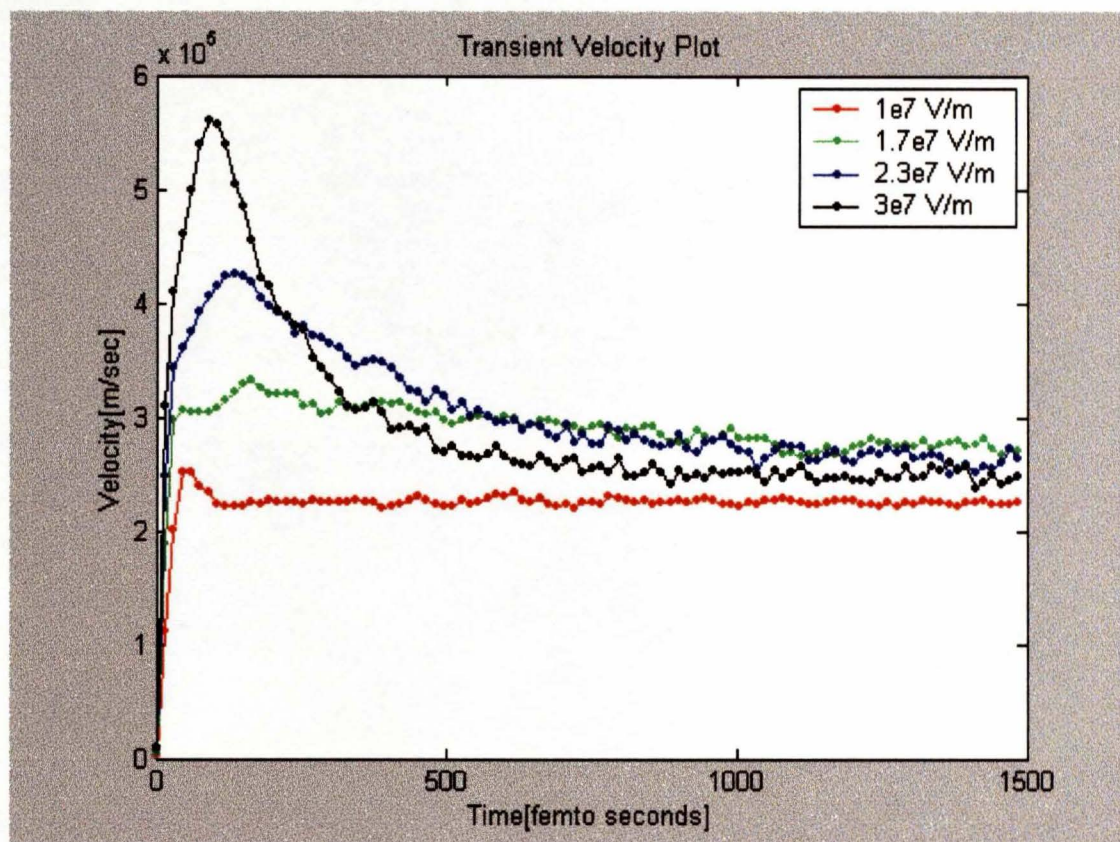
Fig. 3.5 Transient velocity plot for different fields.
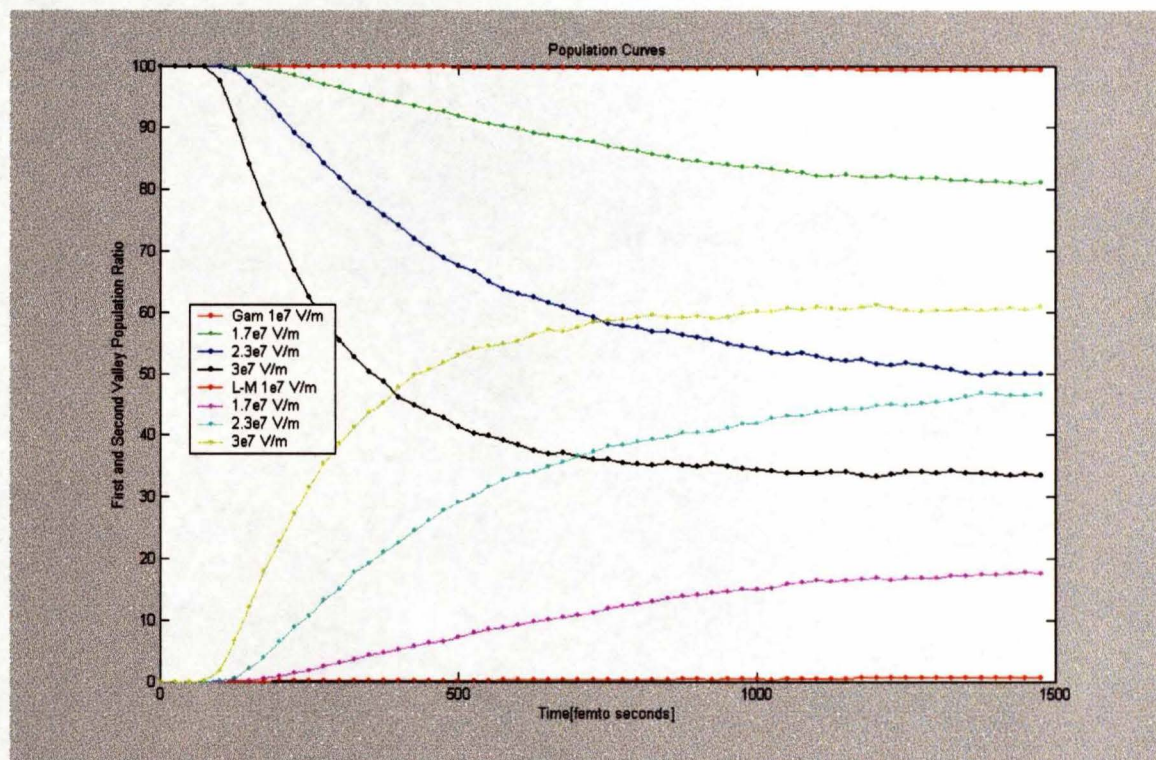
Fig. 3.6 First and second valley populations for various fields.
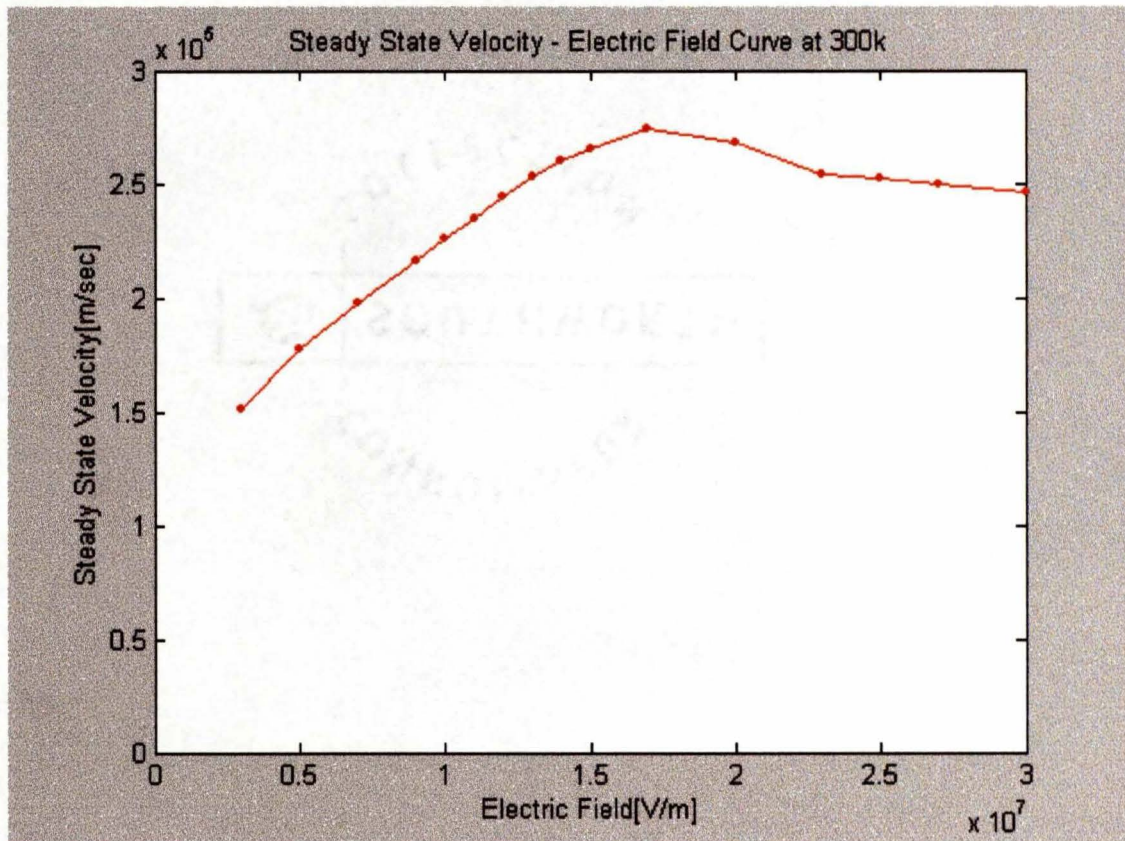
Fig. 3.7 Steady state velocity vs electric field plot at T = 300K.

This plot is given in Fig. 3.7. For comparison, the steady state velocity-field plot for

Wurtzite GaN material as previously reported by Kolnick et al. [42] in the literature is

shown in Fig. 3.8. The current result of Fig. 3.7 compares very well with that of Kolnick

et al. This agreement validates the present approach and numerical implementation of the

Monte Carlo scheme for bulk GaN material. The threshold field at 300K is predicted to

be around 180 kV/cm. This value and the overall velocity-field curve are in good

agreement with the report by Kolnick et al. [14]. A peak steady state drift velocity of

about 2.7×10^5 ms^{-1} is predicted for the 300 Kelvin case. A gradual decrease in the

steady-state drift velocity beyond 180 kV/cm is apparent, but the values remain well over

2×10^5 ms^{-1} even for electric fields as high as 300 kV/cm. This agreement establishes the

validity of the transport parameters used in the present model and underscores its utility

as a simple, computational efficient tool for analyzing transport for field below 300

kV/cm.
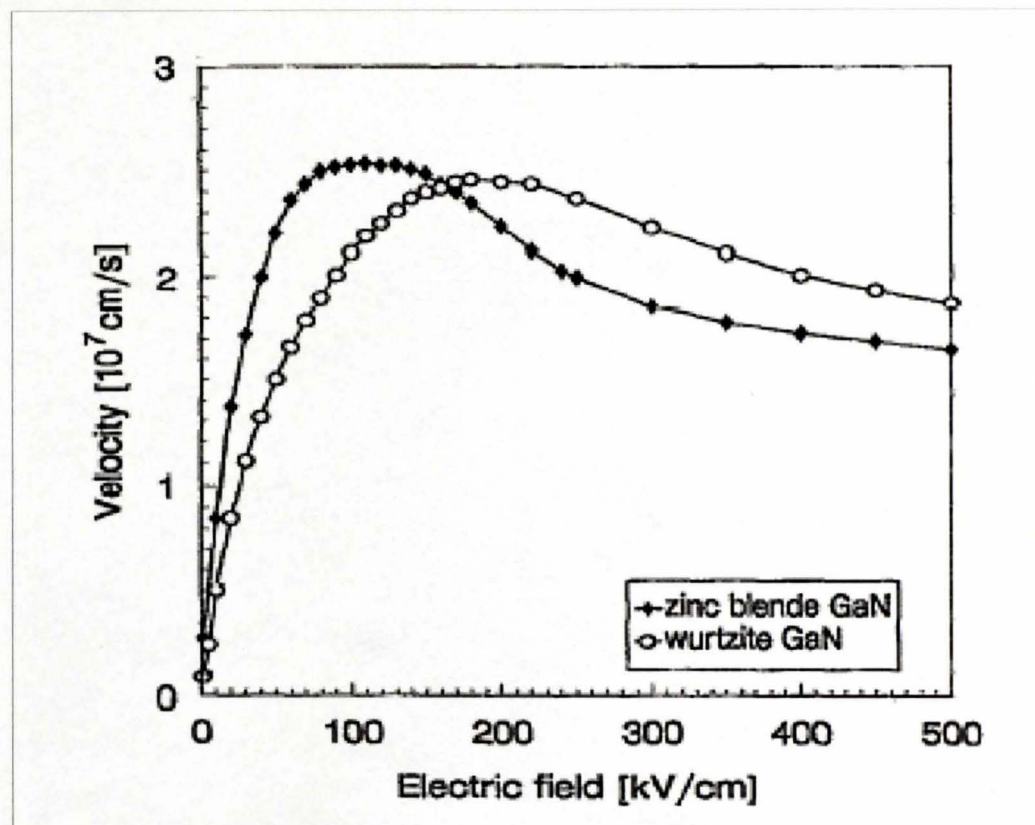
Fig. 3.8 Steady state velocity–field plot as calculated by Kolnick et al. [42].

Table 3.1   Parameters used in the Monte Carlo calculations for wurtzite GaN.

PARAMETER	VALUE
Lattice constants in meter (a , c)	3.189×10^{-10}, 5.185×10^{-10}
Dielectric constants $k(0)$, $k(4)$	9.5 , 5.35
Density (gm cm^{-3})	6.095
Acoustic velocity (ms^{-1})	4.33×10^5
Effective mass $m_{\parallel}$ $(T_1$, U- and T_3-valley)	0.1846, 0.3858 , 3.6227
Effective mass m_{ζ} $(T_1$, U- and T_3-valley)	0.2283, 3.03, 0.2856
Valley separation (eV)	0.0 , 2.2717 , 2.4
Nonparabolicity factors T_1 (eV^{-1})	0.37
Nonparabolicity factors U- valley (eV^{-1})	3.03 (m_{ζ}) and 0.385($m_{\parallel}$)
Nonparabolicity factors T_3 valley (eV^{-1})	0.22 (m_{ζ}) and 4.455($m_{\parallel}$)
Longitudinal optical phonon energy (eV)	0.092
Intervalley phonon energy (eV)	0.065
Acoustic deformation potential (eV)	8.0
Zero-order equivalent intervalley deformation potential (eV/cm)	0.5×10^9
Zero-order nonequivalent intervalley deformation potential (eV/cm)	1.0×10^9
First-order intervalley potential (eV)	5.0

CHAPTER IV

RESULTS AND DISCUSSION

4.1 INTRODUCTION

The present work presents an exact large-signal simulation of millimeter-wave Gunn effect oscillators made of bulk wurtzite GaN semiconductor material. This simulation properly accounts for all significant electron relaxation/collision phenomena by utilizing the Monte Carlo technique of Fawcett, Boardman and Swain [70]. The device modeled has a "contemporary" design with heavily doped contacts. The contact doping is used in the evaluation of the electric field at the boundaries. This, in effect, circumvents having to approximate the terminal electric field at a zero value. The Gunn diode, when interacted with the external circuit, is shown to oscillate in the fundamental mode at 140 GHz for a device length of 1μm. The interpretation of the device behavior which for the first time is based upon the latest knowledge of electron physics, includes familiar phenomena: electrons are seen to "overshoot" traditional peak velocities, and a "dead zone" at the cathode found where electrons never gain sufficient energy to transit to satellite valleys. The following sections present an outline of the Gunn diode device model and the method used for the Monte Carlo calculation. Two structures have been examined here: (1) devices with the conventional single notch structure, and (2) repetitive structures with serial segments to fashion a "multiple domain" device.

4.2   THE GUNN DIODE DEVICE MODEL

The description of the device for the conventional Gunn diode structure is presented. The multi-domain Gunn diode structure is almost similar, since it is in essence nothing other than a serial array of ordinary Gunn diodes that can be fabricated by Molecular Beam Epitaxy. Such devices would have larger impedance than the conventional Gunn diodes, leading to an increase in the output power [71].

For the simulation of the conventional Gunn diode, a 20-percent notch in doping near the cathode was included to provide an initial high electric field region so that the dead zone can be considerably reduced. The "dead zone" is typically the region that does not contribute to any output power, since the injected thermal electrons are getting accelerated up to the inter-valley transfer threshold energy. The device was divided into 100 spatial cells and the size of each cell is 10^{-6} cm, which meets the numerical convergence requirements of Thim [72]. The total number of electrons chosen in this Monte Carlo Simulation is 9000. This implies that each Monte Carlo electron represents to 1.1×10^{6} real electrons in the actual device. The size of the computer memory as well as the execution time of the simulation are taken into consideration for choosing the number of electrons for the simulation.

The electric field each electron was subjected to, was calculated by first calculating the internal instantaneous electric field of each cell according to

$$E(n,t) = E(n-1,t) - [\ MI(N) - MM(N,t)].q.\ \Delta x/\ \varepsilon \qquad , \qquad (4.1)$$

where N is the cell number, $MI(N)$ is the number of ions in each cell representing the real doping density, $MM(N,t)$ is the number of electrons in each cell, q is the electronic

charge, Δx is the cell size, and ε is the dielectric constant. The cathode electric field $E(0,t)$ then was adjusted to satisfy the boundary condition:

$$V(t) = \Sigma \, [E(n,t)- E(n-1,t). \, \Delta x/2] \qquad , \qquad (4.2)$$

where $V(t)$ is the instantaneous terminal voltage defined below, and L is the number of cells. The electric field at each cell boundary was then recalculated according to Eq. (4.1). The electric field each electron was subjected to was calculated as the mean of the electric fields at the boundaries of the simulation cell containing that electron.

Each electron was allowed to drift and undergo collisions for two femto-seconds. After this, the external circuit interaction was determined, and voltages were updated at the device boundaries to yield a new electric field. Electrons that crossed the anode and cathode boundaries during flight were replaced, to satisfy charge neutrality at the cathode or anode, respectively, by electrons randomly chosen from a room temperature Boltzmann distribution. The instantaneous electron current flowing through the device is given by the equation:

$$I_d(t) \; = \; qS/L* \sum_{i=1}^{N} V_i(t) \qquad , \qquad (4.3)$$

where S is a scale factor relating to the number of real electrons per cell to the number of Monte Carlo electrons. N is the total number of Monte Carlo electrons, $V_i(t)$ is the velocity of the ith electron at a given time "t" and L is the length of the device. This

electron current is used for the calculations presented later for the device circuit interaction.

4.3   SIMULATION AND DEVICE EQUATIONS

For a more realistic simulation of the microwave oscillator, the GaN device was embedded in a parallel resonant circuit shown in Fig 4.1. This allows for the circuit effects, permits performance evaluation at the fundamental frequency and other harmonics, and enables the assessment of circuit paramenter variations. The parallel resonant circuit is essentially a dielectric capacitance C_D and an external capicatance C_L in parallel with a load resistance, and the equivalent combination is in series with an inductance L. This circuit is an L-C-R cavity with resistance R = 20 ohm, capcaitance C = 0.05 pico Farads and inductor L = 0.12 nano-Henrys. The battery voltage is applied in series with the inductance. The external capacitance is such that it is 3 times the device capacitance to obtain a reasonable operating frequency.

The interaction of the circuit and device was formulated as a pair of finite difference equations. The time dependent current $I_t(x,t)$ in the device is given by

$$I_t(x,t) = I_e(x,t) + \varepsilon A \left[\partial E(x,t)/\partial t \right] \qquad , \qquad (4.4)$$

where $I_e(x,t)$ represents the particle current and $\varepsilon A \partial E(x,t)/\partial t$ is the displacement current. A is the cross-sectional area of the device, and ε is the dielectric constant. Since the total
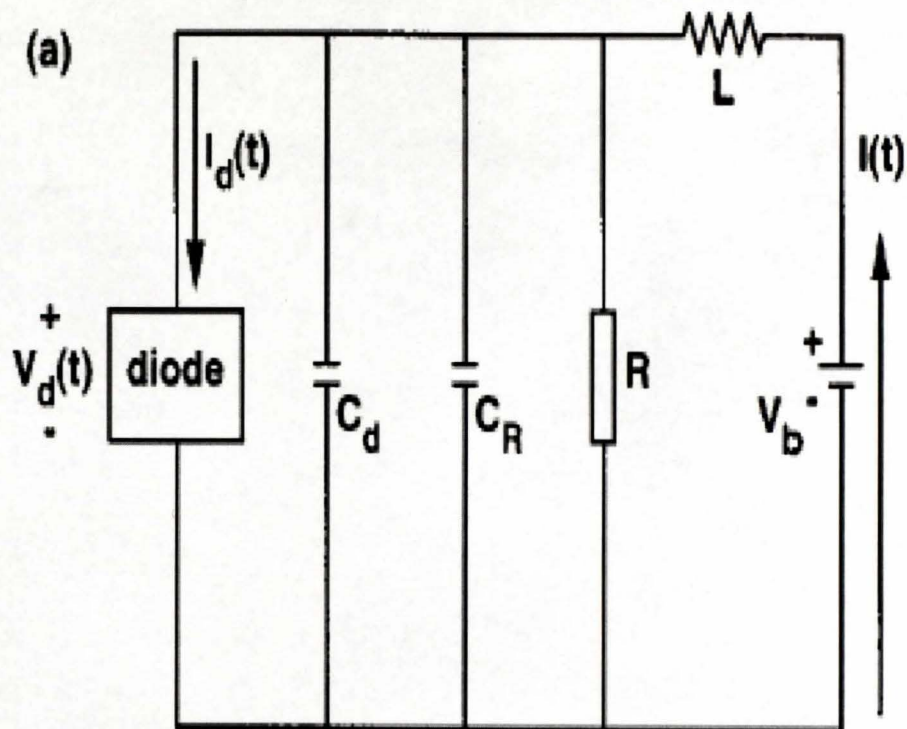
Fig. 4.1(a) Schematic diagram of the parallel resonant RLC circuit used for the simulation of a Gunn diode oscillator.
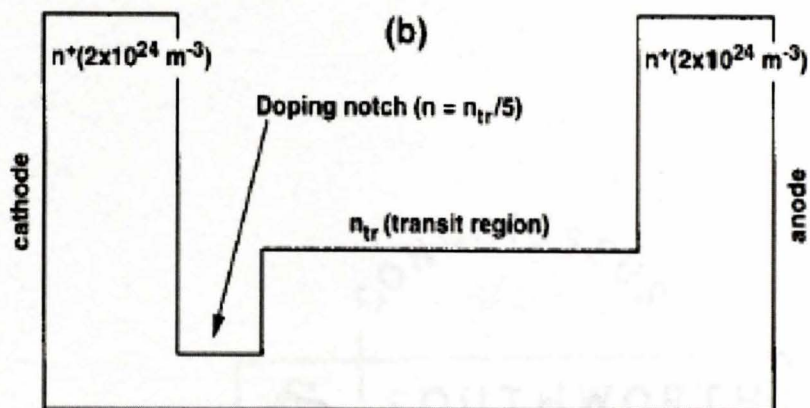
Fig. 4.2(b) Doping profile of the conventional GaN notch diode.

current is constant throughout the device at any given time, the above equation can be integrated over the device length W to yield :

$$I_t(t) = (1/W) * \int_0^W I_e(x,t) + (\varepsilon A/W) * \partial V/\partial t = I_d(t) + C_{cold} \, \partial V/\partial t \qquad , \qquad (4.5)$$

where V is the instantaneous potential across the device. The quantity $\varepsilon A/W$ in the above equation is generally referred to as cold capacitance [73].

The total current and the device voltage were obtained by solving related Kirchhoff's equations:

$$V_D(t) = V_B - L*dI(t)/dt \qquad , \qquad (4.6)$$

$$and, \quad I(t) = I_d(t) + C* \, dV_D(t)/dt \, + \, V_D(t)/R \quad , \qquad (4.7)$$

where $V_D(t)$ is the instantaneous voltage applied to the device terminals, V_B is the dc bias voltage, $I(t)$ is the instantaneous current flowing through the battery, and C is the total capacitance (effective capacitance of the circuit and cold capacitance together). The above equations were discretized using finite differences in time, and can be rewritten as:

$$I(t + \Delta t) = [V_B - V_D(t)]*(\Delta t/L) + I(t) \qquad , \qquad (4.8)$$

$$and, \quad V_D(t + \Delta t) = [\, I(t) - \, I_d(t) \,]*(\Delta t/C \,) + V_D(t)[1 - (\, \Delta t/RC) \,] \qquad . \qquad (4.9)$$

From the above equations, forward voltages and currents were determined from the previous voltages and currents. In this simulation, either a set of initial guesses or old values of V(t), I(t), and $I_e(t)$ were used to initiate the iteration. The initial states of the Monte Carlo electrons were either those of the previous calculation, or states chosen at random from a room temperature Maxwellian distribution. The instantaneous voltage calculated above is the instantaneous terminal voltage of the device, based on which the internal electric fields were determined. The Monte Carlo procedure was executed for each simulation electron. Those Monte Carlo electrons that crossed anode and cathode boundaries in this process were then used to for calculation of the electronic current based on Eq. (4.8) above. The iteration was continued with calculations of new voltages and currents. Convergence was generally observed within 5 or 6 radio-frequency cycles.

A three-valley non-parabolic model was used to simulate the electronic motion based on the effective mass approximation. All the relevant scattering mechanisms such as polar, optical, acoustic deformation potential, equivalent- and nonequivalent inter-valley phonon, and ionized impurity scattering were comprehensively included. The Poisson solver was used at the end of each time step to update the internal electric field in response to electronic motion. A three-point, centered-difference scheme was used to discretize Poisson's equation. Finally, two device structures were chosen for the current simulation purposes: (1) devices with the conventional single notch structure, and (2) repetitive structures with serial segments to fashion a "multiple domain" device. Despite the potential, there have not been much studies going on in this subject. The only reports appear to be by Alekseev and Pavlidis [74] for wurtzite GaN based on transient hydrodynamic simulations.

Wurtzite material has been chosen because of the higher drift velocity and because analytical expressions for the band-structure have recently become available. A 65 meV phonon was assumed to adequately represent deformation potential scattering, and a 92 meV phonon value was used for the polar optical process. Apart from these, ionized impurity based on the Brooks-Herring approach and intervalley deformation potential processes were also considered. The piezoelectric scattering was neglected, because it has been shown that its effect is negligible at temperatures of 300K and above. Non-equivalent inter-valley scattering events were taken into account among all three valley types, governed by a single deformation potential and phonon energy. The electron mobility in different valleys is calculated from the diffusivity rather than from the drift velocity. This approach makes it possible to calculate the mobility at zero applied field, and also exhibits a lower statistical variation than the mobility determinations from the drift velocity [75].

A full Monte Carlo treatment of the time-dependent transferred electron problem is more accurate and desirable than the hydrodynamic scheme. The literature shows that steady-state velocity-field characteristics are obtained for the older band structure data. For example, previous results [76] were based on Γ_1-Γ_2 and M-L inter-valley separations of 1.9 and 2.1 eV, respectively. More recent calculations suggest a Γ_1, M-L, Γ_3, L_1, A_1 ordering. In the present work, we carry out the simulation using only the first 3 valleys of the above ordering. The details of the band-structure are as follows. The effective masses have been calculated to be 0.2283 and 0.1846 along the perpendicular and parallel directions, respectively, with a non-parabolicity coefficient of about $0.37eV^{-1}$. The satellite valleys are at the U point that is two-thirds of the way between the L- and M-

symmetry points, with an energy separation of 2.2717 eV. According to the calculations by Goano et al. [42], the next highest valley is located at the Γ_3 point, 2.4 eV above Γ_1. Finally the valleys at the L_1 and A_1 are located at 2.5 and 2.6 eV respectively above Γ_1. The effective masses for the M-L minima are anisotropic. The mass is 3.0375(along Γ-A_1), 0.3158 (along K-H), and 0.3858 (along the M and L points). The corresponding non-parabolicity coefficients also depend on the direction, and are reported to be : -1.0325 eV^{-1} (along Γ- A_1), 0.2164 eV^{-1} (along K-H), -0.174 eV^{-1} (along M) and 0.9686 eV^{-1} (along L). Such anisotropic features were included in the present simulation. For the Γ_3 valley, the effective masses along the parallel and perpendicular directions were taken to be 3.6227 and 0.2856, respectively. The non-parabolicity factors are given to be 4.4554 parallel to the c-axis and 0.22 along the perpendicular directions.

In our simulations, the device structure was taken to have a cross-sectional area of 10^{-9} m^{-2}. The doping profile for the conventional single transit notch structure is shown in Fig 4.2. The two heavily doped end regions with densities of 2 x 10^{24} m^{-3} serve as the n$^+$ contacts. The transit region has the doping level in the range of 5 x 10^{22} m^{-3} – 2 x 10^{23} m^{-3} range. This doping level looks very large compared to the typical value of the doping level chosen for GaAs and InP Gunn devices. This is because of the lower mobility of GaN, when compared with the mobility of either GaAs or InP, and thus the time required to build up a stable domain is higher for the same background doping. The higher doping chosen here helps offset the lower mobility. The notch at the cathode end is required to create the local non-uniformity that helps launch the accumulation or dipole-domain mode instabilities. The equilibrium density of the notch was set at 20 percent of the

transit region. The dead-zone lies in this region. The simulation should also be run for the device having multiple segments as shown in Fig 4.3.

4.4   DISCUSSION OF THE RESULTS

The results are divided into two parts. First, results of the Monte Carlo simulation for bulk wurtzite GaN at different temperatures are given and the results are compared with the previous results with discussion. Secondly, having demonstrated the Monte Carlo model, simulations were carried out for the GaN based Gunn structure for different lengths of the n region around 1.0 μm at different temperatures. These simulations are for two different device structures which are: (1) devices with conventional single notch structure, and (2) repetitive structures with serial segments to fashion a "multiple domain" device.

Results of the Monte Carlo simulation for bulk Wurtzite GaN at 300K are given and discussed first. The primary objective of this simulation is to compare the results against more sophisticated calculations that have included a full band structure. A 9000 electron Monte Carlo code was used with a 0.5 femto-second time step. The transient velocity-versus-time graphs are shown in Figs. 4.4, 4.5 and 4.6 for different electric fields at three different temperatures. From the graphs, it can be seen that there is an overshoot initially and the velocities finally settle down. For small electric fields, there will be no much overshoot. This simulation is run until the velocity becomes steady with time and from these results, the steady state drift velocities at different electric fields are determined. There has been an upper limit on the electric field of 300 kV/cm to prevent the electronic energies to become very large. This precaution was necessary as the
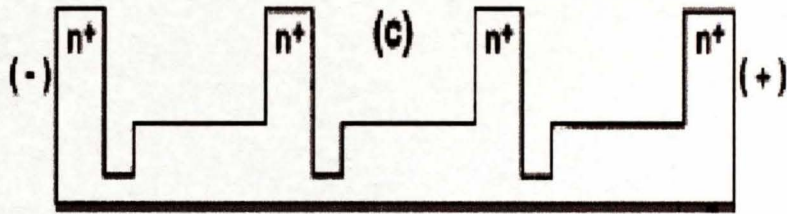
Fig. 4.3(c) Doping profile of a three transit region multiple GaN Gunn diode.
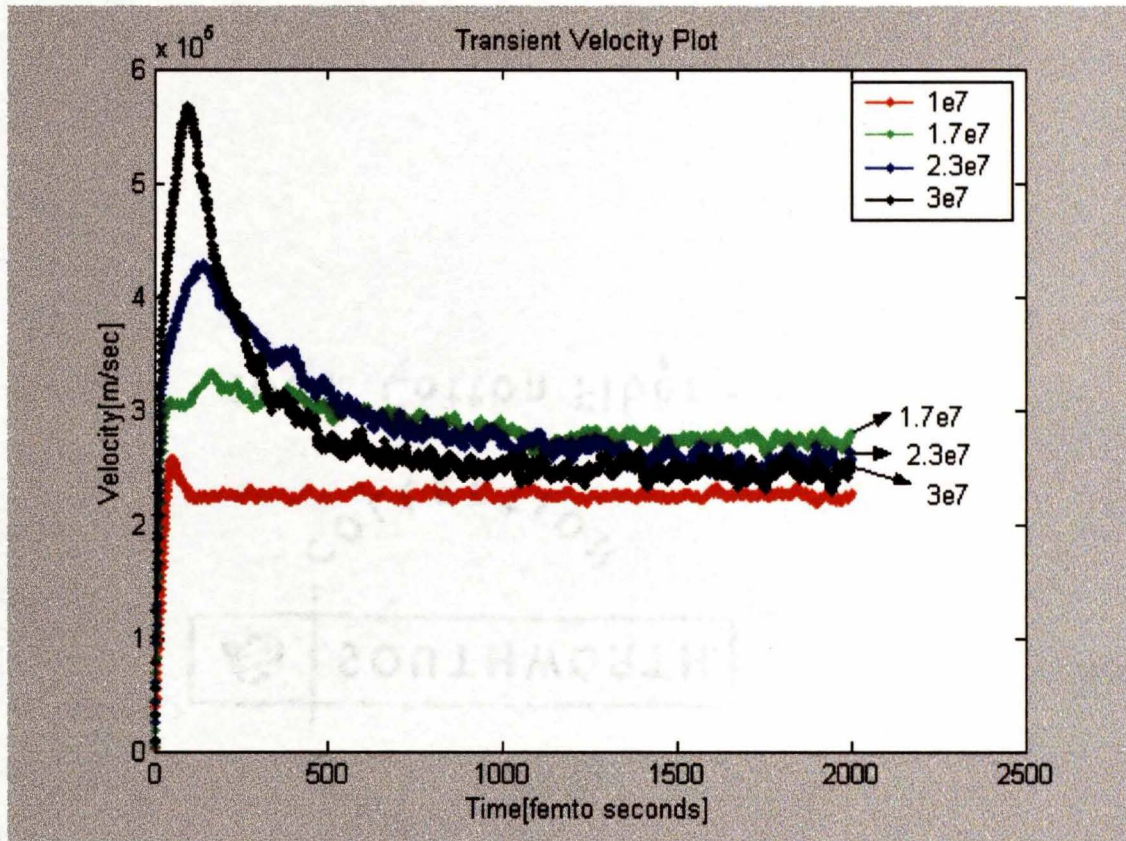
Fig. 4.4 Monte Carlo results of the transient electron drift velocity at 300K in wurtzite GaN for different electric fields.
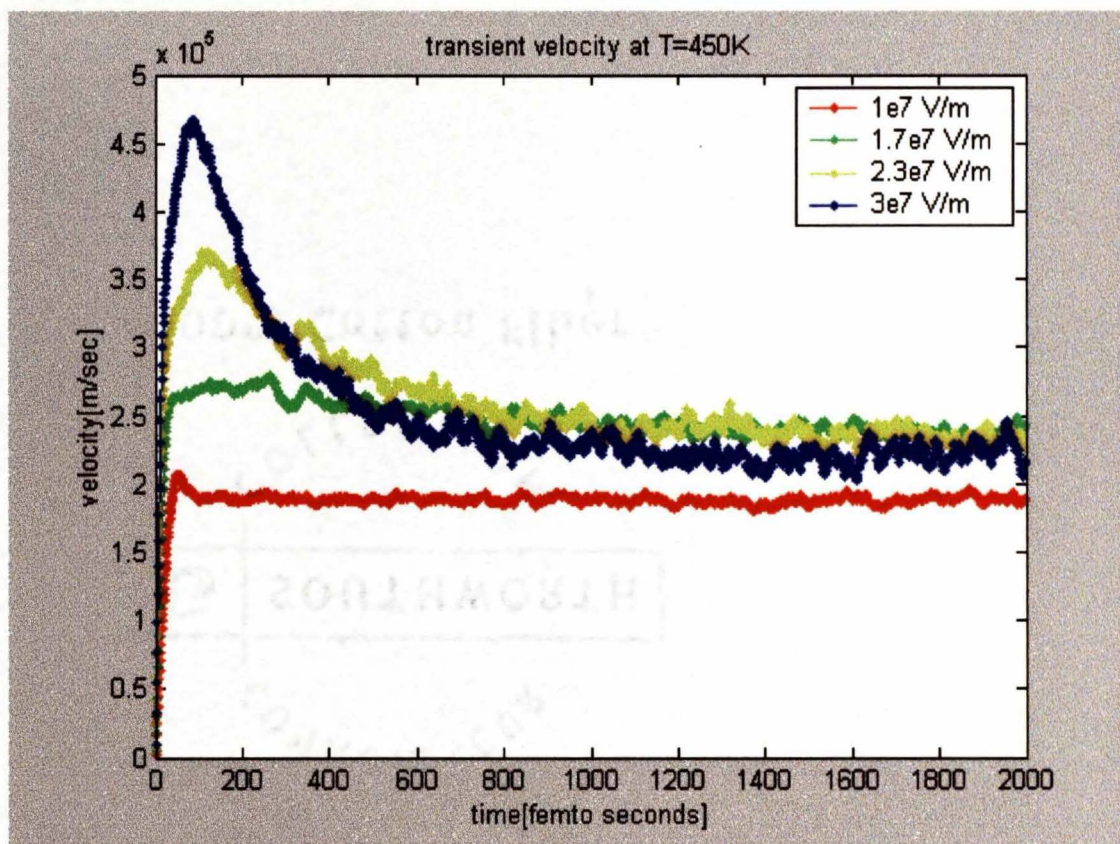
Fig. 4.5 Monte Carlo results of the transient electron drift velocity at 450K in wurtzite GaN for different electric fields.
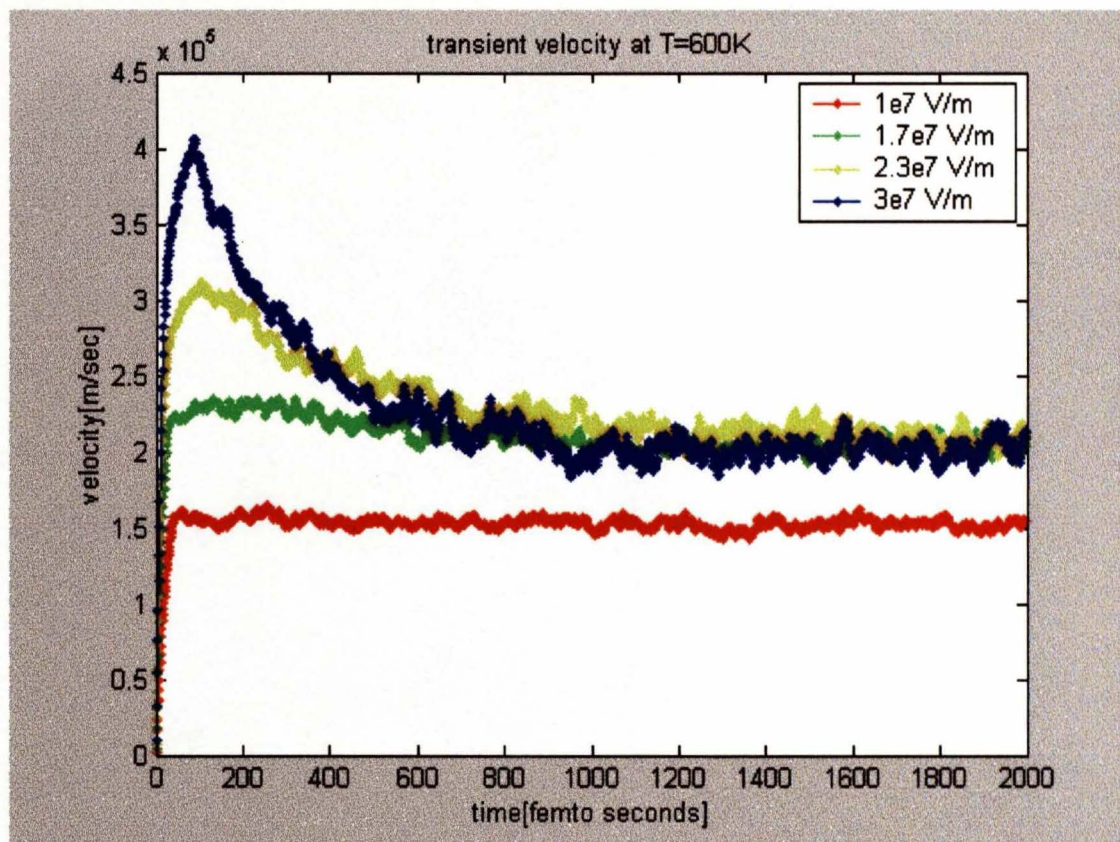
Fig. 4.6 Monte Carlo results of the transient electron drift velocity at 600K in wurtzite GaN for different electric fields.

present simulation does not include a full band structure, but instead relies on a simple non-parabolic approach to the energy bands.

The steady state drift velocity of the electronic ensemble in bulk GaN at 300K for different values of the electric fields is given in Fig 4.7. This result facilitates a direct comparison with previous reports that took account of a full band-structure calculation by Kolnik et al. [42]. The maximum steady state drift velocity is found to be 2.742 x 10^5 m/sec at an electric field of 170 kV/cm. This compares well with the value of 2.5 x 10^5 m/sec at a field of 180 kV/cm obtained by Kolnik et al. [42]. The value and the overall velocity field curve are hence in good agreement with the previous reports. A gradual decrease in the steady state drift velocity beyond 170 kV/cm is apparent, but the values remain well over 2 x 10^5 m/sec even for electric fields as high as 300 kV/cm.

The simulation is also carried out for different temperatures. The steady state drift velocity – field curves for 450 K and 600 K are given in Fig 4.8 and they are compared with the curve for 300K. A peak velocity of 2.387 x 10^5 m/sec at 200 kV/cm for 450 K and a peak velocity of 2.127 x 10^5 m/sec at 200 kV/cm for 600K are predicted. These values are far larger than that for GaAs at room temperature and it clearly shows the future prospects of using GaN for high temperature operations. It can be seen that the velocities reduce as the temperature increases because of the stronger electron-phonon scattering. Another important parameter that can be obtained by the Monte Carlo simulation, is the percentage of electrons occupying each band (i.e. the band occupancy). The occupancy of the lowest Γ valley and L-M valley as a function of time for three different electric fields at three different temperatures are predicted. These can be seen in Figs 4.9, 4.10 and 4.11. Considering 300K case, fractional occupancies of 80% and
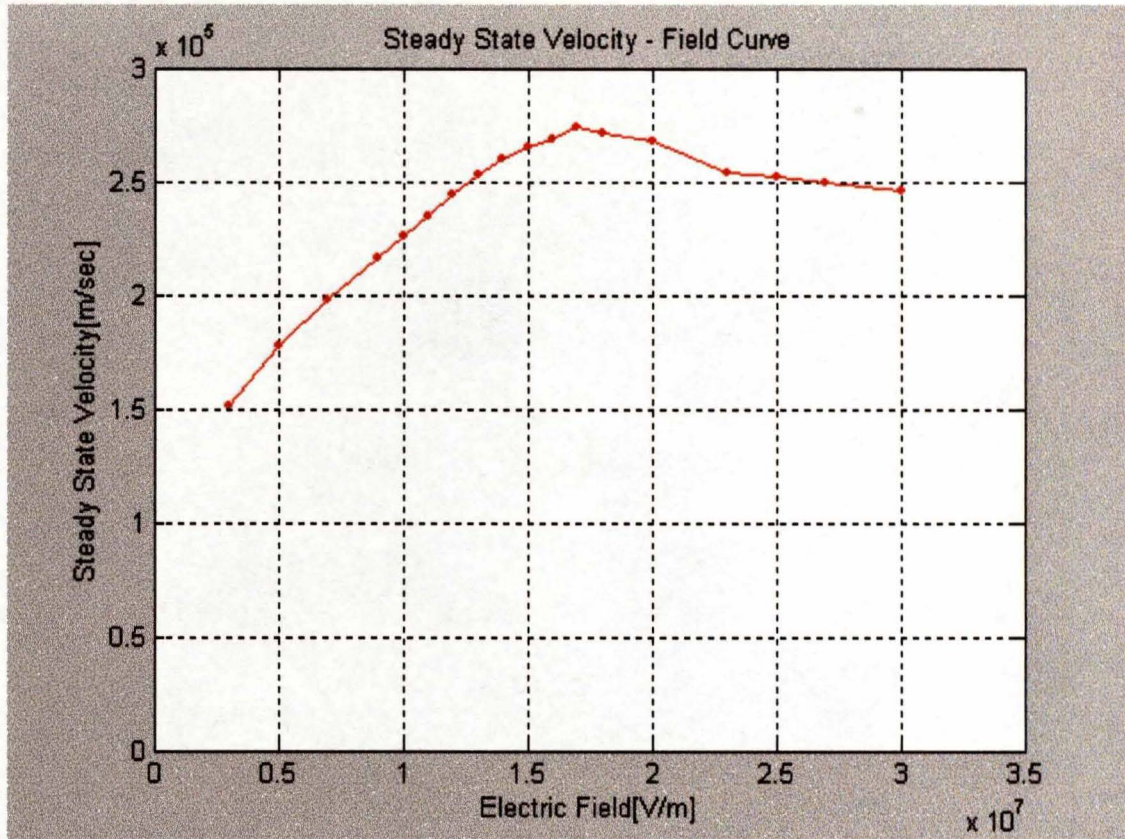
Fig. 4.7 Monte Carlo results of the steady-state velocity-field characteristics for electrons at 300K.
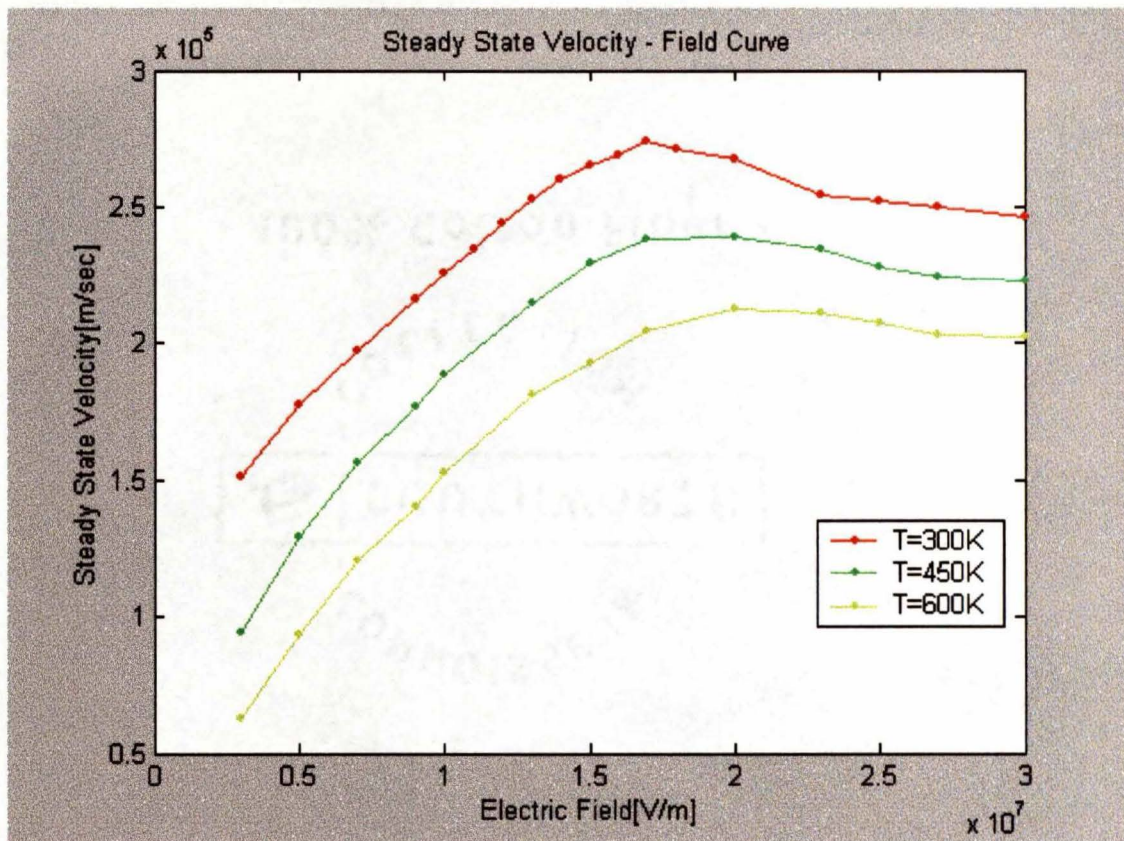
Fig. 4.8 Monte Carlo results of the steady-state velocity-field characteristics for electrons at T = 300K , 450K and 600K.
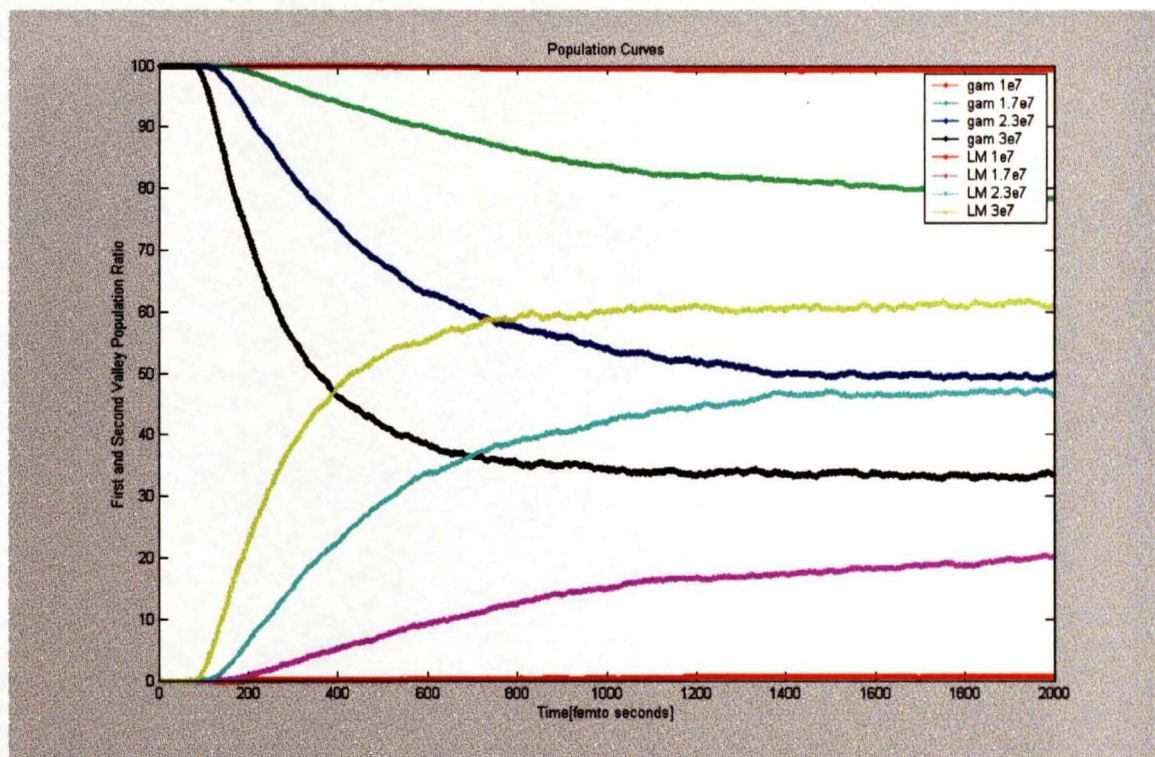
Fig. 4.9 Monte Carlo results of the Γ_1 valley and L-M valley electron populations at

T = 300K for different electric-fields.
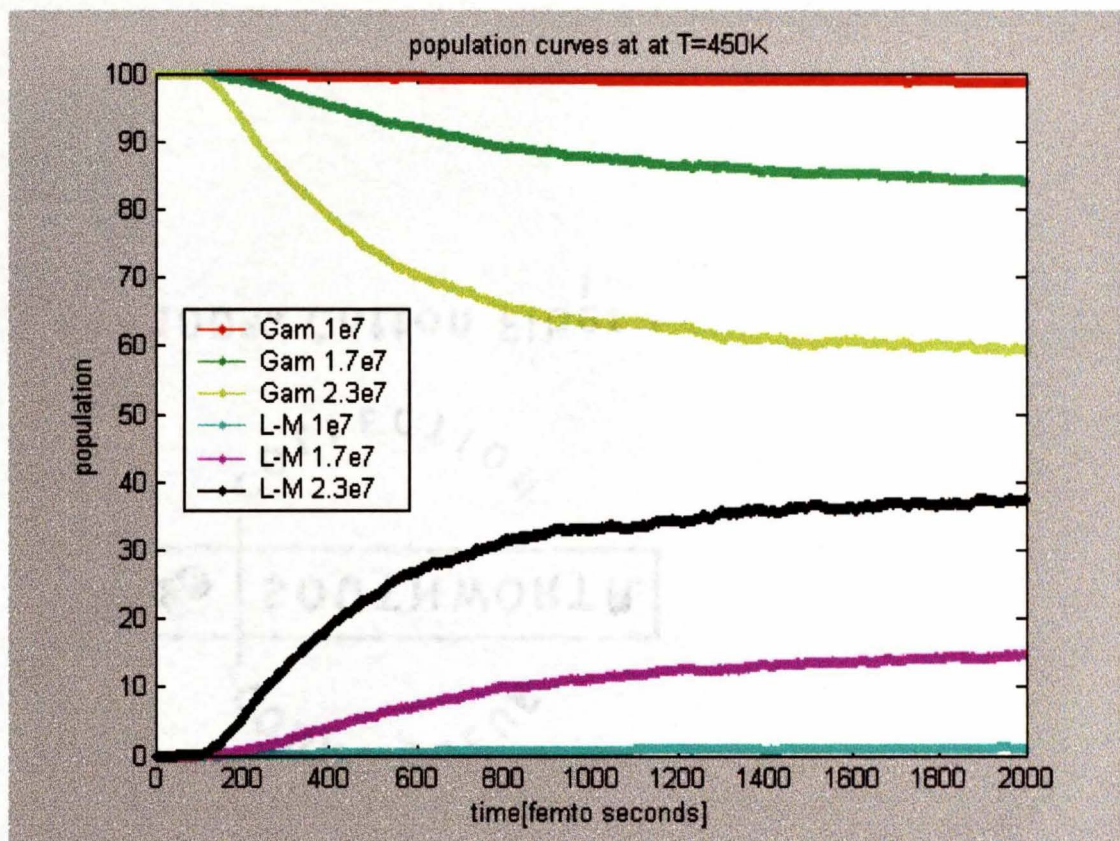
Fig. 4.10 Monte Carlo results of the Γ_1 valley and L-M valley electron populations at T = 450K for different electric-fields.
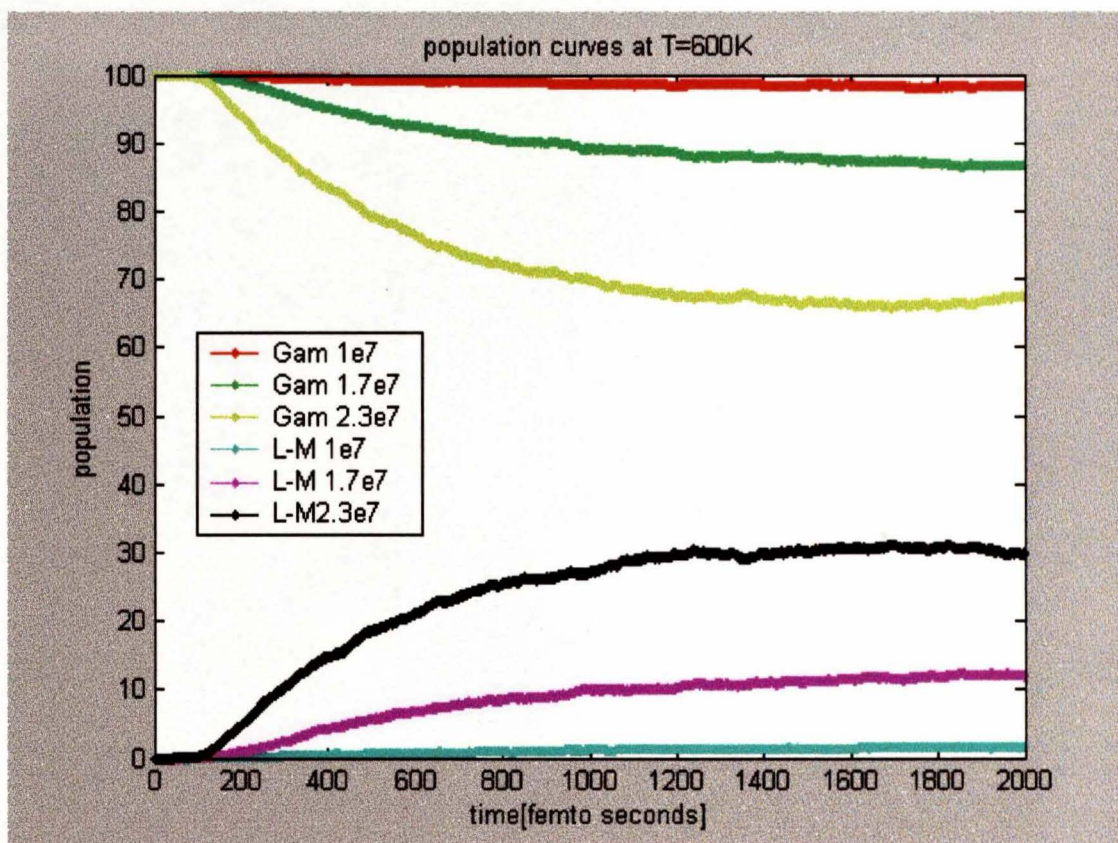
Fig. 4.11 Monte Carlo results of the Γ_1 valley and L-M valley electron populations at

T = 600K for different electric-fields.

higher are predicted for applied electric fields below 170 kV/cm for lowest Γ valley. There is a relative sharp transition into the satellite valleys for fields around 190 kV/cm. Steady state Γ_1 valley occupancies as low as 32% are predicted at our highest field at 300 kV/cm.

At field strengths greater than the threshold field, the electrons significantly populate the satellite valleys where new inter-valley deformation scattering mechanisms become effective. These results are also very close to those obtained by Kolnik et al. on the basis of a more sophisticated Monte Carlo scheme that included a full band structure. This agreement establishes the validity of the transport parameters used in the present model and underscores its utility as a simple, computational efficient tool for analyzing transport for fields below 300 kV/cm. Similarly for 600K, the fractional occupancies of 88% are higher are predicted for applied electric fields below 170 kV/cm for Γ_1 valley and fractional occupancies of 84% or higher for 450K. The electron phonon scattering is stronger at higher temperatures, which leads to lower electron drift velocity, and the average energy is not enough for the electrons transfer into the high energy, low mobility satellite valleys.

Simulations were next carried out for the GaN based n^+-n^--n-n^+ notch structure for lengths of the n region (active region) around 1.0 μm at 300K. The much smaller length compared to the 3.0 μm device simulations reported previously serves the following two purposes: (1) Enhanced operating frequency due to lower transit times, and (2) it ensures a higher sinusoidal component at the fundamental mode. Longer devices that operate in dipole domain mode tend to have a flatter response, with a higher non-sinusoidal component since variations in terminal current only take place at the start of

every domain formation cycle. The n-doping chosen here in the active region leads to "nL" product above the $5 \times 10^{16}\,\text{m}^{-2}$ threshold for GaN Gunn oscillations compared to $0.1 \times 10^{15}\,\text{m}^{-2}$ for GaAs. This means that for the same length of the active device, the device should be highly doped for GaN compared to GaAs. Higher doping of the active layers in the GaN NDR diodes also leads to reduction of the differential dielectric relaxation time and as a result it enhances growth rate of Gunn domains. Thus, the differential dielectric relaxation frequency of GaN Gunn diodes exceeds the frequency of GaAs. The electron distribution at the start is taken similarly to the doping density distribution of the device. This Gunn structure was taken to connect with the tank (RLC) circuit at $t = 0^{+}$.

Monte Carlo results at various temperatures for different active lengths at different applied bias voltages are calculated. The results at 300K for the single transit Gunn diode showing the time dependent behavior of the total current and the device voltage are shown in 4.12 and Fig 4.13. The device length was taken to be $1\mu m$ and the results are run for three different bias voltages. The result for an applied bias of 50V is explained first. The initial transient is simply associated with the commencement of the applied dc bias at time $t = 0$. A steady oscillatory state is reached in 50 pico-seconds, with the operating frequency predicted to be 140 GHz. The time required for the domain to travel from the cathode to anode is, the length of the active device divided by the average ensemble electron velocity. The corresponding frequency for the transit time domain mode is nothing but the inverse of the transit time. But a Gunn diode in a resonant circuit can operate at frequencies higher than the transit time frequency if the high-field domain can be quenched before it reaches the anode. Results for the simulated frequency dependencies of the generated power and device efficiency were then obtained by
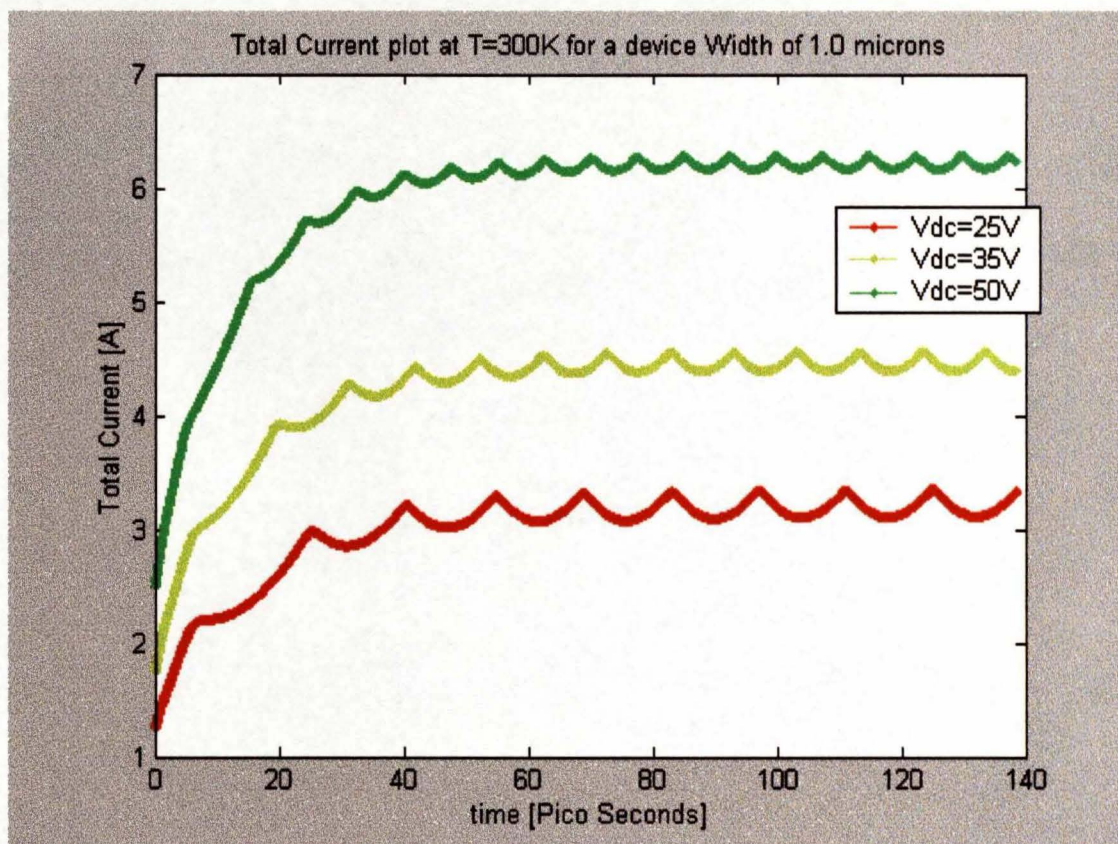
Fig. 4.12 Monte Carlo results showing the temporal development of the total current for a 1µm device at T = 300K for various biasing voltages.
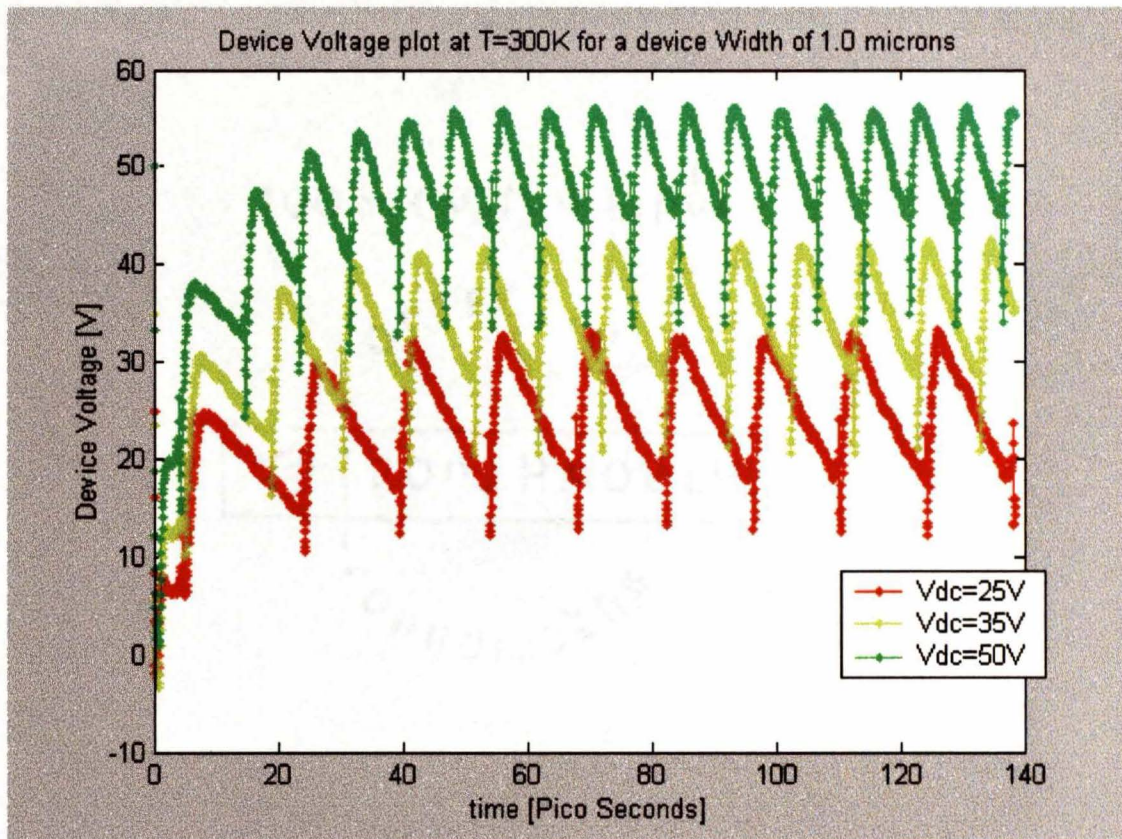
Fig. 4.13 Monte Carlo results showing the temporal development of the device voltage for a 1μm device at T = 300K for various biasing voltages.

running such time dependent simulations for different active lengths, device voltages and operating temperatures. The results for applied biases of 25 V and 35 V are shown in the same Figs 4.12 and 4.13. For a low applied bias of 35 V, the transit time taken by a domain to move from cathode to anode is low and it is still low for an applied bias of 25 V. The simulation cannot be run for voltages below 20 V, as the critical voltage for the oscillations to occur is 20 V for GaN diode for an active length around 1.0 μm at T = 300K. Then the simulation is carried out for a different device length of 0.8 μm and the results are shown in Figs 4.14 and 4.15. The applied bias voltage applied is 50 V. It is obvious that the transit time taken for a domain to move from cathode to anode is less, as compared to the 1.0 μm device since the traversal distance for the electrons is now less. It is predicted that the operating frequency of the Gunn diode is around 240 GHz. Similarly for an active device length of 1.2 μm and at an applied bias of 50 V, the operating frequency of the Gunn diode is around 80 GHz, which is obvious, as electrons now has to travel an extra distance compared to 1.0 μm. The results are shown in Figs 4.16 and 4.17.

The above results are repeated for various biasing voltages going as low as 25 V. Then the simulations are again run for all the above cases of different active lengths and different biasing voltages, but now with T = 600K. The results can be shown in Figs 4.18-4.23. At very low biasing levels, the electric field within the GaN device is close to the threshold for NDR, and hence the power output is low. With increasing bias, the output power increases, as does the operating frequency due to the larger average electron velocity. A central maxima thus results, and the general shape is in keeping with previous reports. At very high biasing, the transferred electron effect is lost with nearly all carriers residing primarily in the satellite valleys.
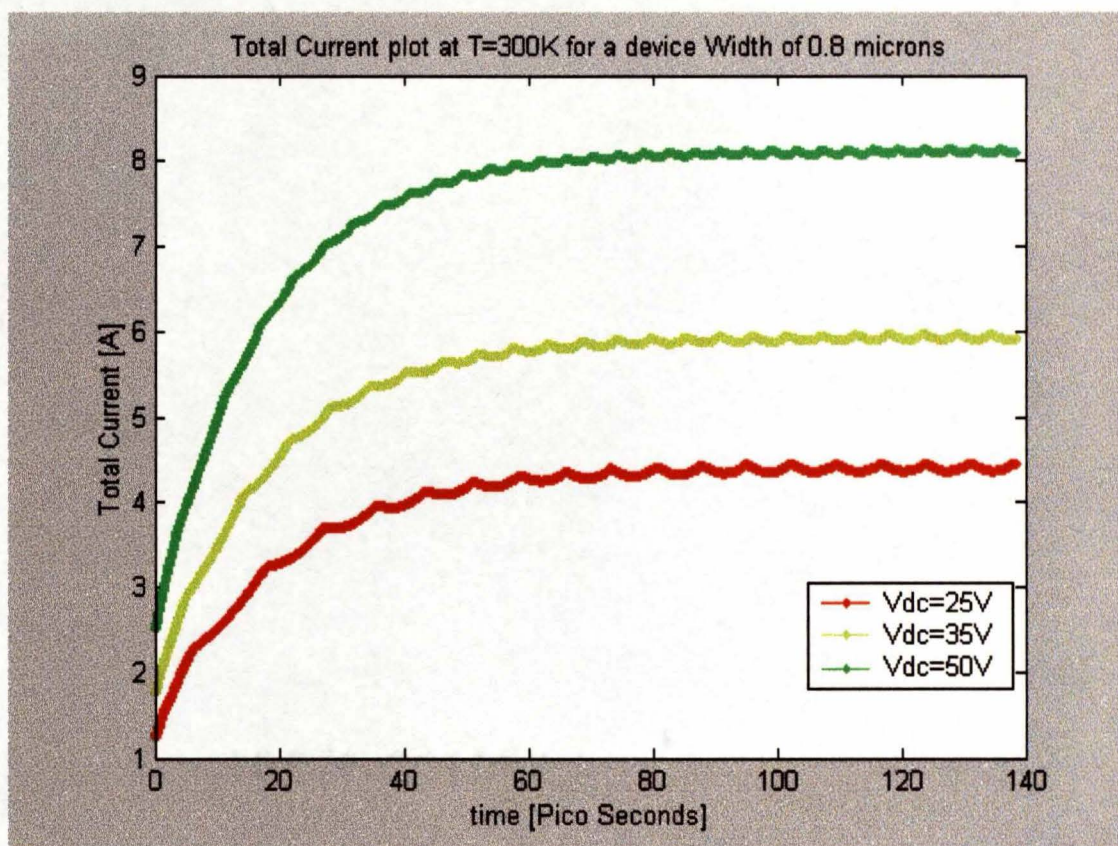
Fig. 4.14   Monte Carlo results showing the temporal development of the total current for

a 0.8µm device at T = 300K for various biasing voltages.
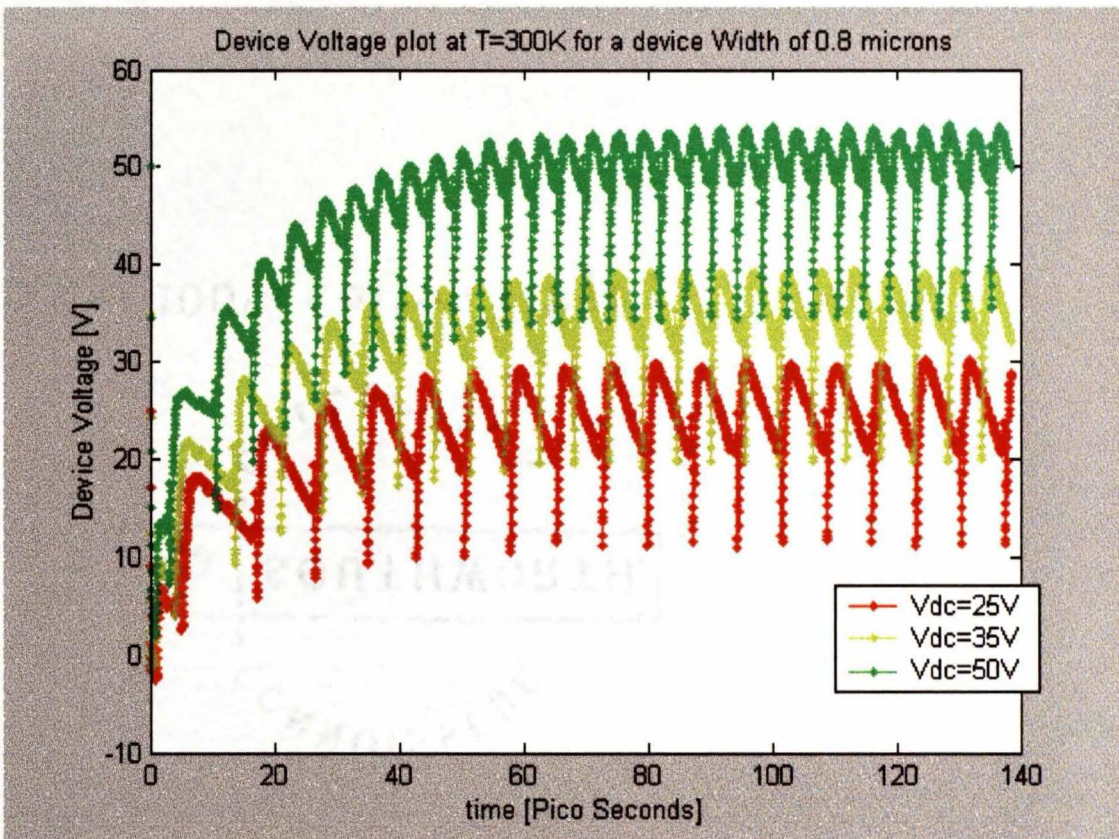
Fig. 4.15 Monte Carlo results showing the temporal development of the device voltage for a 0.8μm device at T = 300K for various biasing voltages.
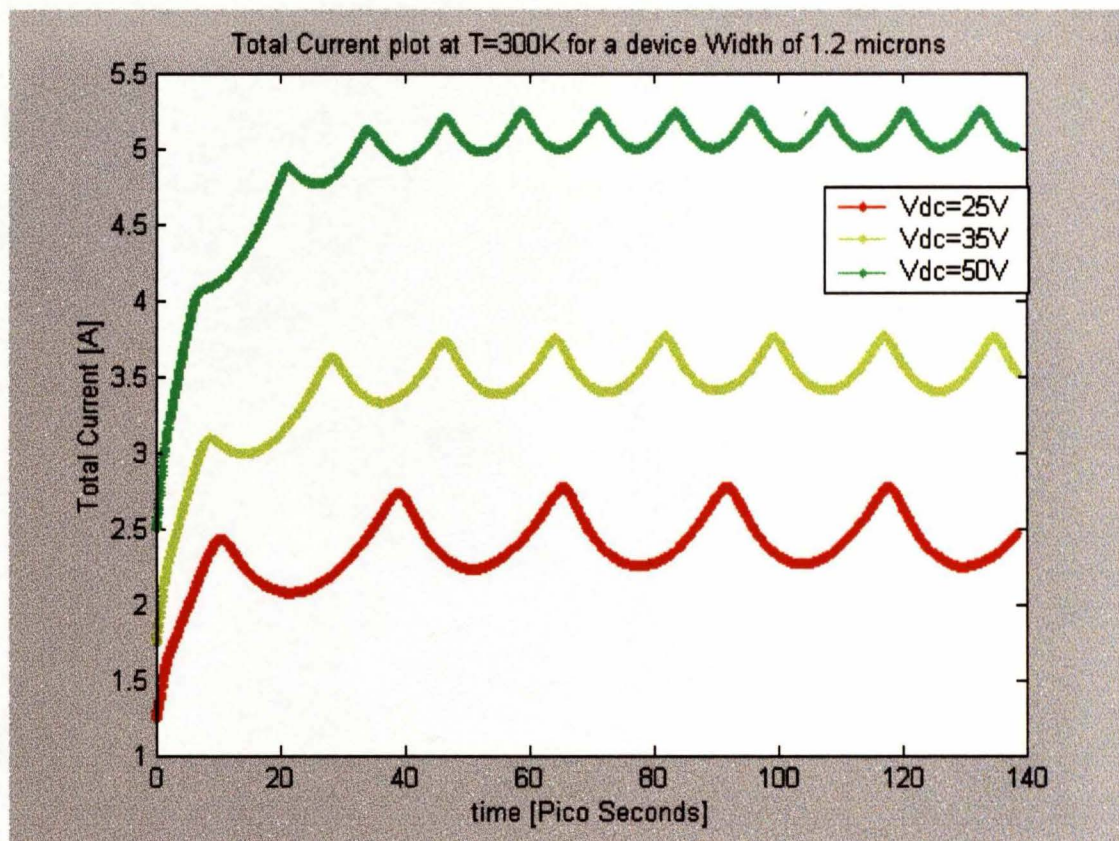
Fig. 4.16 Monte Carlo results showing the temporal development of the total current for a 1.2 μm device at T = 300K for various biasing voltages.
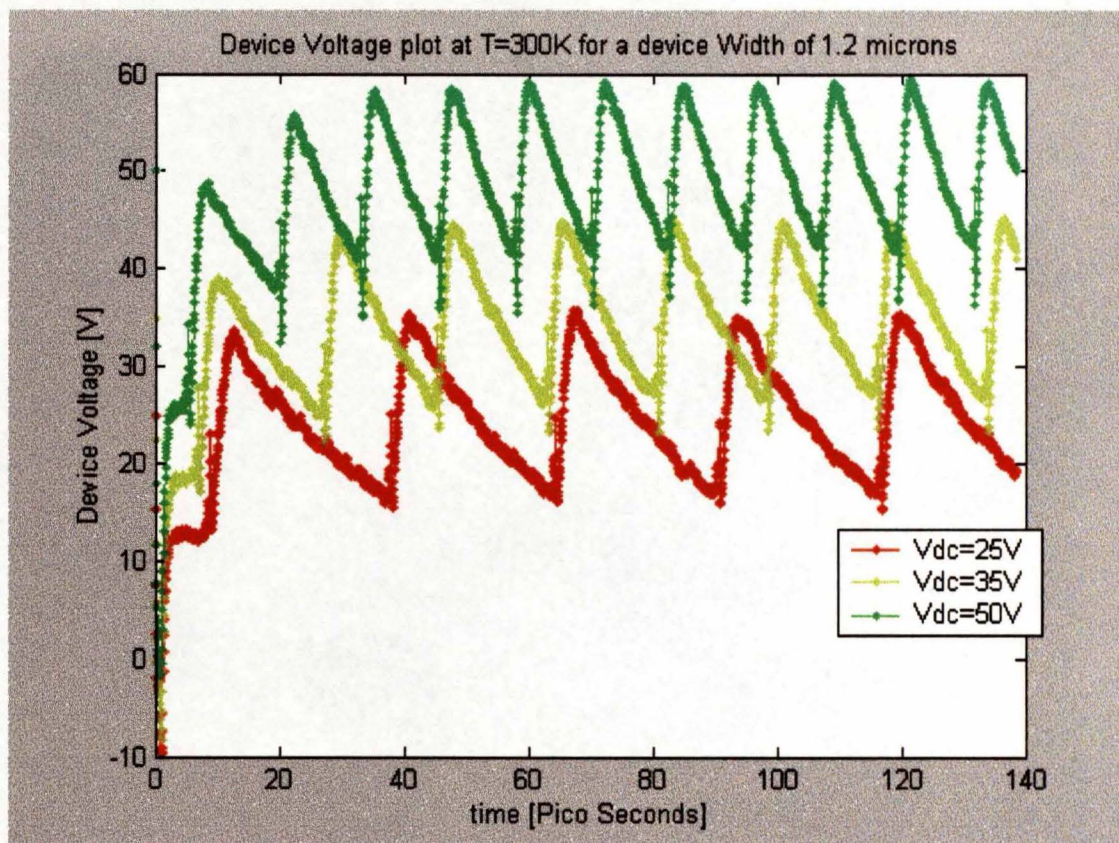
Fig. 4.17 Monte Carlo results showing the temporal development of the device voltage

for a 1.2μm device at T = 300K for various biasing voltages.
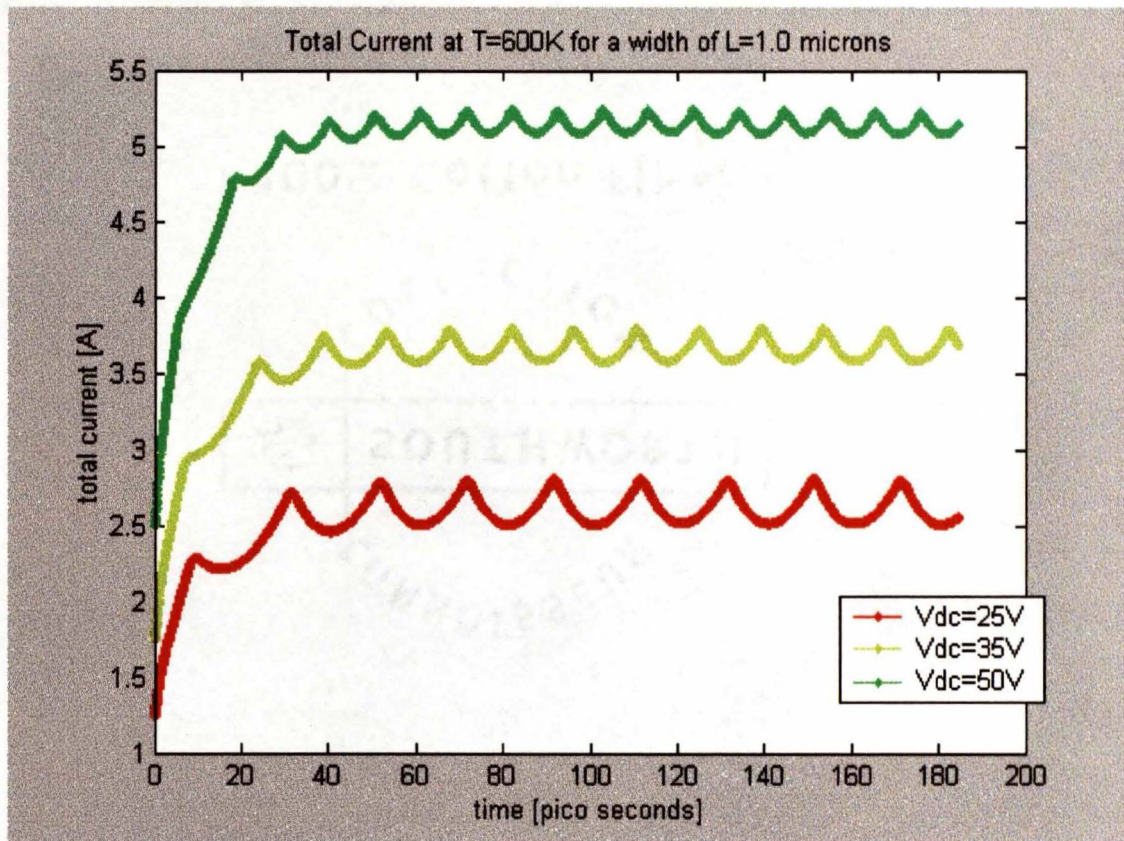
Fig. 4.18 Monte Carlo results showing the temporal development of the total current for a 1μm device at T = 600K for various biasing voltages.
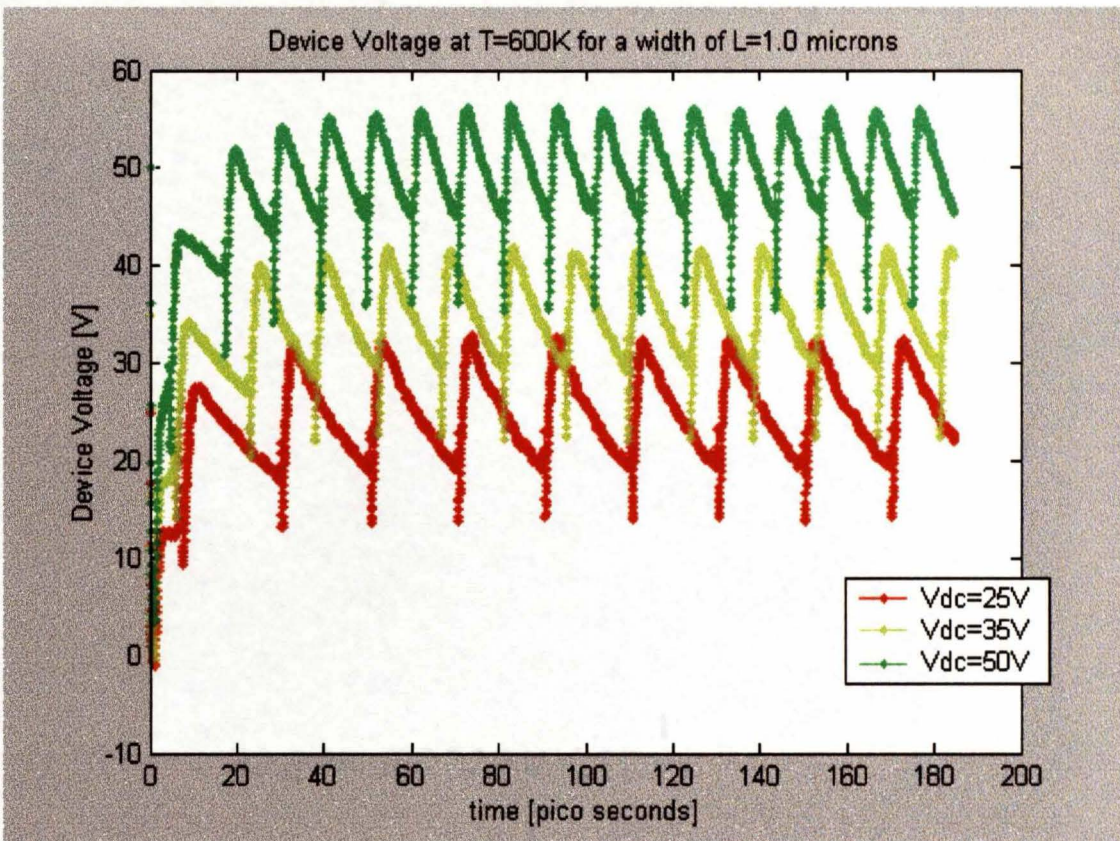
Fig. 4.19 Monte Carlo results showing the temporal development of the device voltage

for a 1µm device at T = 600K for various biasing voltages.
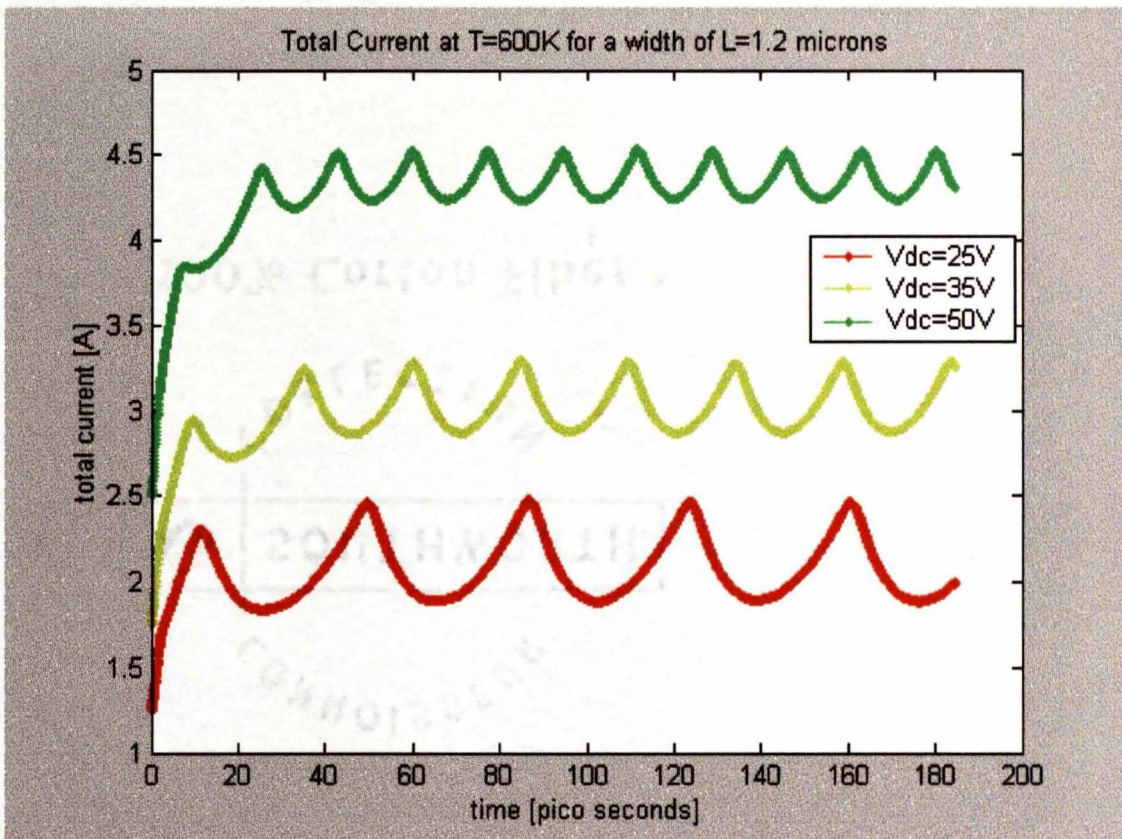
Fig. 4.20 Monte Carlo results showing the temporal development of the total current for a 1.2μm device at T = 600K for various biasing voltages.
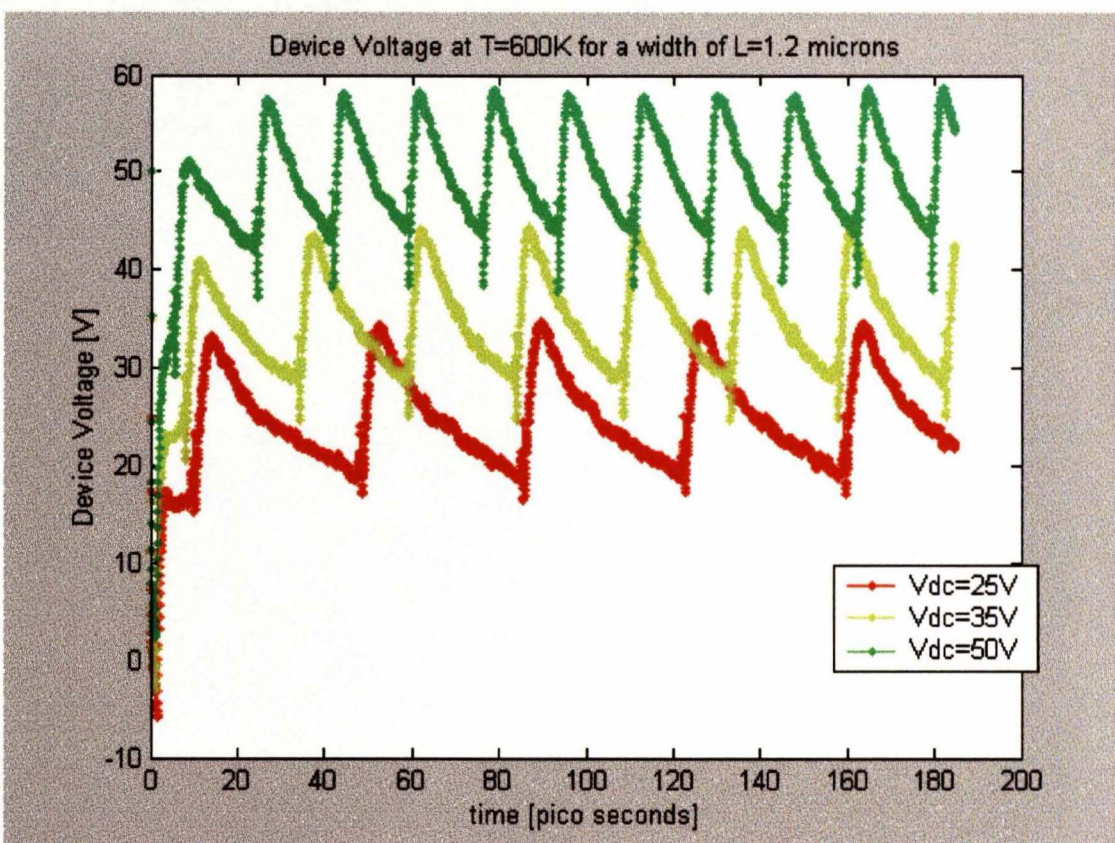
Fig. 4.21 Monte Carlo results showing the temporal development of the device voltage

for a 1.2μm device at T = 600K for various biasing voltages.
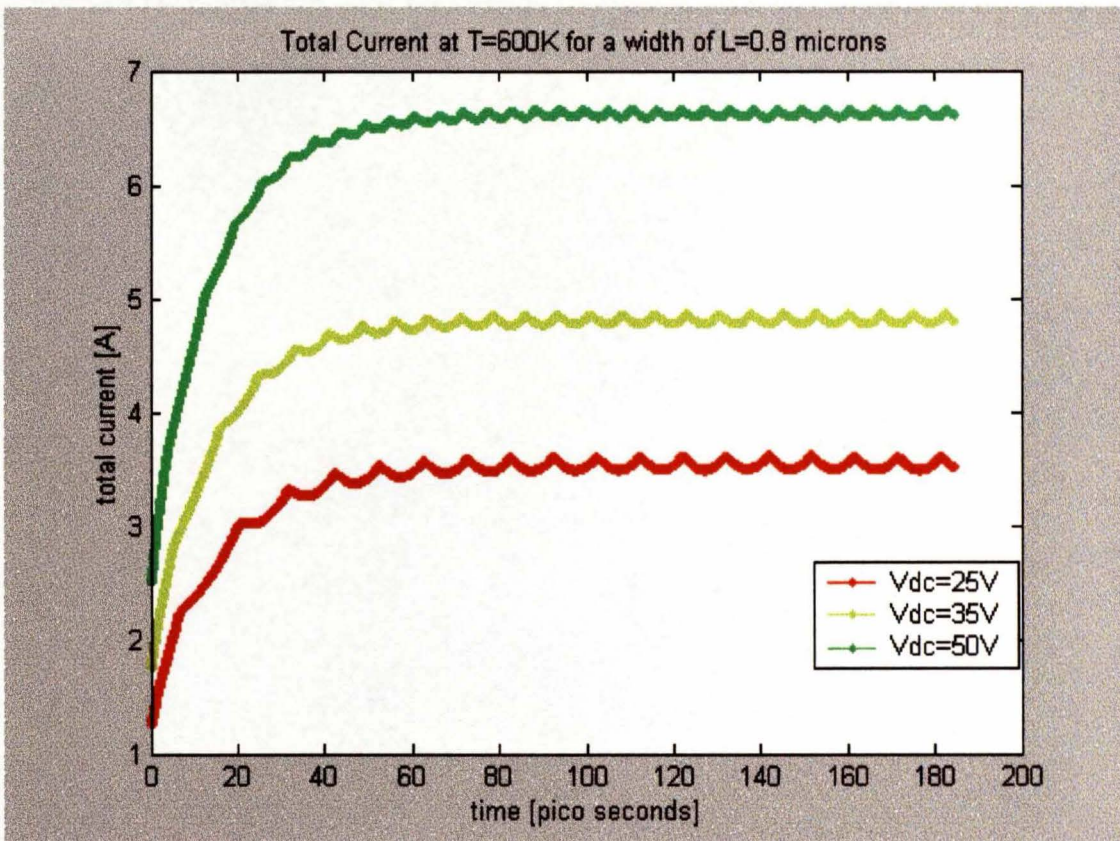
Fig. 4.22 Monte Carlo results showing the temporal development of the total current for a 0.8μm device at T = 600K for various biasing voltages.
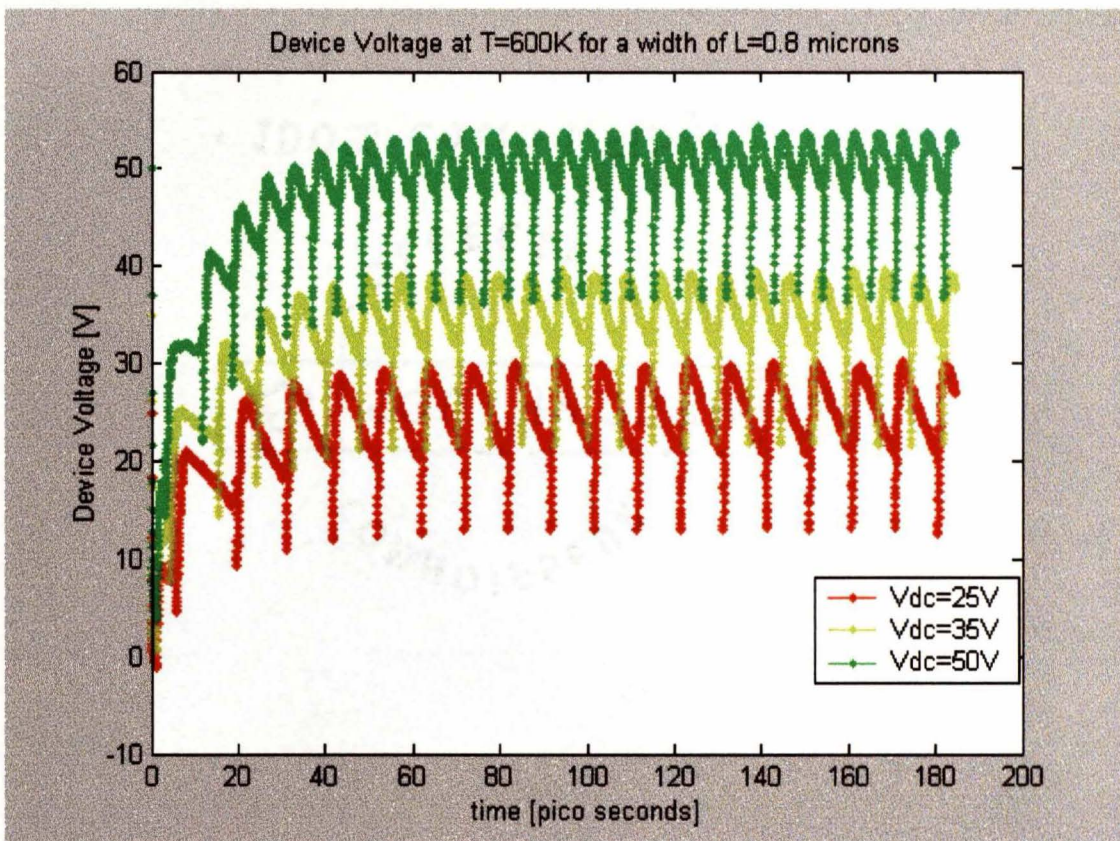
Fig. 4.23 Monte Carlo results showing the temporal development of the device voltage for a 0.8µm device at T = 600K for various biasing voltages.

Finally Monte Carlo simulations were performed for GaN diodes with multiple transit segments. The results are shown in Fig. 4.24 and Fig. 4.25 that compare the total current and device voltage for two-segment Gunn diode with single transit Gunn diode. The results are for applied bias of 35V and at a T = 300K for a device length of 1.2 μm. It should be noted that the device length in the two cases is same and is 1 μm. The transit time in case of two-segment Gunn diode is nearly half of the transit time of the single transit conventional notch Gunn diode. This is obvious as the two-segment Gunn diode can be treated as repetition of two single transit Gunn diodes with device length halved. This means that the operating frequency is almost doubled. But, the output power is less compared to the single transit Gunn diode. The output power can be increased for the case of a two-segment Gunn diode by using single transit Gunn diodes in series. In this case, the device length is twice for a two-segment Gunn diode compared to the single transit Gunn diode. In the above case, the operating frequency is same for both types of Gunn diodes.

Finally, voltage and current waveforms in the region of sustained oscillations were subjected to harmonic power analysis based on Fourier transformed and the obtained spectrum was used to determine the output power and the oscillation frequency. The resulting power output as a function of the frequency is given in Fig 4.26 at T = 300K and T = 450K for single domain GaN Gunn diodes. The efficiency of the Gunn diode is then calculated by dividing the output power with the power supplied by the applied bias across the device. The resulting conversion efficiency as a function of the frequency is given in Fig 4.27 at T = 300K and T = 450K. Fig. 4.26 shows peak powers of 0.665W and 0.525W at 300K and 450K operating temperatures. Since device self-
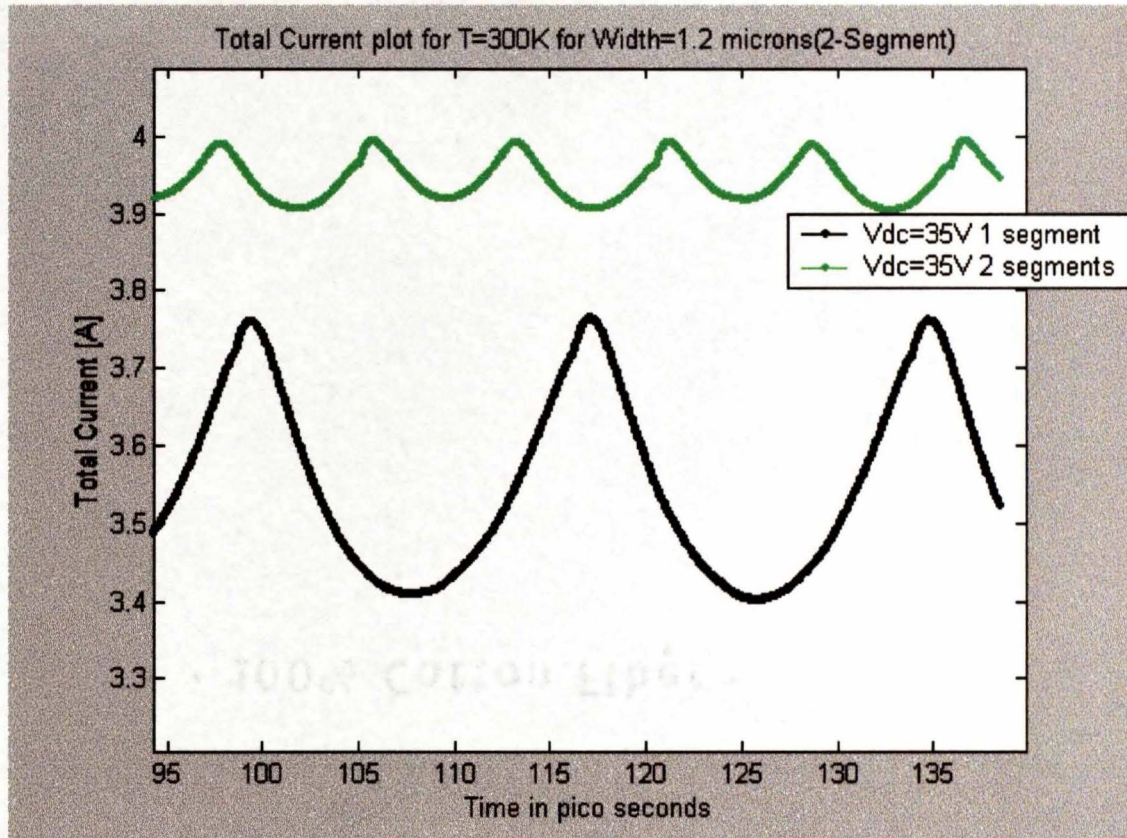
Fig. 4.24 Monte Carlo results showing the temporal development of the total current for

a 1.2μm device at T = 300K at 35V for both 1 segment and 2 segment Gunn diodes.
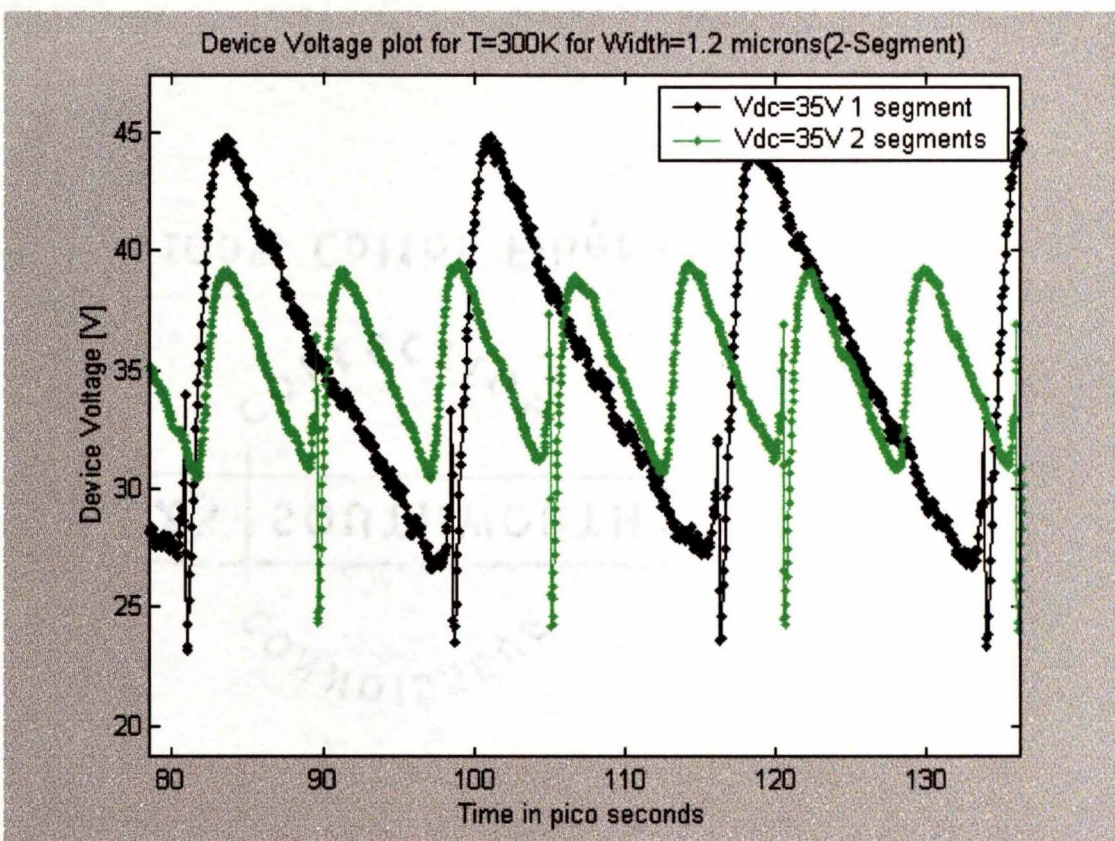
Fig. 4.25 Monte Carlo results showing the temporal development of the device voltage

for a 1.2μm device at T = 300K at 35V for both 1 segment and 2 segment Gunn diodes.
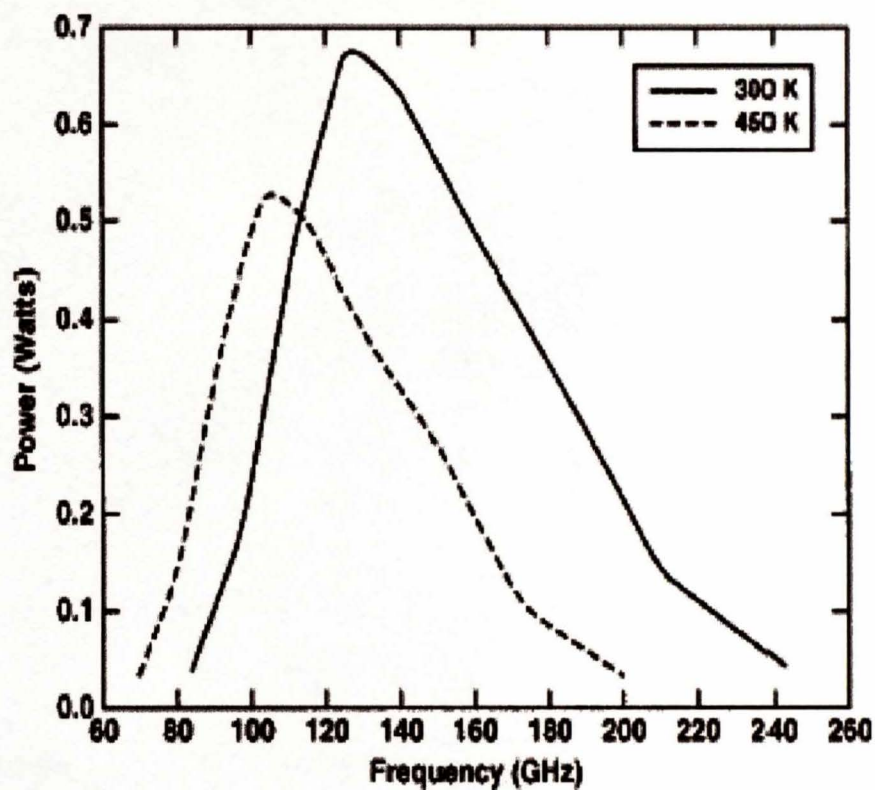
Fig. 4.26 Monte Carlo results of the power output vs frequency at T = 300K and T = 450K for single domain GaN Gunn diodes.
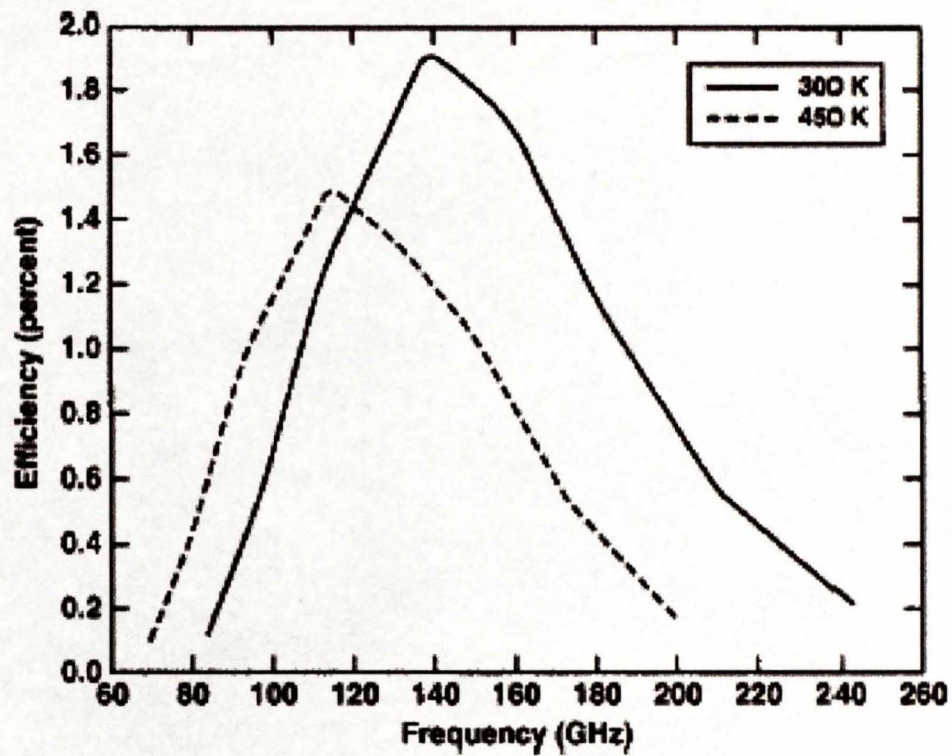
Fig. 4.27 Monte Carlo results of the device efficiency vs frequency at T = 300K and T = 450K for single domain GaN Gunn diodes.

heating effects have not been dealt with, these values represent an overestimation. Even then, there is still a considerable improvement over the reported results of about 0.15 W for InP [77]. This is obvious, since the threshold field for GaN is nearly 10 times larger than that of InP. The corresponding peak efficiencies are 1.9% and 1.47% at 300 and 450K operating temperatures, respectively, as shown in Fig. 4.27. The room temperature (300K) value is higher than that reported for GaAs devices [78]. Then, this analysis is carried to multi domain Gunn diode structure. The resulting output power as a function of frequency is given in Fig 4.28 and is compared with that of the single transit Gunn diode. A simplistic expectation is for the output power to scale N^2, with N the number of the segments for fixed values of the operating frequency, temperature and device impedance. This follows from a required scaling in both the voltage and device current. The voltage is scaled to maintain the electric fields in the device and the current is scaled due to an increase in area for maintaining the impedance. However, in practice, the benefits of a multiple transit structure might not be quite as significant for a variety of reasons. In a conventional single transit structure, the injected carriers are all nearly thermalized and have comparable energies. Hence, the device noise can be expected to be lower due to a relatively "tightly bunched" carrier distribution, especially for short device lengths. With multiple transit zones, however, the carrier distributions at the start of each successive transit segment might not be completely periodic, nor closely bunched in distributions, and could even be non-thermal. Consequently, one can expect a larger variance in the inter-valley transfer distance, leading to higher noise. The actual condition at the start of successive domains depends on the thickness and doping of the n^+ layer between the transit regions. Thicker and more strongly doped layers would facilitate better carrier
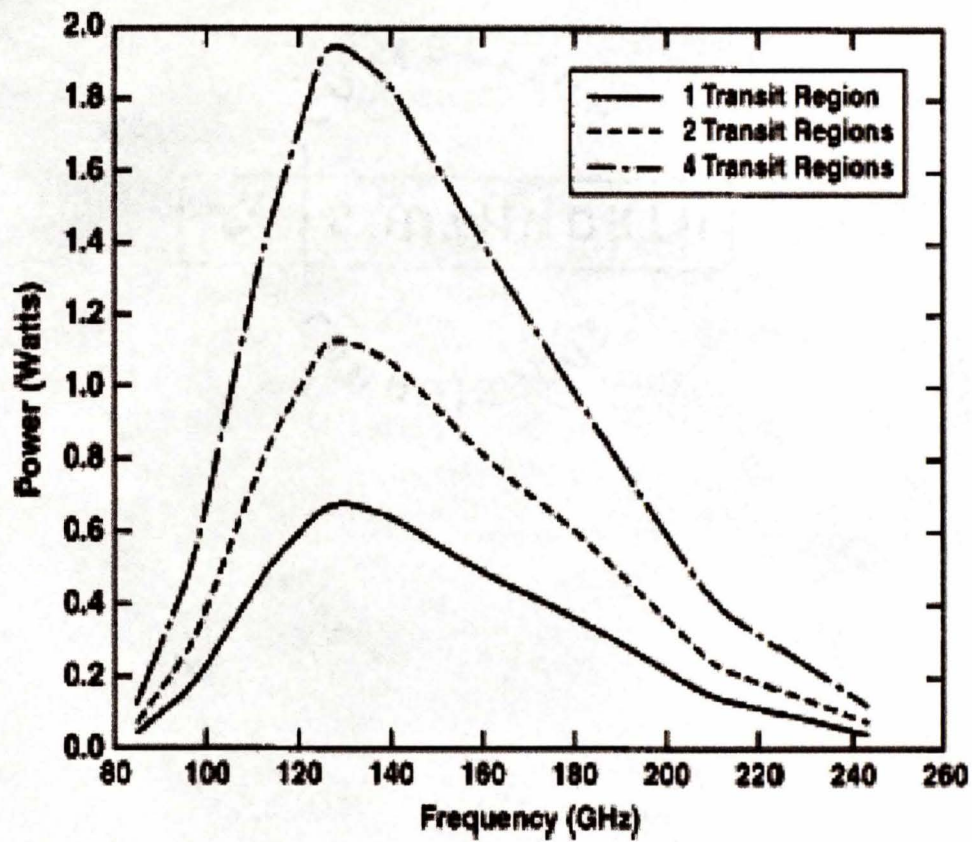
Fig. 4.28 Monte Carlo results of the power output vs frequency at T = 300K for multiple

transit segment GaN Gunn diodes. Plots for one, two and four segments are shown above.

thermalization, but would increase the overall transit time of a fully thermal distribution at the beginning of each successive transit region also implies that the average carrier energies within the device would tend to be larger. This could lead to higher internal power losses because of strong polar-optical phonon scattering, especially within the satellite valleys due to their higher density of states. In addition, with the hot electrons spending a longer fraction of their time within the satellite valleys, the overall speed would be slower, and the swing in the current oscillation reduced. Last, but not least, the higher power losses can be expected to lead to higher internal temperatures and possible thermal gradients due to local hot spots near the successive "virtual anodes". Both would adversely affect the transport and reduce the operating frequency. Collectively, the useful power output might not scale quite as well as N^2.

CHAPTER V

CONCLUSIONS

5.1   SUMMARIZING OVERVIEW

In the present research, the microwave and millimeter wave characteristics of conventional GaN Gunn diodes and multi-domain Gunn diode oscillators were evaluated. This was done by performing large-signal harmonic power analysis of current and voltage waveforms corresponding to sustained oscillations. A model for the self-consistent Ensemble Monte Carlo simulation of both conventional and multi-domain Gunn diode oscillators has been developed. A three valley Monte Carlo model was used for the GaN material, that included electron interactions with acoustic modes via the deformation potential, polar optical phonon interactions, zero- and first-order intervalley deformation potential scattering. Though the Monte Carlo scheme is well-known in the context of semiconductor transport studies and has been applied to many of the commonly used materials, it has not been used much for GaN and related nitride materials.

The results obtained in this Monte Carlo calculation seemed to correlate well with some of the experimental data available on wurtzite GaN. Wurtzite material has been chosen because analytical expressions of parameters, such as the non-parabolicity coefficients and effective masses are now available to facilitate an accurate Monte Carlo analysis. The analysis shows that the GaN based oscillators outperform GaAs Gunn diodes. Performance parameters of interest such as the operating frequency, output power

and conversion efficiency were calculated. Variations due to changes in temperature, biasing voltage and device length, are also included.

It has also been shown that multi-domain Gunn diodes can lead to improvements in output power over conventional, single-transit structure Gunn diodes. Series connections of Gunn diodes have been considered in the past, but have not been successful because of the difficulty of fabricating the devices accurately enough. In order to achieve stable multi-domain operation, the doping profile must be repeated, from section to section of the device, with high accuracy. Since new techniques of fabrication such as Molecular Beam Epitaxy have come of age, there has been a marked improvement in the accuracy of doping profiles. This should facilitate the successful fabrication and development of such multi-transit Gunn oscillators.

The results indicate that there is an improvement in the output power when compared to the value of about 0.15 W for InP. The output peak powers of 0.665W and 0.525W have been obtained for Wurtzite GaN at 300 K and 450 K temperatures, respectively. This is for the case of conventional transit structure Gunn diode. For multi-domain (2-segment) Gunn diode, the peak output power is predicted to be almost double than that of conventional single transit structures. A definite conclusion is that the multi-domain Gunn diode structure show improvement in performance against conventional Gunn devices, and are definite candidates for high power, microwave devices.

5.2   SCOPE FOR FUTURE WORK

The possible development of Gunn diodes is mainly governed by the output power generated and the conversion efficiency at a given operating frequency. The

various causes of power and efficiency limitations are space-charge effects, thermal dissipation and impedance requirements. In order to avoid space-charge effects, the carrier concentration should not deviate very much from the doping level. This helps prevent impact ionization and build-up of strong non-uniform electric fields in the transit region.

Since the output power developed is high in case of GaN Gunn diodes, there is a larger amount of current (say, as compared to GaAs devices) flowing in the device. Consequently, there is a distinct possibility for self-heating within the device. If proper care is not taken to dissipate this heat, the device performance could fall significantly. A possible reason would be the decrease in mobility associated with the enhanced phonon scattering at the elevated temperatures. One possibility is to use silicon (or even silicon carbide or diamond) substrates that would act as heat sink and result in a better heat flow away from the diode. Since the thermal conductivities of SiC and diamond are much larger by factors of about 2 and 5, thermal issues would be better managed. Another solution has been given by Sands et al. [79]. GaN films were grown on sapphire substrates and lifted off using a laser lift-off technique, and then successfully bonded to a silicon substrate. Besides thermal issues, another potential limitation is the minimum impedance than can be matched in microwave circuits. This occurs, because it is not possible to design a microwave circuit whose resistance is much smaller in magnitude than the absolute value of the negative resistance of the device.

Having considered the practical issues that need to be considered for improved performance, we proceed to discuss the other improvements that need to be included in the modeling. The current resonant circuit is modeled for the operation in fundamental

mode of oscillation. For practical applications, it is more common to use circuits operating in the harmonic mode, as these are easier to fabricate and tune. The present model can be extended to the harmonic operation by loading the Gunn diode with a number of parallel resonant circuits connected in series and tuned to the harmonic frequencies.

As we have seen, the frequency of the conventional Gunn diode is primarily dependent on the active transit length. However, a portion of this length is used to accelerate the electrons from the cathode to the low-mobility, high-energy state. This portion of the length does not contribute to the domain formation. This "dead" zone is nearly 10-20% of the active length, and since it acts as a parasitic resistance, this results in reduced efficiency. The limitations of the conventional Gunn diode can be overcome by injecting high energy, hot electrons into the transit region. This can be achieved using a graded gap Gunn diode. The concept is to introduce electrons into a region so that their temperature, which describes their energy distribution, is much greater than that of the semiconductor lattice. In the graded gap Gunn diode, the electrons are injected into the transit region with an energy equal to that of the Γ-L intervalley separation so that stable domains will form very near to the cathode and move across the transit region as soon as the field is high enough to sustain accumulation and propagation. This could be achievd by employing a AlGaN emitter region which would have a larger bandgap as compard to the GaN-transit region. The dead zone could then effectively be eliminated and the transit length fixed independent of the applied bias.

Finally, one way to obtain the resulting operating frequency is by placing regions of high doping at positions at which domains are to be quenched. However, this operating

frequency should be about the same as that of conventional transit time Gunn diodes. An advantage of this domain quenching mechanism is that it removes the heated electrons from the active region very quickly, allowing a new domain to be formed near the cathode. Other potential modeling work would include the evaluation of heterojunction GaN-AlGaN diodes, and coupled Monte Carlo-heat diffusion equations for an electro-thermal analysis.

REFERENCES

1. P. J. Bulman, G. S. Hobson, B. C. Taylor, *Transferred Electron Devices* (Academic Press, NewYork, 1972).

2. J. R. Hauser, T. H. Glisson, and M. A. Littlejohn, Solid State Elect. **22**, 487 (1979).

3. C. Patel, T. J. Parker, H. Jamshidi, and W. F. Sherman, Phys. Stat. Sol. B **122**, 461 (1984).

4. J. Shah, B. Deveaud, T. C. Damen, W. T. Tsang, A. C. Gossard, and P. Lugli, Phys. Rev. Lett. **59**, 2222 (1987).

5. H. W. Thim, J. Appl. Phys. **39**, 3897 (1965).

6. M. Slater and R. J. Harrison, IEEE Trans. Electron Devices **23**, 560 (1976).

7. J. A. Copeland, J. Appl. Phys. **38**, 3096 (1967).

8. D. Jones and H. D. Rees, Electron. Lett. **8**, 566 (1972).

9. R. Bosch and H. W. Thim, IEEE Trans. Elec. Dev. **21**, 16 (1974).

10. P. A. Lebwohl and P. Price, Appl. Phys. Lett. **19**, 530 (1971).

11. D. E. Aspnes, C. G. Olson, and D. W. Lynch, Phys. Rev. Lett. **37**, 766 (1976).

12. J. W. Tully, IEEE Trans. Elec. Dev. **30**, 566 (1983).

13. Y. F. Wu, B. P. Keller, S. Keller, D. Kapolnek, P. Kozodoy, S. P. Denbaars, and U. K. Mishra, Appl. Phys. Lett. **69**, 1438 (1996).

14. S. N. Mohammad, A. Salvador, and H. Morkoc, Proc. IEEE **83**, 1306 (1995).

15. H. Morkoc, *Nitride Semiconductors and Devices* (Springer-Verlag, Heidelberg, 1999).

16. R. P. Joshi Appl. Phys. Lett. **64**, 223 (1994) ; R. P. Joshi, A. N. Dharamsi and J. Mcadoo, Appl. Phy. Lett. **64**, 3611 (1994).

17. Nakamura, T. Mukai, and M. Senoh, Appl. Phys. Lett. **64**, 1687 (1994).

18. R. Gaska, Q. Chen, J. Yang, A. Osinky, M. A. Khan, and M. S. Shur, IEEE Electr. Dev. Lett. **18**, 492 (1997).

19. Keller, G. Parish, P. T. Fini, S. Heikman, C. H. Chen, N. Zhang, S. P. Denbaars, and U. K. Mishra, J. Appl. Phys. **86**, 5850 (1999).

20. R. Gaska, M. S. Shur, A. D. Bykhovski, A. O. Orlov, and G. L. Snider, Appl. Phys. Lett. **74**, 287 (1999).

21. K. Shenai, R. S. Scott and B. J. Baliga, IEEE Trans. Electr. Dev. **36**, 1811 (1989).

22. S. Nakamura, M. Senoh, S. Nagahama, N. Iwasa, T. Yamada, T. Matsushita, H. Kiyoku, Y. Sugimoto, T. Kozaki, H. Umemoto, M. Sano, and K. Chocho, Jpn. J. Appl. Phys. II- Lett. **36**, L1568 (1997).

23. G. E. Bulman, K. Doverspike, S. T. Sheppard, T. W. Weeks, H. S. Kong, H. M. Dieringer, J. A. Edmond, J. D. Brown, J. T. Swindell, J. F. Schetzina, Electr. Lett. **33**, 1556 (1997).

24. S. Nakamura, M. Senoh, N. Iwasa, S. Nagahama, T. Yamada, T. Mukai, Jpn. J. Appl. Phys. **34**, L1332 (1995).

25. I. J. Fritz and T. J. Drummond, Electr. Lett. **31**, 68 (1995).

26. H. Morkoc and S. N. Mohammad, in Light Emitting Diodes, *Wiley Enclopedia of Electrical and Electronics Engineering*, edited by J. Webster. (New York: J. Wiley and Sons, 1999).

27. H. Morkoc, IEEE J. Selected Topics in Quantum Electronics **4**, 537 (1998).

28. U. Bhapkar and M. S. Shur, J. Appl. Phys. **82**, 1649 (1997).

29. J. D. Albrecht, R. P. Wang, P. P. Ruden, M. Farahmand, and K. F. Brennan,

J. Appl. Phys. **83**, 4777 (1998).

30. W. F. Yu, B. P. Keller, P. Fini, J. Pusl, M. Le, N. Nguyen, C. Nguyen,
    D. Widman, S. Keller, S. P. Denbaars, and U. K. Mishra, Electronics Lett. **33**, 1742 (1997).

31. S. T. Sheppard, K. Doverspike, W. L. Pribble, S. T. Allen, J. W. Palmour,
    L. T. Kehias, and T. J. Jenkins, Electr. Dev. Lett. **20**, 161 (1999).

32. F. Wu, B. P. Keller, S. Keller, D. Kapolnek, S. P. Denbaars, and U. K. Mishra,
    IEEE lectr. Dev. Lett. **17**, 455 (1996).

33. Y. F. Wu, D. Kapolnek, J. P. Ibbetson, P. Parikh, B. P. Keller, and
    U. K. Mishra, IEEE Trans. Electr. Dev. **48**, 586 (2001).

34. D. E. Grider, N. X. Nguyen, and C. Nguyen, Solid State Electr. **43**, 1473 (1999).

35. S. Rumyantsev, M. E. Levinshtein, R. Gaska, M. S. Shur, A. Khan, J. W. Yang,
    G. Simin, A. Ping, and T. Adesida, Phys. Stat. Sol. A, **176**, 201 (1999).

36. G. J. Sullivan, M. Y. Chen, J. A. Higgins, J. W. Yang, Q. Chen, R. L. Pierson, and
    B. T. McDermott, IEEE Electr. Dev. Lett.**19**, 198 (1998).

37. S. C. Binari, K. Doverspike, G. Kelner, and H. B. Dietrich, Solid St. Electr. **41**, 177 (1997).

38. E. M. Chumbes, J. Smart, T. Prunty, and J. R. Shealy, IEEE Trans. Electr.
    Dev. **48**, 416 (2001).

39. P. Das and D. K. Ferry, Solid-State Electron **19**, 851 (1976).

40. M. Littlejohn, J. R. Hauser and T.H. Glisson, Appl. Phys. Lett. **26**, 625 (1975).

41. N. S. Mansour, K. W. Kim and M. A. Littlejohn, J. Appl. Phys. **77**, 2834 (1995).

42. J. Kolnik, I.H. Oguzman, K.F. Brennan, R. Wang, P.P. Ruden, and Y. Wang, Journal of Applied Physics **78**, 1033 (1995).

43. L. Kleinman and J. C. Philips, Phys. Rev. **118**, 1153 (1960).

44. M. L. Cohen and T. K. bergstresser, Phys. Rev. **141**, 789 (1966).

45. P. O. Lowdin, J. Chem. Phys. **19**, 1396 (1951).

46. M. Fanciulli, T.Lei and T. D. Moustakas, Phys. Rev. **B48**, 15144 (1993).

47. S. T. Sheppard, K. Doverspike, W. L. Pribble, S. T. Allen, J. W. Palmour, L. T. Kehias, and T. J. Jenkins, Electr. Dev. Lett. **20**, 161 (1999).

48. M. Shur, *GaAs Devices and Circuits* (Plenum Press, New York and London, 1987).

49. U. Bhapkar and M. S. Shur, J. Appl. Phys. **82**, 1649 (1997).

50. J. B. Gunn, Solid State Commun., **1**, 88 (1963).

51. R. L. Johnston, B. C. DeLoach, Jr., and B. G. Cohen, Bell Syst. Tech. J., **44**, 369 (1965).

52. M. M. Atalla and J. L. Moll, Solid State Electron., **12**, 619 (1969).

53. J. A. Copeland, Proc. IEEE, **54**, 1479 (1966).

54. B. K. Ridley, J.Appl. Phys., **48**, 754 (1977).

55. J. Ondria, and R. L. Ross, **17**[th] European Microwave Conference Digest (1987).

56. http://www.dur.ac.uk/condensed_matter_theory.group/ssterratum/paper/node2.html

57. S. Tiwari, in *Compound SemiconductorDevices,* (Academic Press, N.York, 1992).

58. B. R. Nag, in *Electron Transport in Compound Semiconductors* (Springer-Verlag,Berlin, 1980).

59. E. M. Convell, Solid State Phys. **6**, 109 (1967).

60. H. G. Reik and H. Risken, Phys. Rev.**126**, 1737 (1962).

61. H. Budd, J. Phys. Soc. Japan **21,** 424 (1966).

62. T. Kurowasa, J. Phys. Soc. Japan **21,** 424(1966).

63. W. Fawcett, in Electron in Crystalline Solids, (International Atomic Energy Agency, Vienna, 1973).

64. A. D. Broadman, in *Physics Programs*, edited by A.D.Broadman (Wiley, New York, 1980).

65. A. D. Boardman, W. Fawcett, and H. D. Rees, Solid State Communications. **6,** 305 (1968).

66. W. Fawcett, A. D. Boardman, and S. Swain, J.Phys. Chem. Sol. **31,** 1963 (1970).

67. C. Jacoboni and L. Reggiani, Rev. Mod. Phys. **55,** 3209 (1994).

68. E. M. Conwell and V. F. Weisskopf, Phys. Rev. **77,** 388(1950).

69. H. Brooks and C. Herring, Phys. Rev. **83,** 879(1951).

70. W. Fawcett, A. D. Boardman, and S. Swain, J. Phys. Chem. Solids **31,** 1963 (1970).

71. J. Tsay, S. E. Schwarz, S. Raman, and J. S. Smith, Microwave and Optical Technology Letters **3,** 54 (1990).

72. H. W. Thim, J. Appl. Phys. **39,** 3897 (1965).4. P. A. Blakey and R.K. Froelich, IEEE Trans. Microwave Theory Tech., **MTT-31,** 781 (1983).

73. E. Alekseev and D. Pavlidis, Electronics Letters **36,** 176 (2000).

74. U. Bhapkar and M. S. Shur, J. Appl. Phys. **82,** 1649 (1997).

75. B. E. Foutz, S. K. O'Leary, M. S. Shur, and L. F. Eastmen, J. Appl. Phys. **85,** 7727 (1999).

76. M. Goano, E. Bellotti, E. Ghillino, G. Ghione, and K. F. Brennan, J. Appl. Phys. **88,** 6467 (2000).

77. V. Gruzinskis, E. Starikov, P. Shiktorov, L. Reggiani, and L. Varani, J. Appl. Phys. **76**, 5260 (1994).

78. R. Vaidyanathan and R. P. Joshi, Electron. Lett. **27**, 1555 (1991).

79. W.S. Wong, Y. Cho, N.J. Quitoriano, T. Sands, A.B. Wengrow and N.W. Cheung, "Integration of GaN thin films with dissimilar substrate materials by Pd-In metal bonding and laser liftoff," *J. Electron. Mater.* **28**, 1409 (1999).